Supporting Information for "The influence of support materials on the structural and electronic properties of gold nanoparticles - A DFT study"

Julien Engel, Samantha Francis, and Alberto Roldan

Table of Content

1. Structure of supported Au clusters

In the following section, the supported metal clusters are identified as $Au_n[A\text{-}B(\text{-}C)]_X$ for a gold cluster with *n* atoms in which *A* gold atoms at the cluster-support interface, *B* in the next layer, and *C* in third layer growing perpendicular to the surface. The subindex X is added to distinguish cluster with otherwise identical names.

1.1 Au/MgO

The most stable position for a single gold atom adsorption on a magnesia support is on top of the oxygen ($Au_1[1]_a$). This lowest energy position is in agreement with previous computational work by Ferrando and Fortunelli[1] and is also supported by experimental EPR spectra data produced by Yulikov et al.[2] In this configuration, the distance between the adatom and the surface is 2.31 Å. The energy difference to the adsorption on top of a magnesium atom or in the void between these positions is found to be +0.474 eV and +0.272 eV respectively. Gold atoms placed on a bridge site between an oxygen atom and a magnesium atom (B) falls to a position on top of the oxygen upon optimisation. On addition of a second atom to the cluster using the built-up approached previously described, the cluster preferentially adopts a perpendicular structure, where the second atom sits directly on top of the first atom (Au_2[1-1]). The distance between the cluster and the surface is reduced to 2.16 Å with a gold-gold distance of 2.52 Å. This configuration is 0.46 eV more stable than a parallel dimer structure, where the gold atoms sit on top of two adjacent oxygen atoms at a distance of 2.59 Å also obtained by this method (Au_2[2-0]). When the cluster grows to accommodate a third atom, there becomes two points of contact with the support, both of which are on top of an oxygen atom, bridged by the third gold atom (Au_3[2-1]). There are two structures formed for Au_3 which are energetically similar. In the lowest energy structure, the oxygen atoms interacting with the trimer are separated by 6.03 Å, whereas for the alternate structure the gold atoms are coordinated to two closer oxygen atoms (4.26 Å apart) with a smaller Au–Au–Au angle and bridging over a magnesium atom. This structure ($Au_3[2\text{-}1]_b$) is 0.008eV higher in energy. For the lowest energy structure, the average gold-gold distance is increased to 2.60 Å and the distance between the cluster and the surface 2.29 Å.

The four-atom gold cluster has a Y-shaped planar structure perpendicular to the surface as its most stable. Compared to the structure of Au_3, the fourth gold atom is added over one of the gold-gold bonds, creating a triangular substructure. A parallelogram-shaped structure perpendicular to the surface, a low energy structure obtained from previous literature with higher average gold coordination number.[1], is higher in energy by 0.095 eV.

The lowest energy structures up until Au_4 were found using the described built-up method and are shown to be perpendicular planar. However, at a cluster size of five gold atoms, the lowest energy (perpendicular, planar trapezium) shape adopted is not obtainable from the previous lowest energy structure of Au_4 but one found in previously reported studies.[3] From six gold atoms on, parallel planar clusters become favoured over perpendicular structures. Hence, Au_6 adopts a triangular shaped parallel planar structure as its lowest configuration whereas the perpendicular structure of the same triangular shape is 0.575 eV less stable. This trend is corroborated by the work of Vilhelmsen *et al.* using a more accurate meta-GGA functional, their work shows the same shapes formed as the lowest energy structures.[3] Beyond the Au_6 clusters up to Au_{19}, the parallel planar structures persist as the most stable. Overall the cluster shapes are not defined by the MgO lattice structure, and instead take the hexagonal form as expected for a gold monolayer. However, there is a slight various to this trend, which affects the distances between surface and interface atoms, as well as the average Au-Au distance.

For Au_6, Au_8 and Au_9, the trend is altered as a consequence of two slightly more stable structures for Au_6 and Au_8. The detachment energies and the cohesive energies are both higher than expected for these sizes, and the distances to the surface increased. The Au_8 takes on a shape that is influenced by the MgO lattice, producing a square-centred star-shaped structure. This consequently affects the distances within the Au_9 cluster since the distortion is perpetuated until the hexagonal structure is once again fully adopted for Au_{10}.

Table S 1: Structures of Au_1/MgO.

	$Au_1[1]_a$	$Au_1[1]_b$	$Au_1[1]_c$
Top	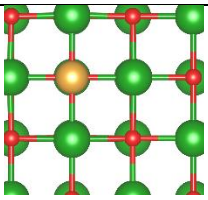	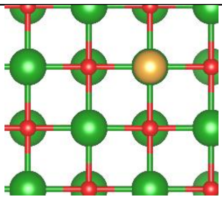	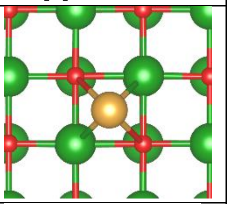
Side	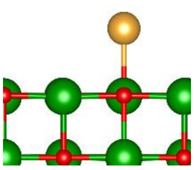	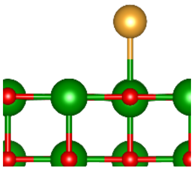	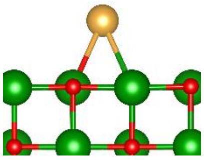
ΔE [eV]	0.00	+0.47	+0.27

Table S 2: Structures of Au_2/MgO.

	Au_2[1-1]	Au_2[2-0]
Top	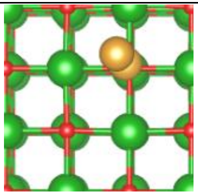	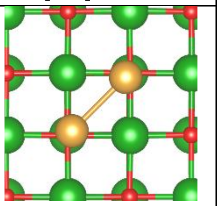
Side	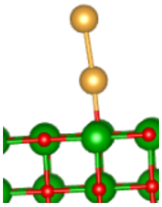	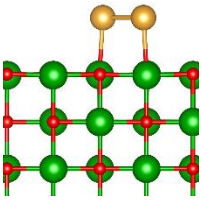
ΔE [eV]	0.00	+0.46

Table S 3: Structures of Au$_3$/MgO.

	Au$_3$[2-1]$_a$	Au$_3$[2-1]$_b$
Top	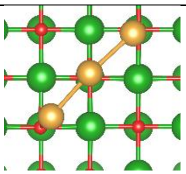	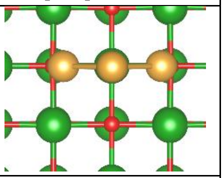
Side	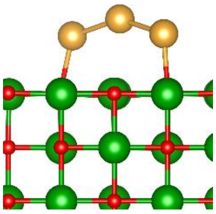	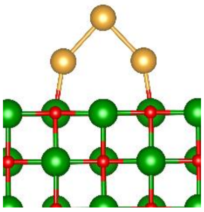
ΔE [eV]	0.00	+0.008 eV

Table S 4: Structures of Au$_4$/MgO.

	Au$_4$[2-2]$_a$	Au$_4$[2-2]$_b$	Au$_4$[3-1]
Top	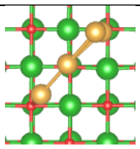	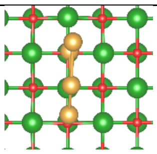	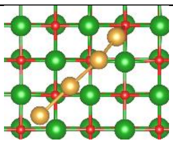
Side	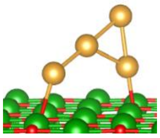	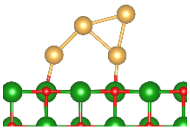	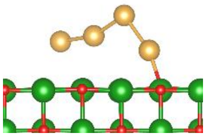
ΔE [eV]	0.00	+0.10	+0.72

Table S 5: Structures of Au$_5$/MgO.

	Au$_5$[3-2]	Au$_5$[5]	Au$_5$[3-1-1]	Au$_5$[4-1]	Au$_5$[2-1-1-1]
Top	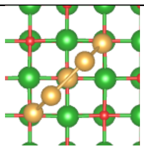	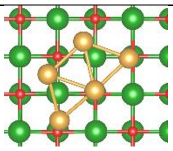	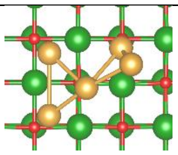	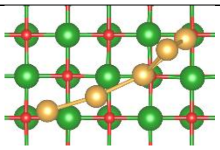	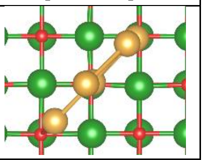
Side	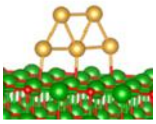	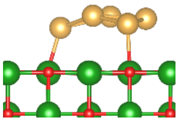	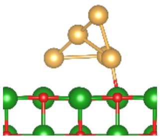	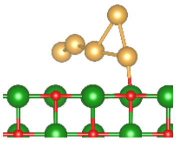	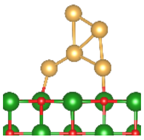
ΔE [eV]	0.00	+0.03	+0.06	+0.26	+0.53

Table S 6: Structures of Au$_6$/MgO.

	Au$_6$[6]	Au$_6$[3-2-1]	Au$_6$[4-1-1]$_a$	Au$_6$[4-1-1]$_b$
Top	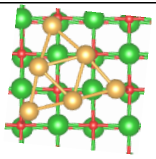	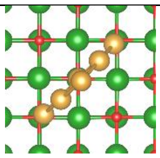	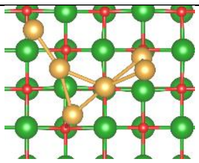	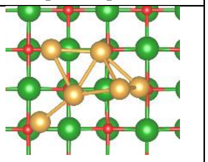
Side	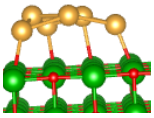	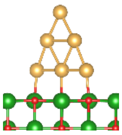	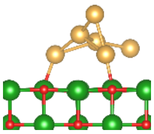	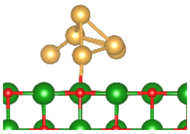
ΔE [eV]	0.00	+0.37	+0.52	+0.075

Table S 7: Structures of Au$_7$/MgO.

	Au$_7$[7]$_a$	Au$_7$[7]$_b$	Au$_7$[7]$_c$	Au$_7$[4-3]	Au$_7$[3-3-1]
Top	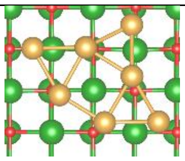	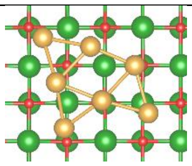	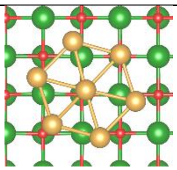	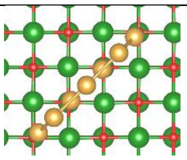	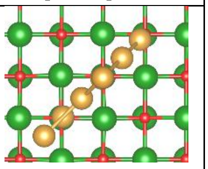
Side	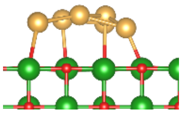	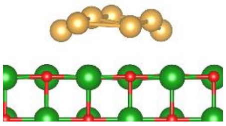	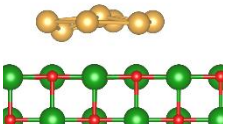	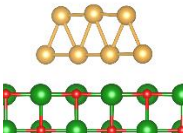	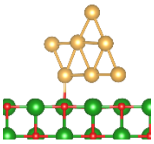
ΔE [eV]	0.00	+0.05	+0.32	+0.56	+0.76

Table S 8: Structures of Au$_8$/MgO.

	Au$_8$[8]$_a$	Au$_8$[7-1]	Au$_8$[8]$_b$	Au$_8$[8]$_c$
Top	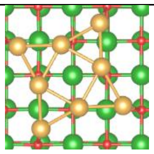	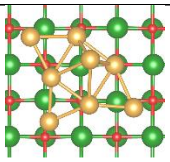	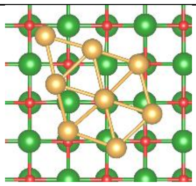	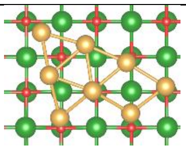
Side	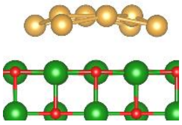	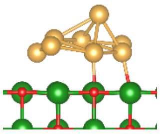	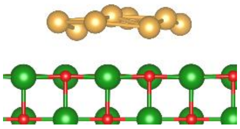	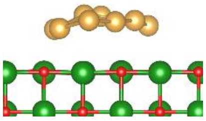
ΔE [eV]	0.00	+0.56	+0.63	+0.83

Table S 9: Structures of Au_9/MgO.

	$Au_9[9]_a$	$Au_9[9]_b$	$Au_9[8\text{-}1]$
Top	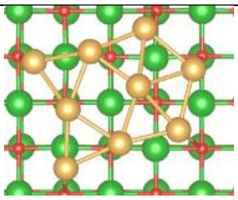	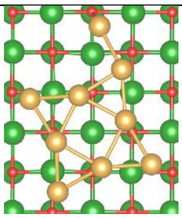	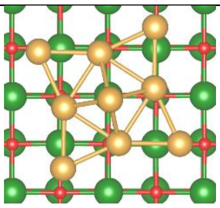
Side	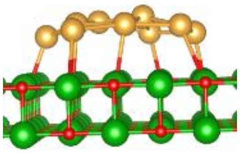	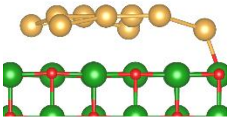	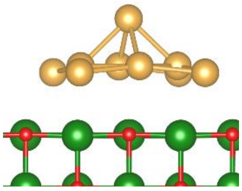
ΔE [eV]	0.00	+0.27	+0.31

Table S 10: Structures of Au_{10}/MgO.

	$Au_{10}[10]_a$	$Au_{10}[10]_b$	$Au_{10}[10]_c$	$Au_{10}[10]_d$
Top	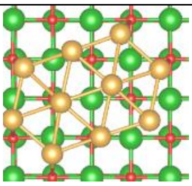	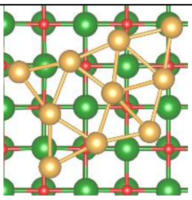	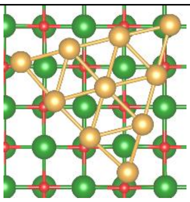	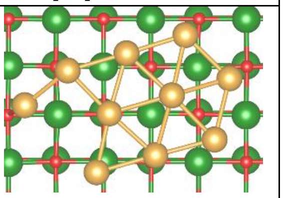
Side	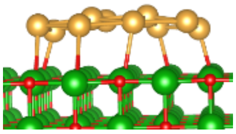	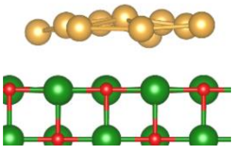	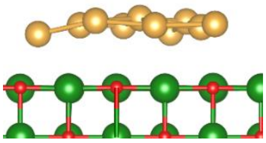	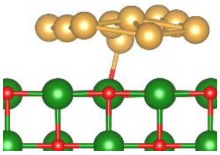
ΔE [eV]	0.00	+0.36	+0.61	+0.57

Table S 11: Structures of Au$_{11}$/MgO.

	Au$_{11}$[11]$_a$	Au$_{11}$[11]$_b$	Au$_{11}$[6-4-1]
Name			
Top	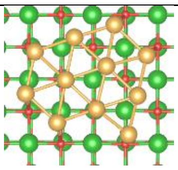	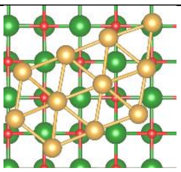	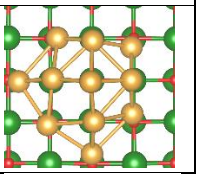
Side	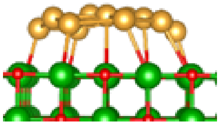	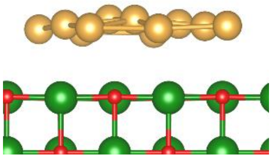	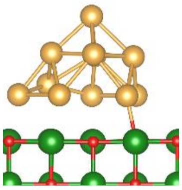
ΔE [eV]	0.00	+0.21	+0.90

Table S 12: Structures of Au$_{12}$/MgO.

	Au$_{12}$[12]$_a$	Au$_{12}$[12]$_b$	Au$_{12}$[9-3]
Top	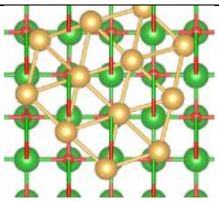	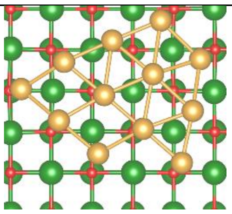	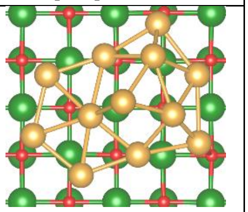
Side	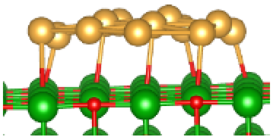	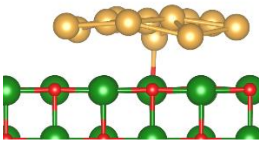	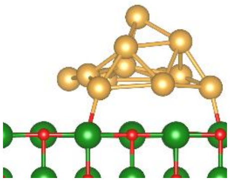
ΔE [eV]	0.00	+0.44	+0.99

Table S 13: Structures of Au_{13}/MgO.

	Au_{13}[13]	Au_{13}[8-4-1]	Au_{13}[8-5]
Top	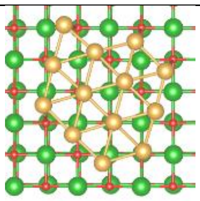	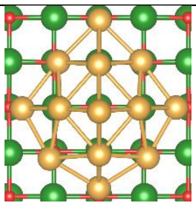	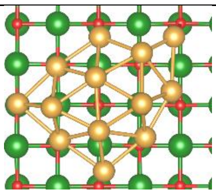
Side	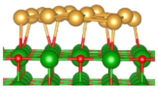	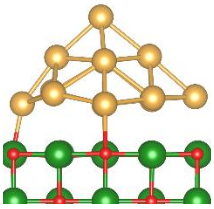	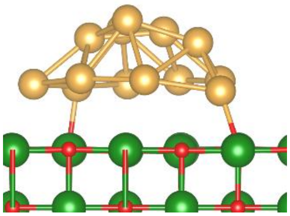
ΔE [eV]	0.00	+0.49	+0.88

Table S 14: Structures of Au_{15}/MgO.

	$Au_{15}[15]_a$	$Au_{15}[15]_b$	$Au_{15}[15]_c$	Au_{15}[10-4-1]
Top	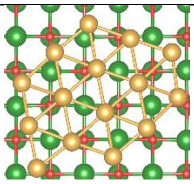	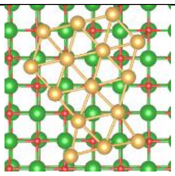	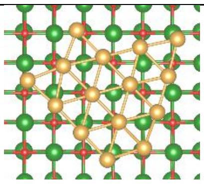	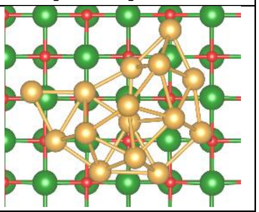
Side	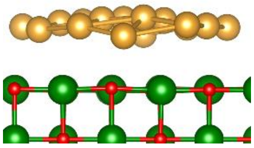	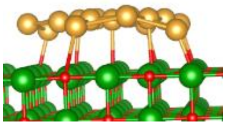	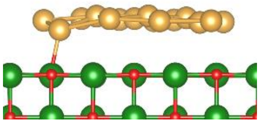	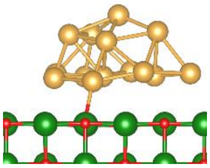
ΔE [eV]		+0.26	+0.50	+0.88

Table S 15: Structures of Au_{16}/MgO.

Name	$Au_{16}[16]_a$	$Au_{16}[16]_b$
Top	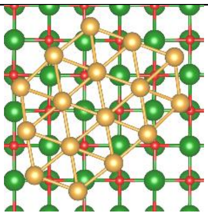	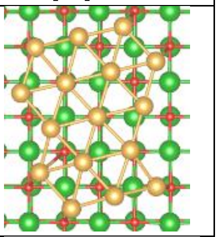
Side	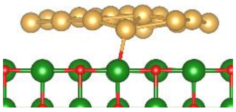	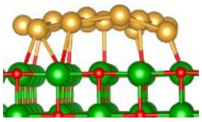
ΔE [eV]		+0.51

Table S 16: Structures of Au_{17}/MgO.

Name	$Au_{17}[17]_a$	$Au_{17}[17]_b$
Top	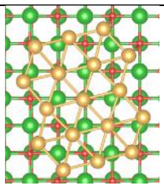	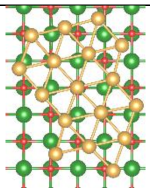
Side	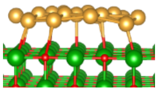	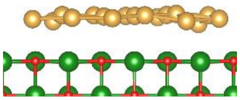
ΔE [eV]		+0.50

Table S 17: Structures of Au_{19}/MgO.

Name	$Au_{19}[19]_a$	$Au_{19}[11\text{-}6\text{-}2]$
Top	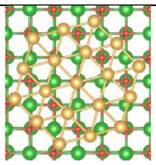	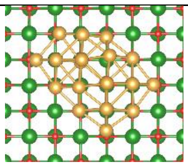
Side	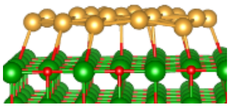	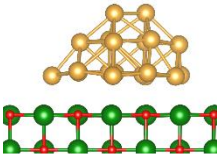
ΔE [eV]		+1.1

1.2 Structures of Au/C

On the (0001) surface of graphite are generally four different positions for a gold adatom.[4] The gold can be located on top of a carbon atom over another carbon atom in the layer beneath (top-α-position; T_α) or over a carbon atom located over a void in the layer beneath (top-β-position; T_β). In our single-layered model, these two positions are equal (top position; T). Furthermore, the adatom can also be placed over a carbon-carbon bond (bridge position; B). In the hollow position (H), the gold atom is placed above the middle of one of the six-membered carbon interacting in an η^6-fashion to the support. Our calculations indicate that the top position is favoured over the bridge position by 0.002 eV and the hollow position by 0.010 eV, which is within the margin of error of the calculations and in agreement with previous computational investigations.[5–11] The distance between the surface and the gold atom in the lowest energy T structure is 2.99 Å.

Addition of a second gold atom gives preferably a perpendicular structure as shown by other studies.[5,8,10,12] However, the position of the dimer on the surface is controversial. Calculations within the LDA method by Wang *et al.* predict the dimer to be located over a hollow position.[5] The results by Jalkanen *et al.* with PW91 showed the top and bridge positions to be equally favoured over the hollow position.[12] Varns *et al.* reported that, based on LDA calculations, the B position is favoured over the T and H positions.[8] The T position was found to be favoured in calculations with PBE by Amft *et al.*[10] Our calculations suggest that the top position is favoured ($Au_2[1\text{-}1]_a$), but as in the case of a single gold atom, the same perpendicular structure on a B position ($Au_2[1\text{-}1]_b$) is not significantly different in energy (+0.01 eV). The gold-surface distance in the perpendicular dimer on top of a carbon atom is reduced when compared to the gold adatom by 0.49 Å to 2.50 Å. Perpendicular arrangements over the hollow position relaxed during the geometry optimisation procedure to the top position. Parallel structures were found to be only stable at top positions ($Au_2[2\text{-}0]_a$ and $Au_2[2\text{-}0]_b$] and are 0.33 eV higher in energy than the lowest energy configuration.

For clusters with three gold atoms, the lowest energy configuration is a perpendicular, triangular structure with one gold atom on the surface ($Au_3[1\text{-}2]_a$). The bridge position is favoured in this case over the top position with an energy difference of 0.03 eV ($Au_3[1\text{-}2]_b$). The distance to the surface is further reduced to 2.39 Å because of the addition of the third atom. This structure is in agreement with a computational study of Wang *et al.* using LDA, which showed a perpendicular triangular structure (on top or bridge) to be most favoured.[13] Moreover, Amft *et al.* reported that such structure over the bridge position is most stable (PBE).[10] Parallel triangular clusters ($Au_3[3\text{-}0]_a$) are 0.37 eV higher in energy. However, a planar, nearly linear configuration ($Au_3[3\text{-}0]_b$; $\alpha = 172.9°$) is only 0.03 eV higher in energy than $Au_3[1\text{-}2]_a$.

The addition of a fourth gold atom gives a Y-shaped as lowest energy configuration ($Au_4[2\text{-}2]$) and not a parallelogram shape ($Au_4[1\text{-}3]$) which has a larger number of Au–Au bonds. This is corroborated by GGA calculations[10] of Amft *et al.*, while LDA calculations[13] predict the parallelogram-shaped cluster to be more stable. The distance of the lowest gold atom to the surface is 2.30 Å. A three-dimensional tetrahedron-shaped configuration was not stable during the geometry optimisation procedure. Clusters with more than four gold atoms were found to be planar and parallel to the surface.

The most stable structure of Au_5 is a planar trapezium-shaped cluster oriented parallel to the surface ($Au_5[5\text{-}0]_a$). Due to the change to a parallel structure, the number of interface atoms increases resulting in a decrease of the strength of the interaction with the surface per interface atom and therefore an increase of the distance between the cluster and the surface to 3.34 Å. Furthermore, the average gold-gold distance is slightly increased to 2.71 Å compared to 2.64 Å in Au_4. This is close to the average gold-gold distance that we calculated for a Au(111) monolayer (2.74 Å).

Addition of a sixth gold atom gives a highly symmetric triangular cluster parallel on the surface (Au_6[6-0]). For seven atoms, we found that a highly symmetric hexagonal cluster (Au_7[7-0]$_c$) is disfavoured by 0.31 eV with respect to a triangular cluster with one additional atom at the interface (Au_7[7-0]$_a$). As for smaller clusters, it is not relevant for the energy of the system whether the gold atoms are located on top of carbon atoms or on a bridge position in between two carbon atoms (Au_7[7-0]$_c$). While most structures show a triangular substructures of the gold atoms resembling the (111) surface of gold, the most stable structure of an eight-atom cluster is D_{4h} symmetric star-shaped with a square arrangement of the central four gold atoms (Au_8[8-0]$_a$). The structural change is represented in the average gold-gold distance, which increases from 2.71 Å (in Au_7) to 2.85 Å (in Au_8). This structure was previously identified as the most stable shape in the gas phase.[14] A parallel planar structure formed from Au_7[7-0]$_a$ or Au_7[7-0]$_c$ by addition of a gold atom at the interface is 0.37 eV higher in energy (Au_8[8-0]$_b$). The most stable structures of Au_9 on graphene cannot be constructed from Au_8[8-0]$_a$ but by extension of Au_8[8-0]$_b$. Interestingly, the more symmetric planar structure Au_9[9-0]$_b$ (D_{2h} symmetry) is 0.21 eV higher in energy than the C_{2v} symmetric most stable structures Au_9[9-0]$_a$ and Au_9[9-0]$_c$. Up to 19 atoms, the lowest energy structures of all clusters remain planar and parallel to the surface. Addition of a gold atom in a second layer results in relaxation to a planar single-layered cluster or strongly distorted structures with high energy after the geometry optimisation procedure. However, we found that for 19 gold atoms, the preferred structure is a three-dimensional C_{3v}-symmetric cluster with ten atoms in a triangular interface layer, six atoms in a second layer, and a third layer of three atoms (Au_{19}[10-6-3]). This structure is 0.64 eV lower in energy than the best planar cluster, a hexagonal-shaped D_{6h} symmetric cluster with a diameter of 1.1 nm (Au_{19}[19-0]$_a$).

Table S 18: Structures of Au$_1$/C.

	Au$_1$[1]$_a$	Au$_1$[1]$_b$	Au$_1$[1]$_c$
Top	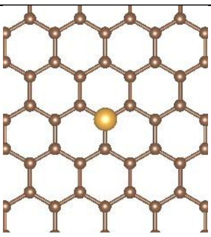	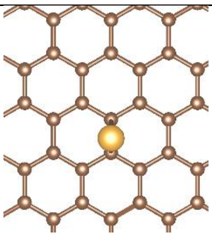	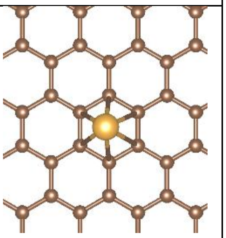
Side	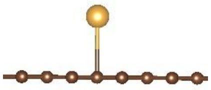	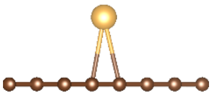	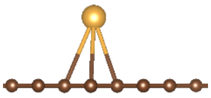
ΔE [eV]	0.00	+0.00	+0.01

Table S 19: Structures of Au$_2$/C.

	Au$_2$[1-1]$_a$	Au$_2$[1-1]$_b$	Au$_2$[2-0]$_a$	Au$_2$[2-0]$_b$
Top	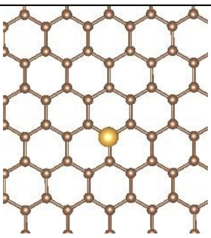	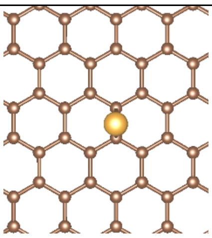	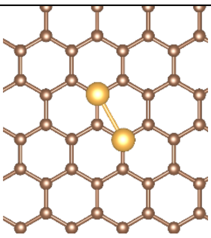	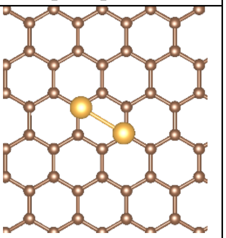
Side	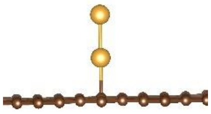	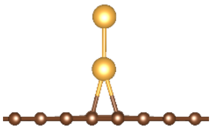	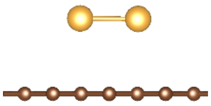	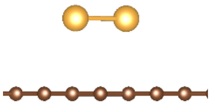
ΔE [eV]	0.00	+0.01	+0.34	+0.33

Table S 20: Structures of Au$_3$/C.

	Au$_3$[1-2]$_a$	Au$_3$[3-0]$_a$	Au$_3$[1-1-1]	Au$_3$[3-0]$_b$	Au$_3$[1-2]$_b$
Top	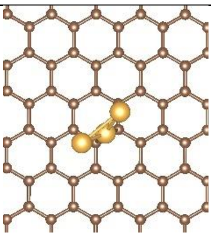	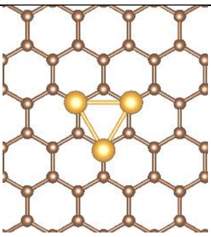	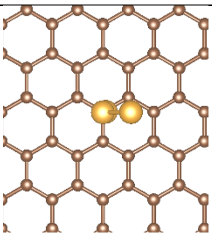	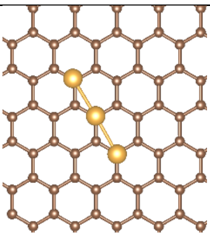	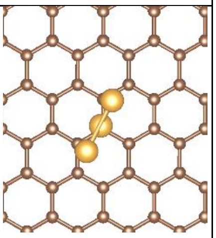
Side	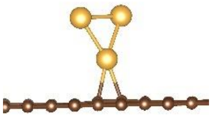	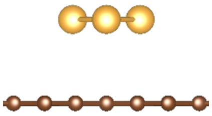	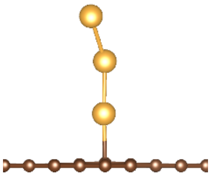	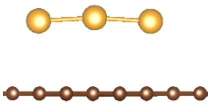	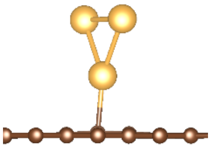
ΔE [eV]	0.00	+0.37	+0.26	+0.03	+0.03

Table S 21: Structures of Au$_4$/C.

	Au$_4$[2-2]	Au$_4$[1-3]	Au$_4$[1-2-1]	Au$_4$[4-0]$_a$	Au$_4$[4-0]$_b$
Top	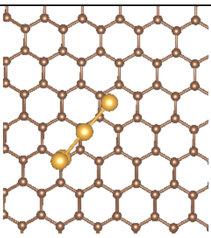	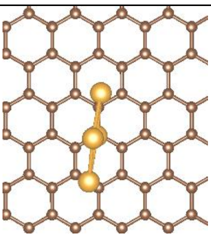	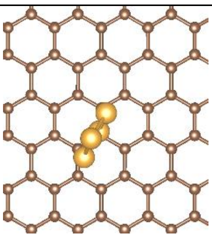	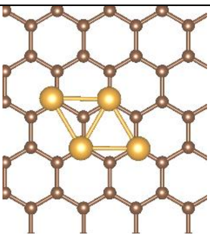	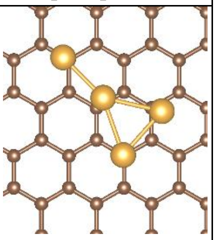
Side	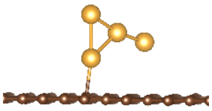	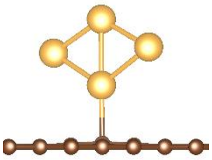	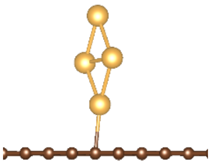	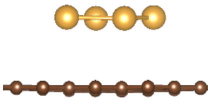	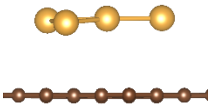
ΔE [eV]	0.00	+0.15	+0.71	+0.34	+0.34

Table S 22: Structures of Au$_5$/C.

	Au$_5$[5-0]$_a$	Au$_5$[2-3]	Au$_5$[1-2-2]	Au$_5$[1-3-1]	Au$_5$[4-1]
Top	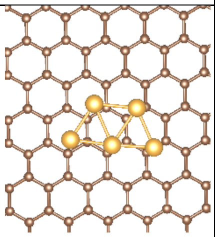	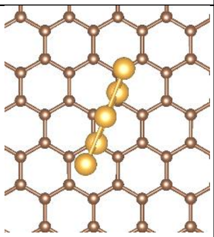	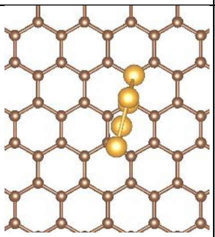	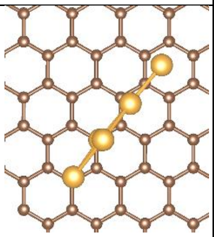	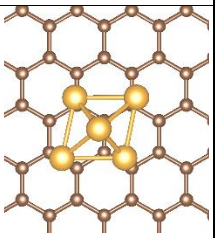
Side	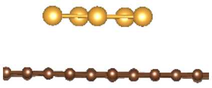	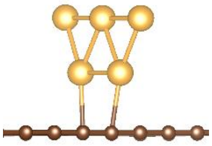	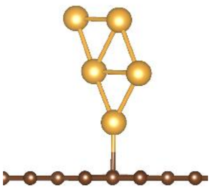	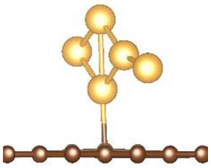	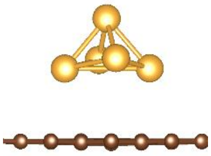
ΔE [eV]	0.00	+0.34	+0.42	+0.60	+1.00

Table S 23: Structures of Au$_6$/C.

	Au$_6$[6-0]	Au$_6$[1-2-3]	Au$_6$[3-2-1]
Top	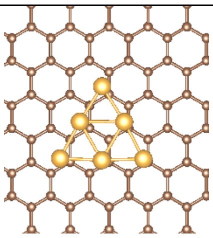	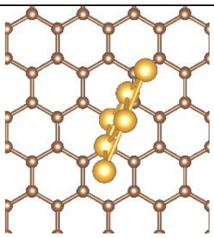	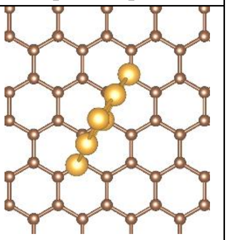
Side	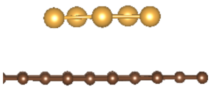	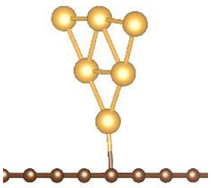	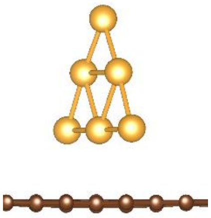
ΔE [eV]	0.00	+0.54	+0.35

Table S 24: Structures of Au$_7$/C.

	Au$_7$[7-0]$_a$	Au$_7$[7-0]$_b$	Au$_7$[6-1]	Au$_7$[7-0]$_c$
Top	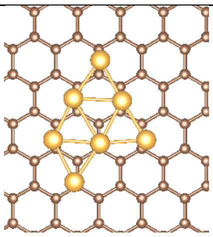	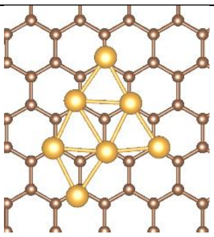	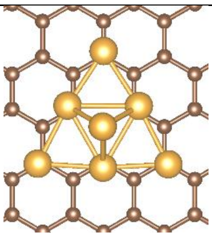	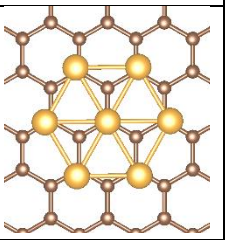
Side	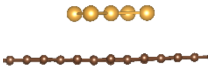	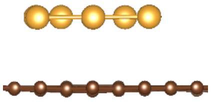	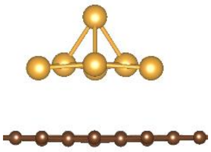	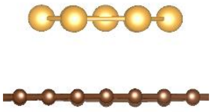
ΔE [eV]	0.00	+0.02	+0.51	+0.31

Table S 25: Structures of Au$_8$/C.

	Au$_8$[8-0]$_a$	Au$_8$[8-0]$_b$	Au$_8$[5-3]	Au$_8$[8-0]$_c$
Top	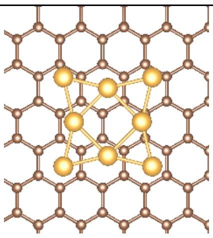	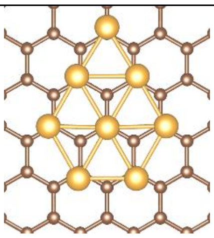	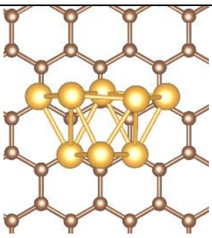	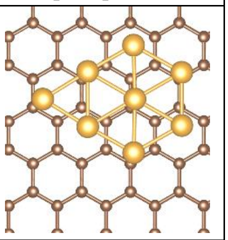
Side	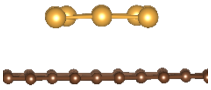	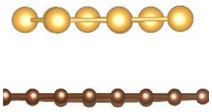	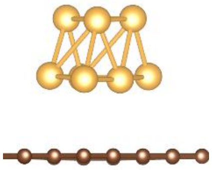	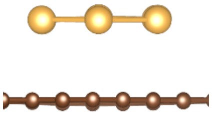
ΔE [eV]	0.00	+0.37	+0.76	+0.35

Table S 26: Structures of Au$_9$/C.

	Au$_9$[9-0]$_a$	Au$_9$[9-0]$_b$	Au$_9$[9-0]$_c$	Au$_9$[6-3]	Au$_9$[8-1]
Top	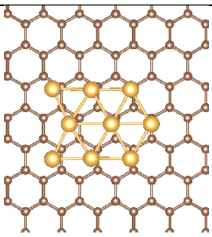	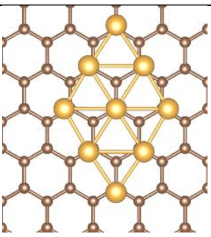	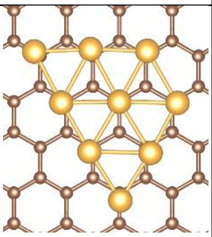	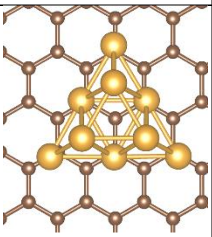	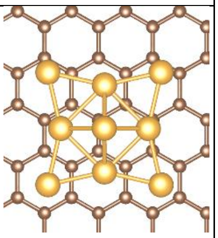
Side	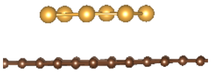	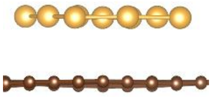	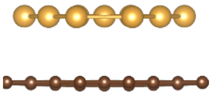	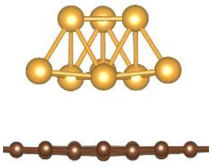	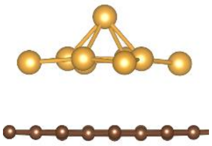
ΔE [eV]	0.00	+0.21	+0.00	+0.70	+0.24

Table S 27: Structures of Au$_{10}$/C.

	Au$_{10}$[10-0]$_a$	Au$_{10}$[10-0]$_b$
Top	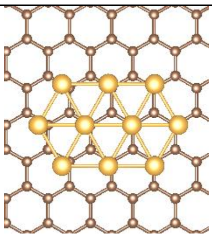	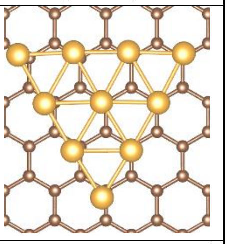
Side	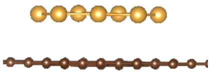	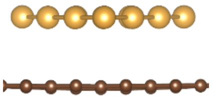
ΔE [eV]	0.00	+0.70

Table S 28: Structures of Au_{11}/C.

	Au_{11}[11-0]$_a$	Au_{11}[11-0]$_b$
Top	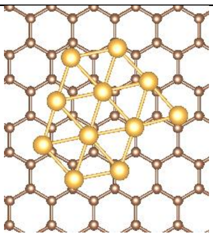	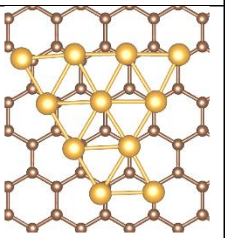
Side	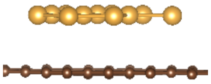	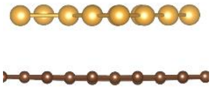
ΔE [eV]	0.00	+0.46

Table S 29: Structures of Au_{12}/C.

	Au_{12}[12-0]
Top	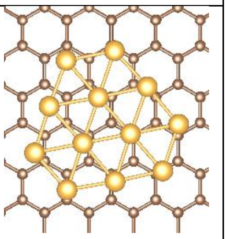
Side	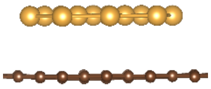
ΔE [eV]	0.00

Table S 30: Structures of Au$_{13}$/C.

	Au$_{13}$[13-0]
Top	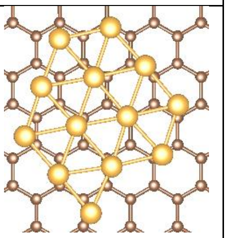
Side	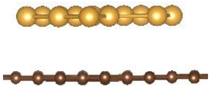
ΔE [eV]	0.00

Table S 31: Structures of Au$_{14}$/C.

	Au$_{14}$[14-0]
Top	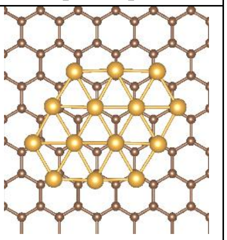
Side	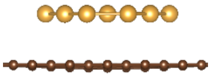
ΔE [eV]	0.00

Table S 32: Structures of Au_{15}/C.

	Au_{15}[15-0]
Top	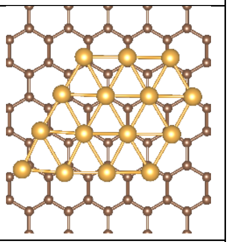
Side	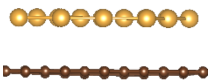
ΔE [eV]	0.00

Table S 33: Structures of Au_{16}/C.

	Au_{16}[16-0]$_a$	Au_{16}[16-0]$_b$	Au_{16}[10-6]
Top	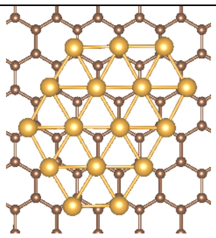	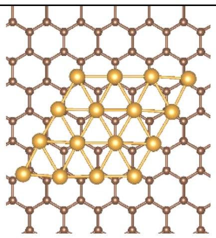	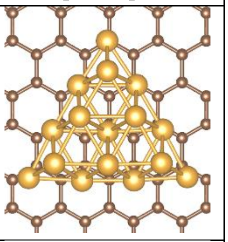
Side	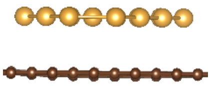	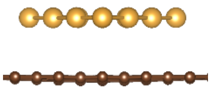	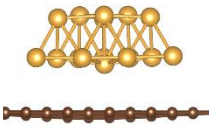
ΔE [eV]	0.00	+0.38	+0.50

Table S 34: Structures of Au$_{17}$/C.

	Au$_{17}$[17-0]$_a$	Au$_{17}$[17-0]$_b$	Au$_{17}$[10-7-1]
Top	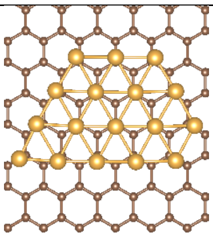	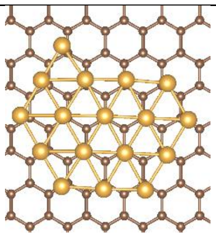	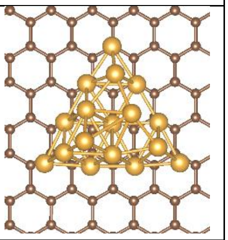
Side	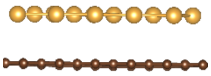	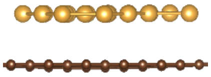	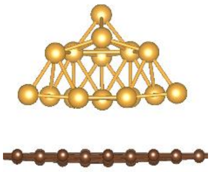
ΔE [eV]	0.00	+0.23	+0.15 (+0.34 with optB88)

Table S 35: Structures of Au$_{19}$/C.

	Au$_{19}$[10-6-3]	Au$_{19}$[19-0]$_a$	Au$_{19}$[19-0]$_b$
Top	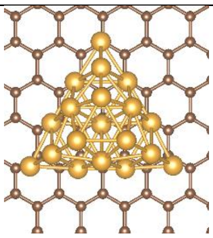	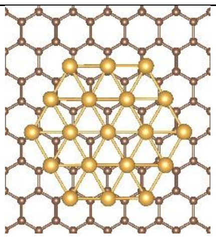	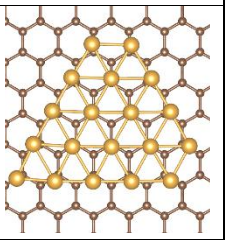
Side	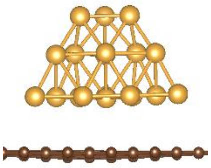	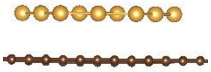	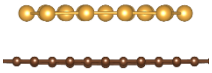
ΔE [eV]	0.00	+0.64 (+0.46 with optB88)	+0.84

Structure of Au/CeO$_2$:

The pristine oxygen-terminated (111) surface of CeO$_2$ has three distinct accessible atoms exposed on the surface. These are an oxygen atom from the highest atomic layer, a cerium atom from the layer below, and an oxygen atom from the third layer. Previous reports suggested that the minimum energy position of a gold adatom is on top of an oxygen of the first layer (T$_{Oa}$),[15,16] on a bridge position between an oxygen in the first layer and one in the third layer (B$_{Oa\text{-}Ob}$),[17–20] or on a bridge site between an oxygen and a cerium atom (B$_{Oa\text{-}Ce}$).[21] Our calculations indicate that the most stable position is on the B$_{Oa\text{-}Ob}$ position (Au$_1$[1]$_a$), but show only a negligible energy difference of only 0.005 eV to the T$_{Oa}$ position (Au$_1$[1]$_b$). We could not obtain a B$_{Oa\text{-}Ce}$ structure since relaxation to the B$_{Oa\text{-}Ob}$ position occurred during the geometry optimisation procedure. Moreover, we found that the top position over an oxygen atom of the lower layer is disfavoured by +0.31 eV (Au$_1$[1]$_c$) and the one on top of a Ce atom by +0.53 eV (Au$_1$[1]$_d$).

In contrast to magnesia and graphene, addition of a second gold atom does not result in a completely perpendicular arrangement (Au$_2$[1-1]$_a$). Instead the dimer is preferentially tilted towards the surface with a Au–Au–O angle of 163.4° as reported by Teng *et al.*[22] A perpendicular dimer on top of an oxygen of the first layer is 0.22 eV higher in energy (Au$_2$[1-1]$_b$) and the most stable parallel dimer was found to be 0.44 eV higher in energy (Au$_2$[2-0]$_a$).

The most favourable structure of a gold trimer on the CeO$_2$(111) surface is a perpendicular triangular cluster with two gold atoms interacting with oxygen atoms in the uppermost layer (Au$_3$[2-1]$_a$). Due to the mismatch in Au-Au distance (2.77 Å) compared to the O–O distance in the highest layer (4.31 Å), the interface gold atoms are not located directly over the oxygen atoms. The structure is corroborated by previous computational studies.[22–24] A decrease of the interface atoms is strongly disfavoured (Au$_3$[1-2]; +1.67 eV). Parallel triangular structures relaxed during the geometry optimisation procedure to the described lowest energy structure. A linear bent structure (Au$_3$[2-1]$_b$) is +0.54 eV less stable than Au$_3$[2-1]$_a$. Addition of a fourth gold atom gives a tetrahedral Au$_4$ structure with three gold atoms at the interface to the surface and interacting with oxygen atoms in the upper layer and one gold atom above the other three in a second layer (Au$_4$[3-1]).[22,24,25] Perpendicular planar structures were found to be less stable with an energy difference of +1.02 eV (Au$_4$[2-2]$_b$). A parallel planar parallelogram-shaped Au$_4$ structure (Au$_4$[4-0]) is 0.97 eV higher in energy. The structure of the lowest five-atom cluster could not be obtained directly from Au$_4$ by adding another gold atom. Instead of a trigonal bipyramidal Au$_5$ cluster (Au$_5$[3-2]$_b$; +0.12 eV), the most stable structure features a triangular shape with two interface atoms and a linear dimer with one interface atom, which are connected with the atoms in the top layer (Au$_5$[3-2]$_a$). However, a nearly planar trapezoid planar on the ceria surface is only 0.07 eV higher in energy (Au$_5$[5-0]). A perpendicular planar trapezoid cluster (Au$_5$[3-2]$_c$) with three gold atoms at the interface, as reported by Teng *et al.*, was found to be +0.14 eV less stable than Au$_5$[3-2]$_a$.[22] The reason for the unsymmetrical structure Au$_5$[3-2]$_a$ to be energetically lower might be that the strong mismatch between the O–O distance and the Au–Au distance leads to non-optimal overlap of the gold and oxygen orbitals. The structure allows for a more flexible binding to the surface and avoids unfavourable interactions caused by close proximity of gold and ceria atoms. This means that for Au$_5$[3-2]$_a$, the geometry is dominated by the cluster-surface interactions rather than the interactions within the cluster while for the energetically close planar Au$_5$[5-0], the structure is dominated by the Au–Au interactions. Addition of a gold atom to Au$_5$ at the interface gives the most stable Au$_6$ structure (Au$_6$[4-2]$_a$). A planar triangular cluster, adsorbed parallel to the surface and obtainable from Au_5[5-0] upon addition of a gold atom (Au_6[6-0]$_a$) was reported in previous studies as the lowest energy structure.[22] However, it was found to be 0.42 eV higher in energy in our calculations. From Au_6 to Au_7, our results suggest a drastic change in the structure. The most stable structure of Au_7 was found to be a nearly planar hexagonal C_{6v}-symmetric cluster oriented parallel to surface (Au_7[7-0]).[22] The hexagonal symmetry of this cluster fits well to the symmetry of the ceria surface and allows for a good binding of all gold atoms to oxygen atoms in the uppermost layer. A higher D_{6h} symmetry, similar to Au_7[7-0]$_c$/C on graphene, is broken by the gold atom in the middle of this structure which is located slightly above the plane of the other atoms. The special stability of the hexagonal structure is also reflected in the structure of Au_8, in which the additional gold atom is located in a second layer on top of the Au_7 structure. Addition of the gold atom at the interface is +0.83 eV higher in energy (Au_8[8-0]$_a$). A three-dimensional cluster with five interface atoms and three atoms in a second layer (Au_8[5-3]), as described by Teng *et al.*, is according to our calculations +0.24 eV less stable than the most stable arrangement.[22] Slightly lower in energy than Au_8[5-3], and the second stable structure, is a cluster with a distorted triangular six-membered interface layer and two atoms in a second layer (Au_8[6-2]$_b$; +0.20 eV) The star-shaped parallel planar structure as described for graphene (and magnesia) is disfavoured by +0.47 eV with respect to the lowest energy structure. The preferred structure of Au_9 is a C_{3v}-symmetric cluster with a six-membered triangular interface and a three-membered triangular second layer (Au_9[6-3]). Addition of a second atom to the second layer of Au_8[7-1], the favoured structure for Au_8, is +0.45 eV higher in energy (Au_9[7-2]$_a$). To obtain the lowest energy structure of Au_{10} from Au_9[6-3], an additional gold atom is placed in a third layer, resulting in the T_d-symmetric cluster Au_{10}[6-3-1]. For Au_{11}, the six-membered triangular interface layer of Au_{10}[6-3-1] is extended to a seven-membered hexagonal layer (Au_{11}[7-3-1]$_a$). The most stable structure of Au_{12} consists of only two layers of gold atoms with an interface layer of eight atoms and a second layer of four gold atoms (Au_{12}[8-4]). Extension of the three-layered structure of Au_{11} is disfavoured by +0.29 eV. The cluster grows further by addition of gold atoms in the first layer (Au_{13}[9-4]) or second layer (Au_{13}[8-3], +0.07 eV) and further extending the first and second layer until a triangular shape of both layers is reached (Au_{16}[10-6]). Then, the growth of the third layer recommences until for Au_{19}, a nearly tetrahedral shaped C_{3v}-symmetric cluster is formed (Au_{19}[10-6-3]) which was also found to be the most stable cluster structure on graphene.

Table S 36: Structures of Au$_1$/CeO$_2$.

	Au$_1$[1]$_a$	Au$_1$[1]$_b$	Au$_1$[1]$_c$	Au$_1$[1]$_d$
Top	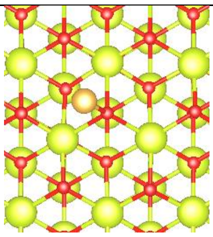	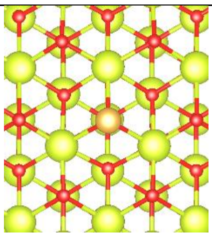	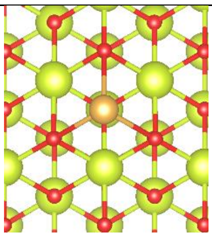	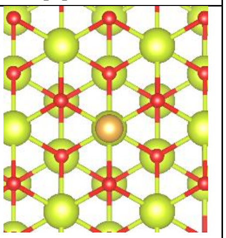
Side		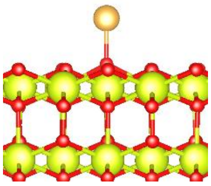	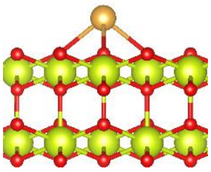	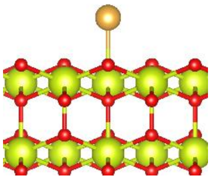
ΔE [eV]	0.00	+0.01	+0.31	+0.53

Table S 37: Structures of Au$_2$/CeO$_2$.

	Au$_2$[1-1]$_a$	Au$_2$[1-1]$_b$	Au$_2$[2-0]$_a$	Au$_2$[2-0]$_b$
Top	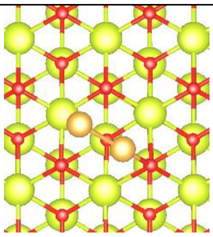	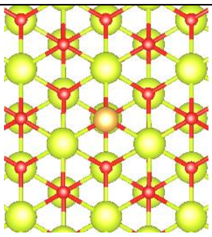	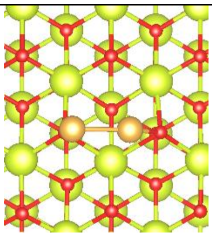	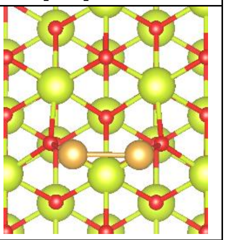
Side	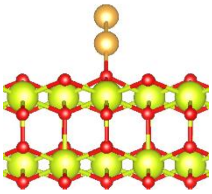	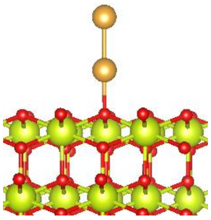	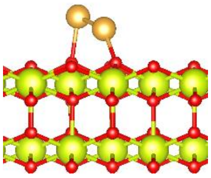	
ΔE [eV]	0.00	+0.22	+0.44	+0.47

Table S 38: Structures of Au_3/CeO_2.

	Au_3[2-1]$_a$	Au_3[2-1]$_b$	Au_3[1-2]
Top	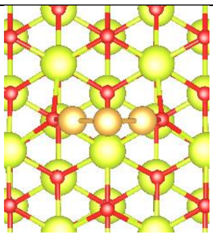	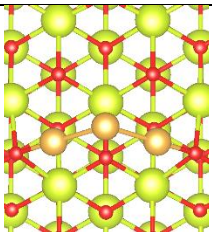	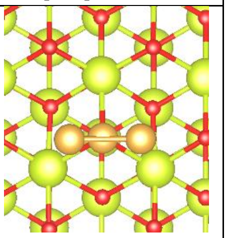
Side	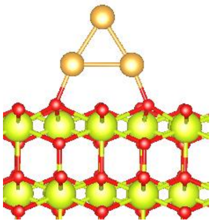	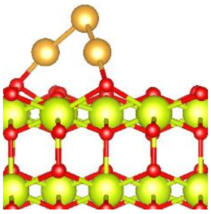	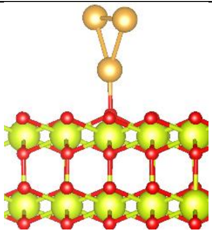
ΔE [eV]	0.00	+0.54	+1.67

Table S 39: Structures of Au_4/CeO_2.

	Au_4[3-1]	Au_4[2-2]$_a$	Au_4[4-0]	Au_4[2-2]$_b$
Top	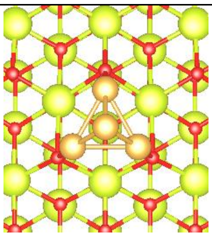	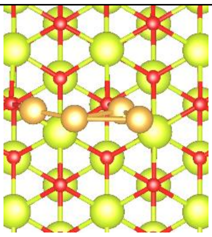	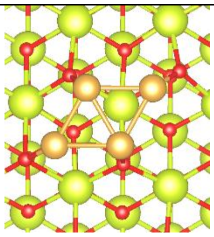	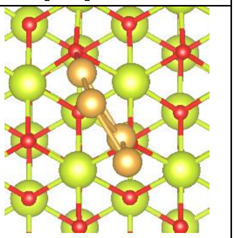
Side	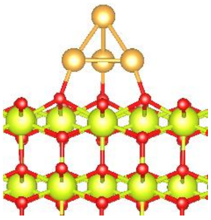	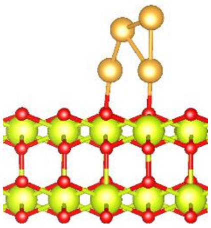	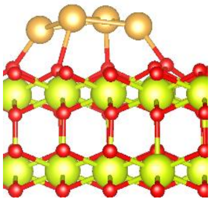	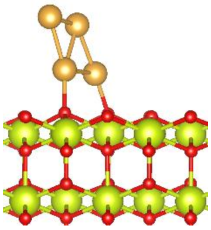
ΔE [eV]	0.00	+1.02	+0.97	+1.02

Table S 40: Structures of Au$_5$/CeO$_2$.

	Au$_5$[3-2]$_a$	Au$_5$[5-0]	Au$_5$[3-2]$_b$	Au$_5$[2-3]	Au$_5$[4-1]	Au$_5$[3-2]$_c$
Top	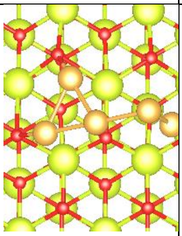	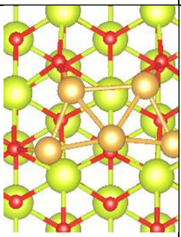	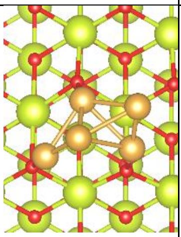	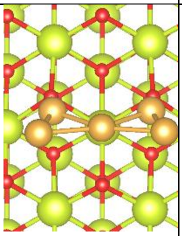	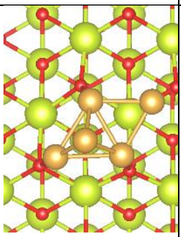	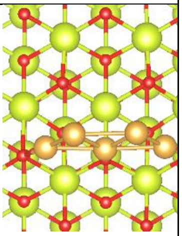
Side	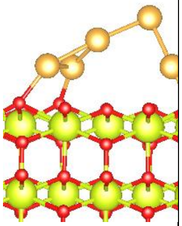	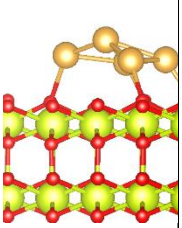	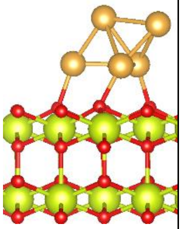	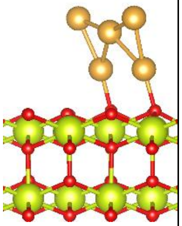	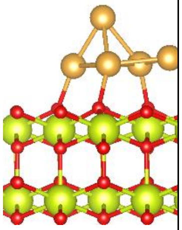	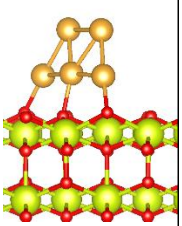
ΔE [eV]	0.00	+0.07	+0.12	+0.62	+0.30	+0.14

Table S 41: Structures of Au$_6$/CeO$_2$.

	Au$_6$[4-2]$_a$	Au$_6$[6-0]$_a$	Au$_6$[4-2]$_b$	Au$_6$[3-2-1]	Au$_6$[6-0]$_b$
Top	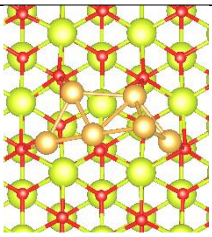	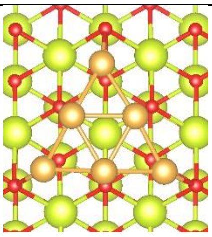	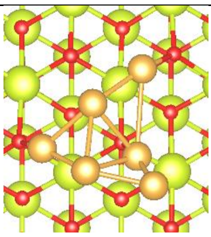	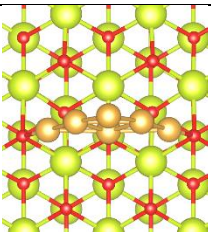	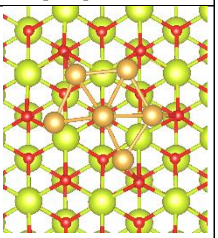
Side	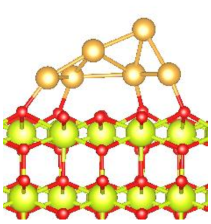	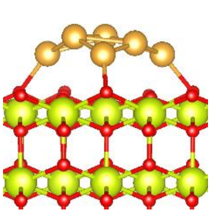	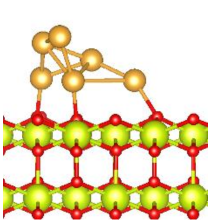	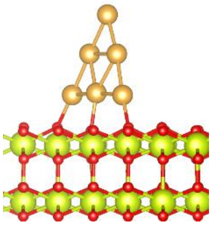	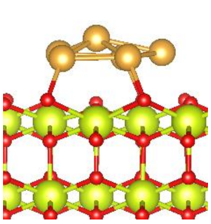
ΔE [eV]	0.00	+0.42	+1.04	+0.78	+0.45

Table S 42: Structures of Au$_7$/CeO$_2$.

	Au$_7$[7-0]	Au$_7$[5-2]$_a$	Au$_7$[6-1]$_a$	Au$_7$[5-2]$_b$	Au$_7$[6-1]$_b$
Top	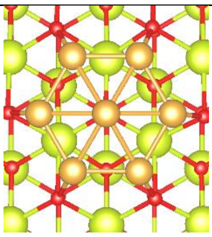	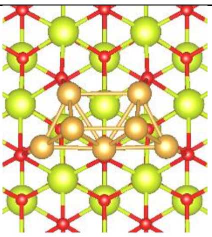	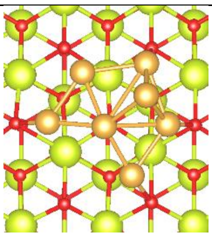	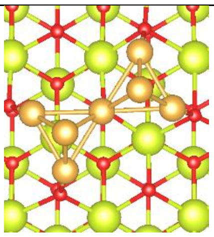	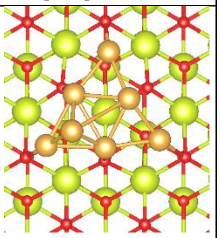
Side	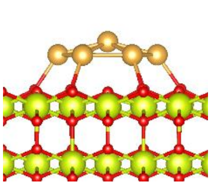	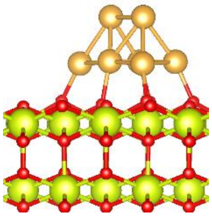	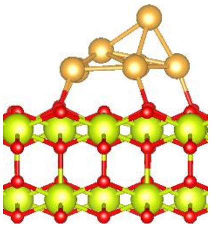	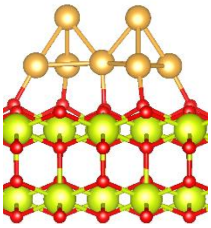	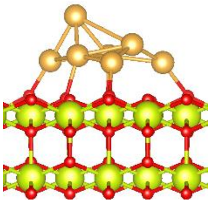
ΔE [eV]	0.00	+0.44	+0.44	+0.52	+0.32

Table S 43: Structures of Au$_8$/CeO$_2$.

	Au$_8$[7-1]	Au$_8$[8-0]$_a$	Au$_8$[8-0]$_b$	Au$_8$[6-2]$_a$	Au$_8$[6-2]$_b$	Au$_8$[5-3]
Top	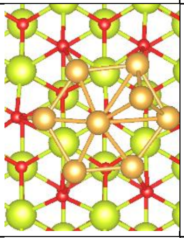	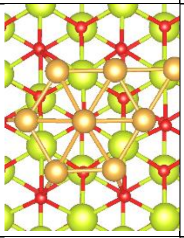	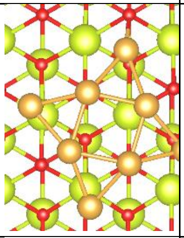	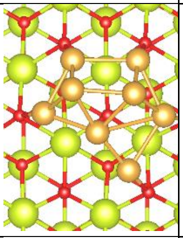	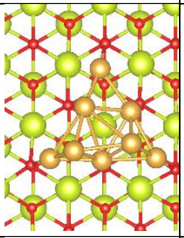	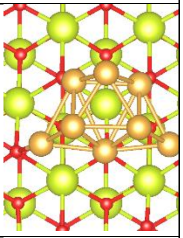
Side	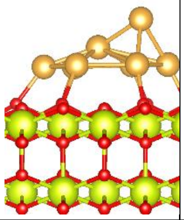	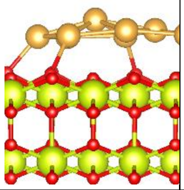	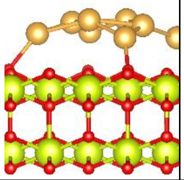	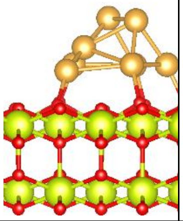	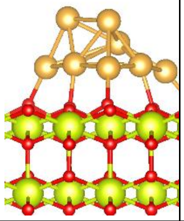	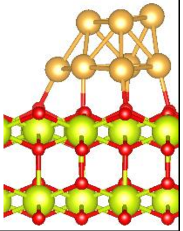
ΔE [eV]	0.00	+0.83	+0.47	+0.38	+0.20	+0.24

Table S 44: Structures of Au$_9$/CeO$_2$.

	Au$_9$[6-3]	Au$_9$[9-0]	Au$_9$[7-2]$_a$	Au$_9$[7-2]$_b$
Top	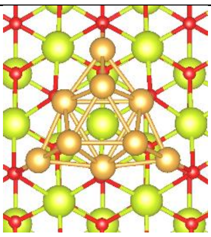	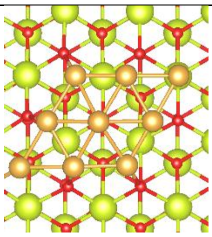	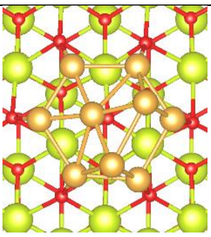	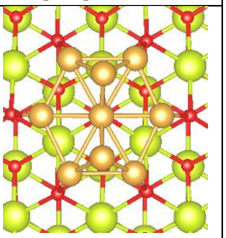
Side	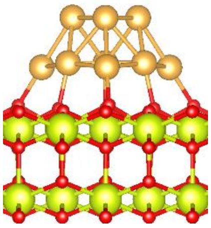	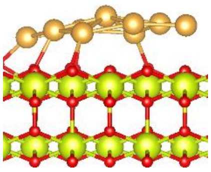	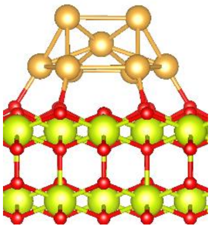	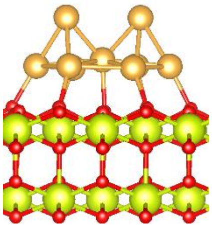
ΔE [eV]	0.00	+1.53	+0.45	+1.08

Table S 45: Structures of Au$_{10}$/CeO$_2$.

	Au$_{10}$[6-3-1]	Au$_{10}$[10-0]$_b$	Au$_{10}$[7-3]	Au$_{10}$[10-0]$_b$
Top	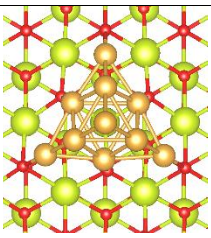	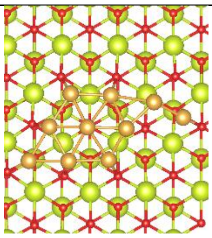	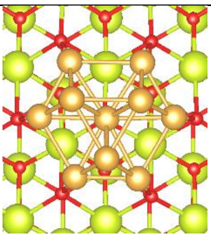	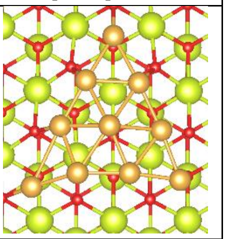
Side	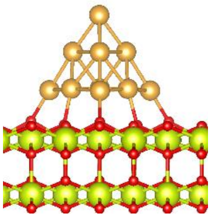	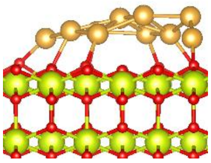	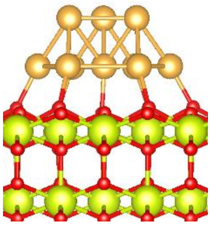	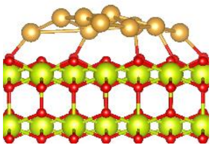
ΔE [eV]	0.00	+1.28	+0.65	+2.06

Table S 46: Structures of Au$_{11}$/CeO$_2$.

	Au$_{11}$[7-3-1]	Au$_{11}$[11-0]	Au$_{11}$[8-3]	Au$_{11}$[7-4]$_a$
Top	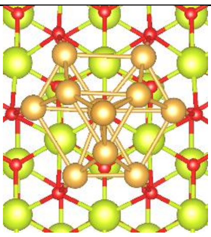	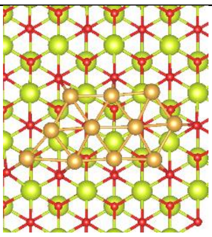	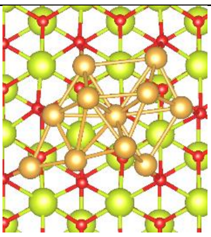	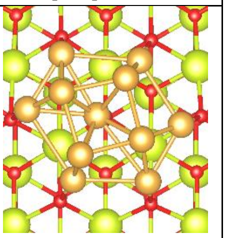
Side	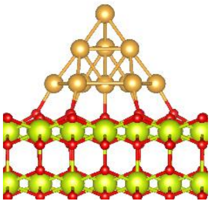	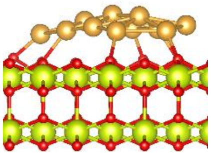	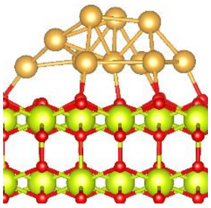	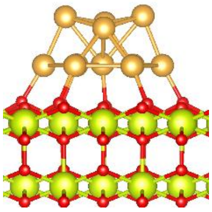
ΔE [eV]	0.00	+1.48	+0.48	+0.35
	Au$_{11}$[6-4-1]	Au$_{11}$[7-3-1]$_b$	Au$_{11}$[7-4]$_b$	
Top	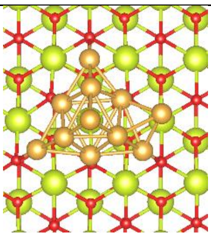	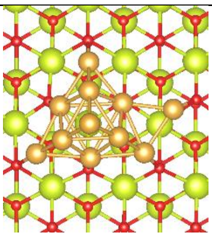	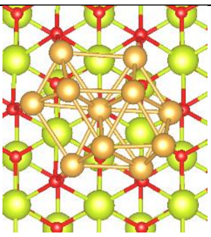	
Side	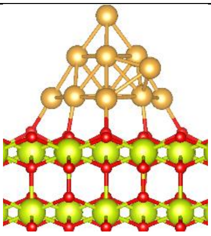	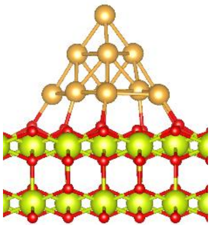	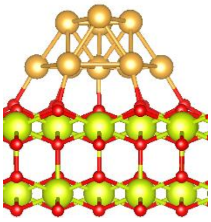	
ΔE [eV]	+0.71	+0.39	+0.48	

Table S 47: Structures of Au$_{12}$/CeO$_2$.

	Au$_{12}$[8-4]	Au$_{12}$[12-0]$_a$	Au$_{12}$[7-5]	Au$_{12}$[12-0]$_b$
Top	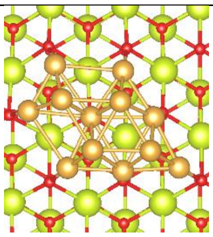	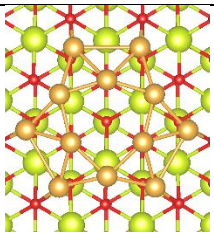	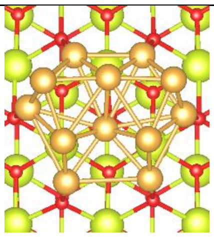	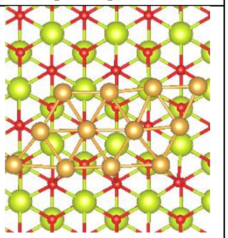
Side	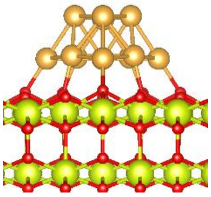	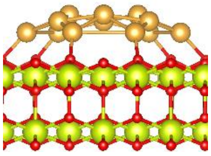	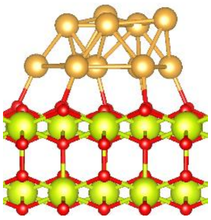	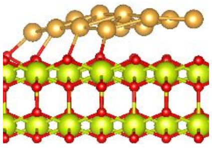
ΔE [eV]	0.00	+1.02	+0.72	+1.74
	Au$_{12}$[12-0]c	Au$_{12}$[7-4-1]	Au$_{12}$[12-0]$_d$	
Top	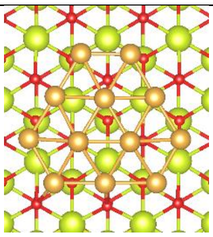	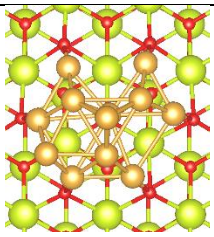	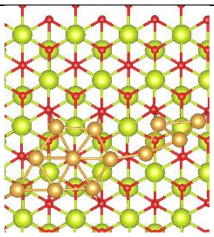	
Side	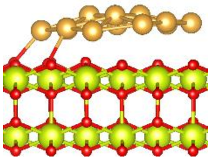	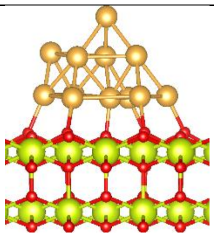	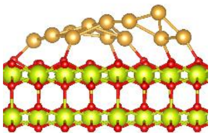	
ΔE [eV]	+0.80	+0.29	+1.83	

Table S 48: Structures of Au$_{13}$/CeO$_2$.

	Au$_{13}$[9-4]	Au$_{13}$[8-5]$_a$	Au$_{13}$[13-0]$_a$	Au$_{13}$[13-0]$_b$	Au$_{13}$[12-1]
Top	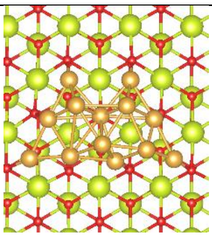	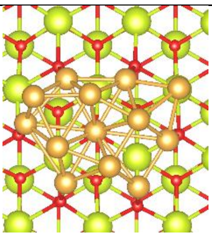	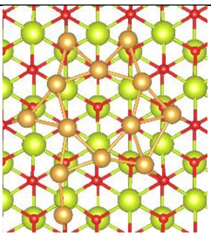	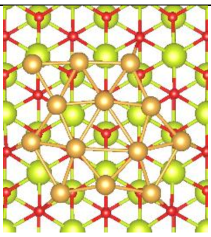	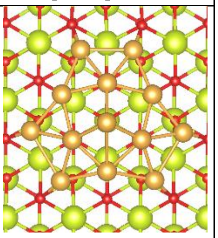
Side	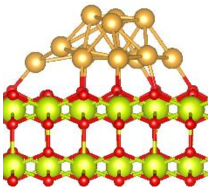	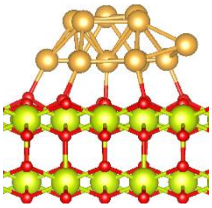	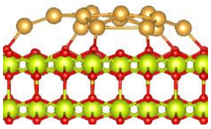	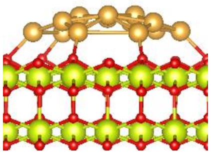	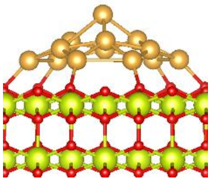
ΔE [eV]	0.00	+0.57	+1.10	+0.99	+0.44
	Au$_{13}$[10-3]	Au$_{13}$[8-5]	Au$_{13}$[7-6]	Au$_{13}$[7-5-1]	
Top	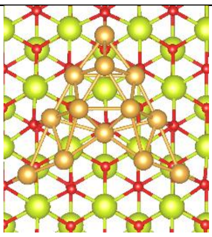	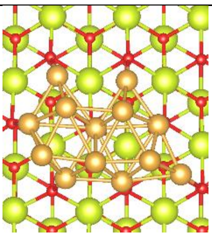	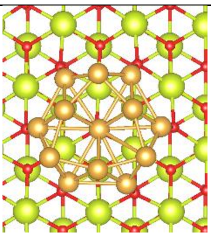	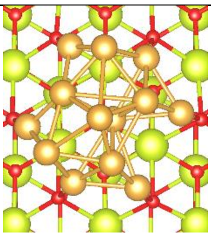	
Side	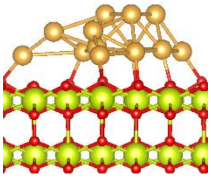	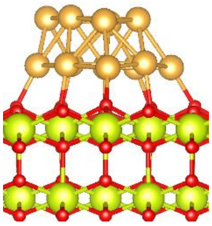	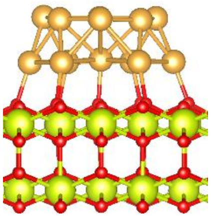	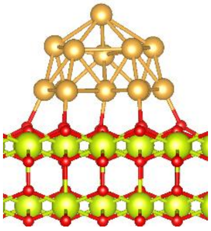	
ΔE [eV]	+0.98	+0.07	+0.18	+0.12	

Table S 49: Structures of Au$_{14}$/CeO$_2$.

	Au$_{14}$[9-5]	Au$_{14}$[8-6]	Au$_{14}$[7-6-1]	Au$_{14}$[10-4]
Top	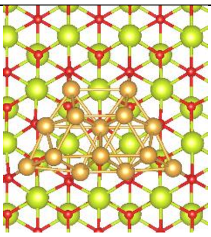	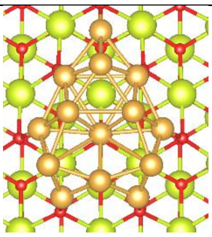	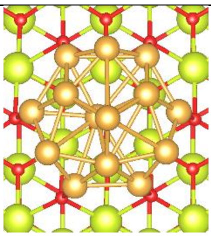	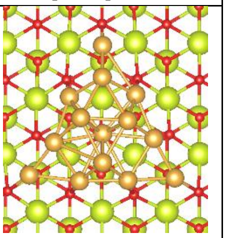
Side	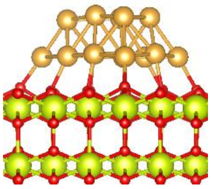	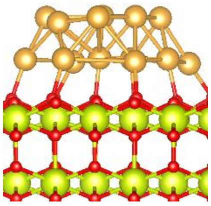	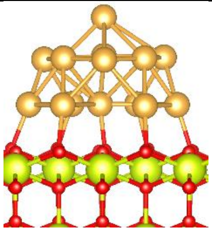	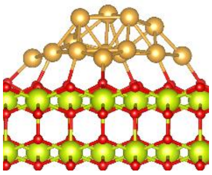
ΔE [eV]	0.00	+0.30	+0.35	+1.03

Table S 50: Structures of Au$_{15}$/CeO$_2$.

	Au$_{15}$[9-6]	Au$_{15}$[7-6-2]	Au$_{15}$[10-5]
Top	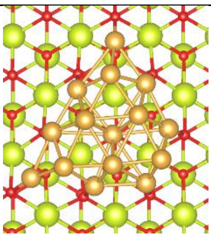	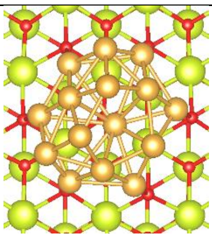	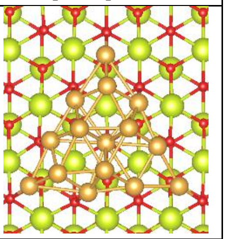
Side	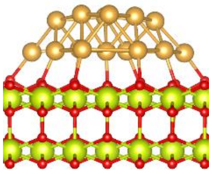	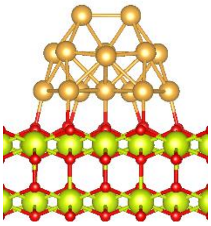	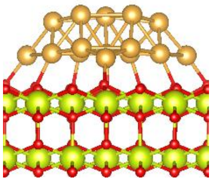
ΔE [eV]	0.00	+0.19	+0.42

Table S 51: Structures of Au_{16}/CeO_2.

	Au$_{16}$[10-6]	Au$_{16}$[7-6-3]	Au$_{16}$[16-0]
Top	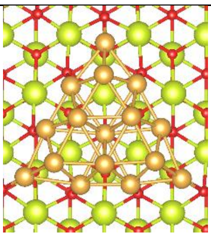	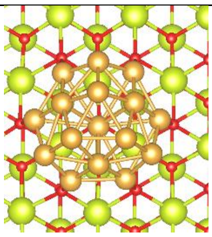	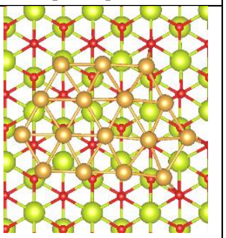
Side	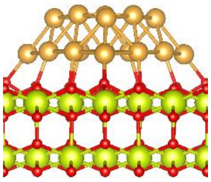	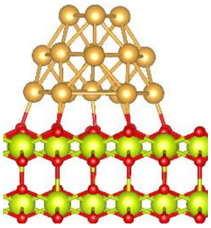	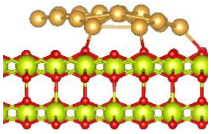
ΔE [eV]	0.00	+0.71	+1.30

Table S 52: Structures of Au_{17}/CeO_2.

	Au$_{17}$[10-6-1]	Au$_{17}$[10-7]	Au$_{17}$[8-6-3]
Top	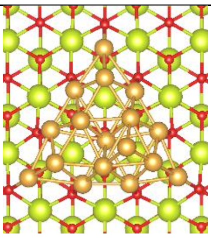	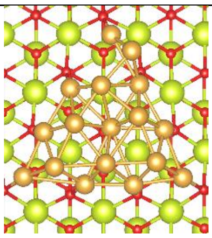	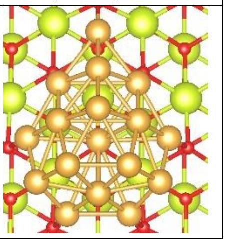
Side	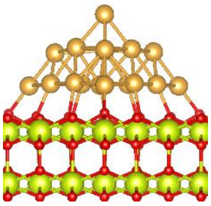	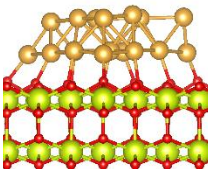	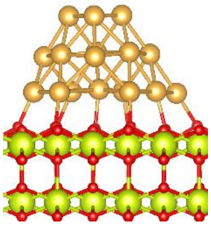
ΔE [eV]	0.00	+0.48	+0.09

Table S 53: Structures of Au_{19}/CeO_2.

	Au_{19}[10-6-3]	Au_{19}[19-0]$_a$	Au_{19}[19-0]$_b$
Top	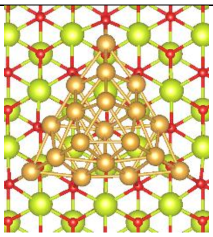	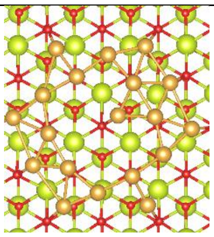	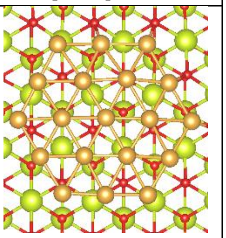
Side	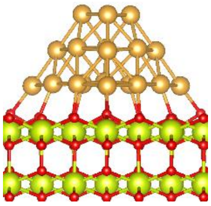	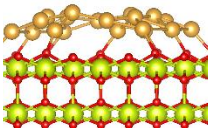	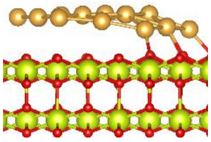
ΔE [eV]	0.00	+3.90	+2.04

2. Structures of isolated Au clusters

The structure of isolated Au clusters is strongly dependent on the computational method. Therefore, we recalculated the energy of previously reported cluster structures to identify the 2D to 3D transition for our computational model.

Table S 54: Structures of Au_3.

	Planar1	Planar2
Structure		
ΔE (PBE) [eV]	+0.11	0.00
ΔE (PBED3) [eV]	+0.12	0.00
ΔE (optB88) [eV]	+0.10	0.00

Table S 55: Structures of Au_4.

	Planar1	Planar2	threeD1
Structure	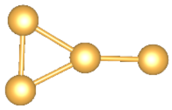	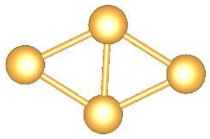	
ΔE (PBE) [eV]	+0.03	0.00	--
ΔE (PBED3) [eV]	+0.04	0.00	--
ΔE (optB88) [eV]	+0.06	0.00	--

Table S 56: Structures of Au_5.

	Planar1	threeD1
Structure	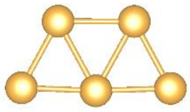	
ΔE (PBE) [eV]	0.00	--
ΔE (PBED3) [eV]	0.00	--
ΔE (optB88) [eV]	0.00	--

Table S 57: Structures of Au_6.

	Planar1	threeD2
Structure	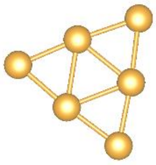	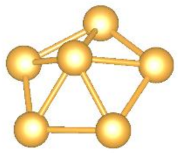
ΔE (PBE) [eV]	0.00	+0.93
ΔE (PBED3) [eV]	0.00	+0.86
ΔE (optB88) [eV]	0.00	+0.86

Table S 58: Structures of Au_7.

	Planar1	Planar2	Planar3	threeD1
Structure	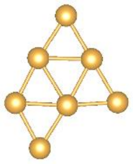	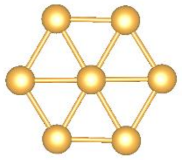	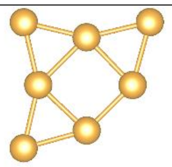	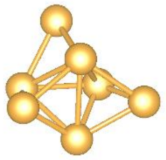
ΔE (PBE) [eV]	0.00	+0.29	+0.12	+0.54
ΔE (PBED3) [eV]	0.00	+0.27	+0.08	+0.44
ΔE (optB88) [eV]	0.00	--	--	--
	threeD2	threeD3	threeD4	
Structure	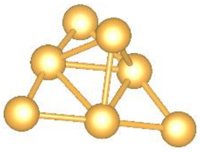	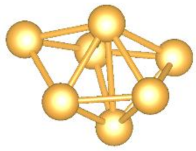	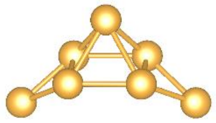	
ΔE (PBE) [eV]	+0.40	+0.70	+0.70	
ΔE (PBED3) [eV]	+0.26	+0.46	+0.61	
ΔE (optB88) [eV]	+0.29	--	--	

Table S 59: Structures of Au_8.

	Planar1	Planar2	threeD1	threeD2
Structure	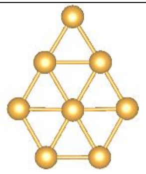	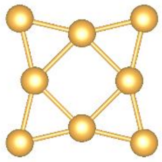	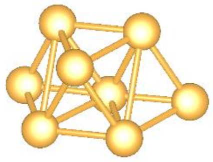	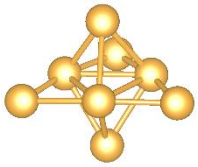
ΔE (PBE) [eV]	+0.32	0.00	+0.52	--
ΔE (PBED3) [eV]	+0.34	0.00	+0.32	+0.85
ΔE (optB88) [eV]	--	0.00	+0.27	+0.89

Table S 60: Structures of Au$_9$.

	Planar1	Planar2	Planar3	threeD1
Structure	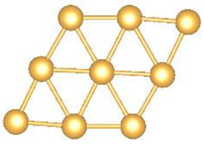	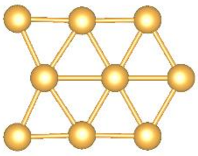	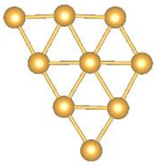	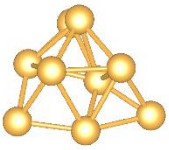
ΔE (PBE) [eV]	+0.16	0.00	+0.09	+0.56
ΔE (PBED3) [eV]	+0.17	0.00	+0.10	+0.29
ΔE (optB88) [eV]	--	0.00	+0.09	--
	threeD2			
Structure	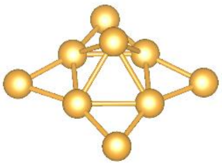			
ΔE (PBE) [eV]	+0.25			
ΔE (PBED3) [eV]	+0.11			
ΔE (optB88) [eV]	+0.16			

Table S 61: Structures of Au$_{10}$.

	Planar1	Planar2	threeD1	threeD2
Structure	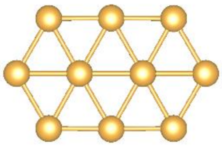	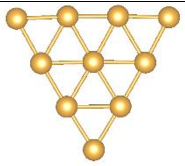	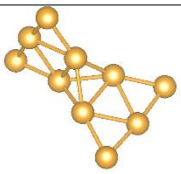	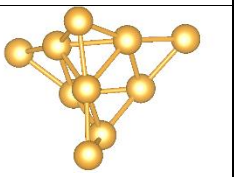
ΔE (PBE) [eV]	0.00	+0.86	+0.39	+0.27
ΔE (PBED3) [eV]	0.00	+0.84	+0.41	+0.01
ΔE (optB88) [eV]	0.00	--	--	+0.14
	threeD3	threeD4	threeD5	
Structure	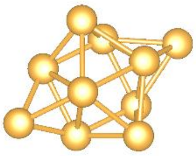	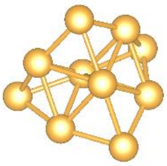	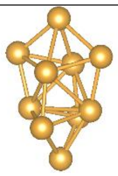	
ΔE (PBE) [eV]	+0.62	+1.41	+0.86	
ΔE (PBED3) [eV]	+0.21	+1.02	+0.57	
ΔE (optB88) [eV]	--	--	--	

Table S 62: Structures of Au_{11}.

	Planar1	Planar2	Planar3	threeD1
Structure	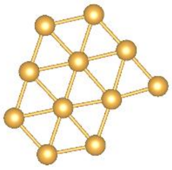	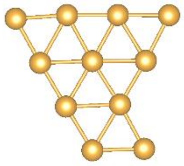	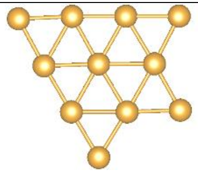	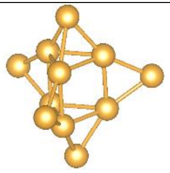
ΔE (PBE) [eV]	0.00	+0.50	+0.24	+0.10
ΔE (PBED3) [eV]	+0.17	+0.70	+0.43	0.00
ΔE (optB88) [eV]	+0.06	--	--	0.00
	threeD2	threeD3	threeD4	
Structure	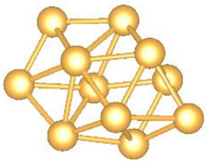	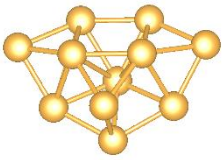	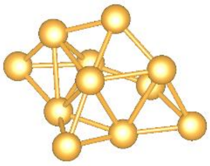	
ΔE (PBE) [eV]	+0.76	+0.62	+0.73	
ΔE (PBED3) [eV]	+0.46	+0.25	+0.50	
ΔE (optB88) [eV]	--	--	--	

3. Detachment Energy

The detachment energy (E_{det}) gives the stability of the cluster towards the detachment of a single gold atom and the formation of a cluster with one atom less and was calculated using

$$E_{det} = E_{Au(n-1)-S} + E_{Au1-S} - E_{Aun-S} - E_S$$

The detachment energy (E_{det}) describes the energy which is required for the abstraction of a metal atom from the metal cluster. For magnesia and graphene, E_{det} shows a clear odd-even oscillation with higher energy for even-numbered clusters as reported previously for gas phase structures.[14,26–29] This indicates a higher stability of the even-numbered closed shell clusters over odd-numbered ones as it takes more energy to remove a gold atom from even-numbered clusters. In contrast to this, no clear trend is recognisable for ceria. On the one hand, this behaviour might be a result of the stronger influence of the support-cluster interactions on the cluster stability which may be dominating the structure making the relative stability of the electronic structure of the cluster negligible. On the other hand, localisation of the unpaired electron at a cerium 4f orbital as known from the literature and can be significantly favoured over localisation at the gold cluster.

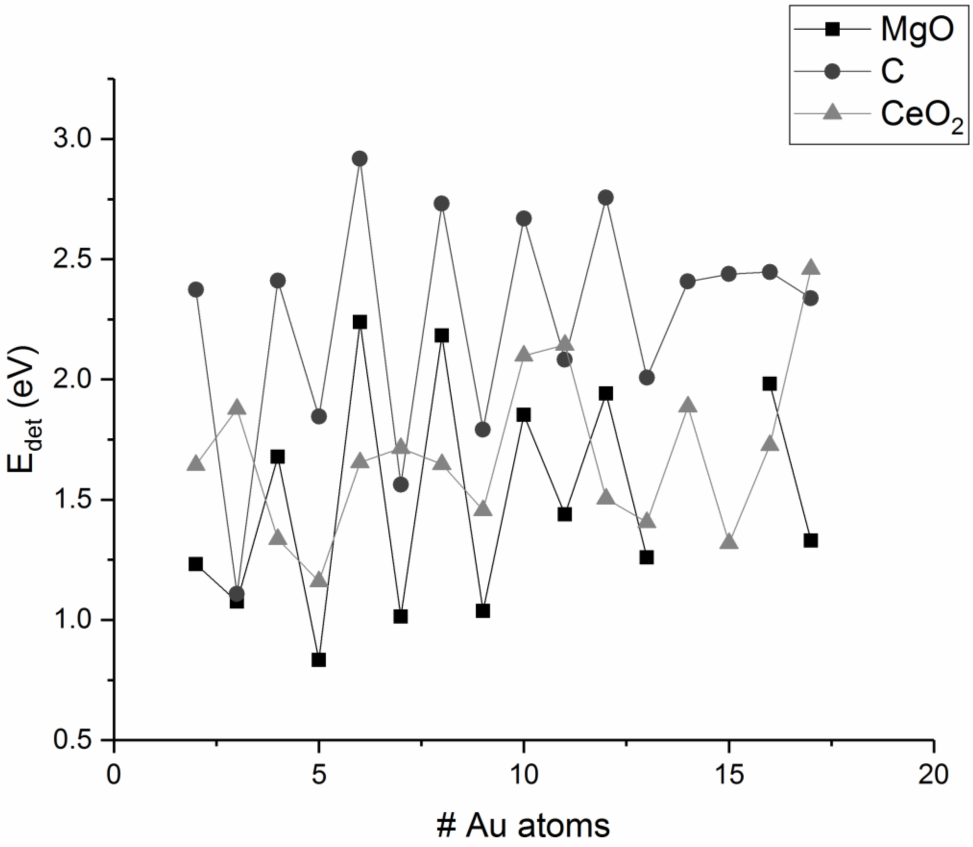

Figure S 1: Detachment energies of Au clusters supported on MgO, C, and CeO_2.

4. Electrostatic Potential

The electrostatic potential was calculated as implemented in VASP.[30] The energies reported here correspond to the energies of a particle with a charge of −e within the electrostatic potential V(r).

$$V(r) = \sum_A \frac{Z_A}{|R_A - r|} - \int \frac{\rho(r')dr'}{|r' - r|}$$

Brinck and co-workers previously reported regions of low electron density at the corners of isolated gold clusters (σ-holes).[31–33] We analysed the electrostatic potential on an isosurface of the electron density at 0.001 a.u..[34] The plots show σ-holes at corner atoms as previously reported for gold clusters in the gas phase by Brinck and co-workers.[31–33] The electrostatic potential can give an indication for preferred electrostatic interaction sites but it has to be remarked that it is not always reliable for the description of chemical reactivity.[34]

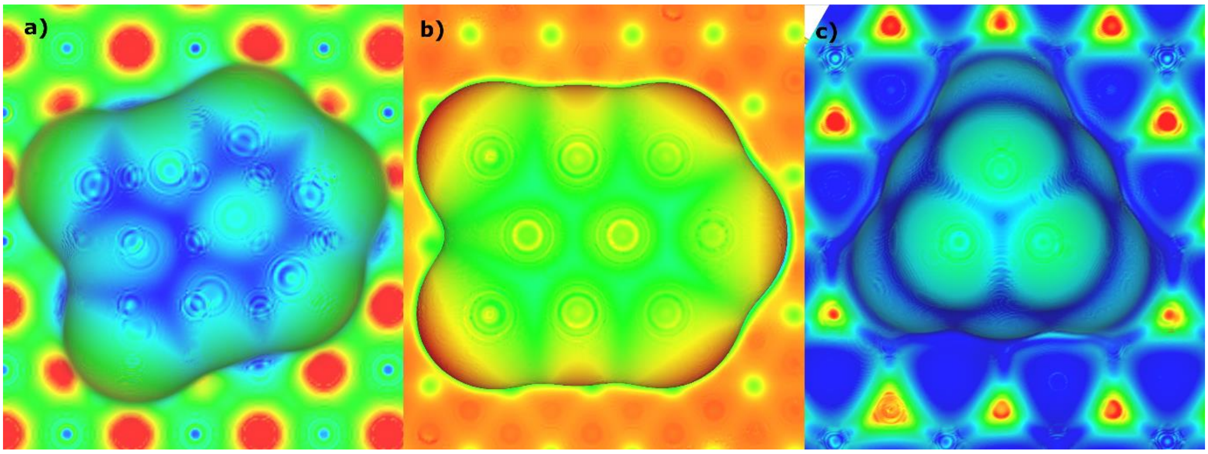

Figure S 2: Electron density of Au_9 on MgO (a), graphene (b), and CeO_2 (c); isosurface at 0.001 a.u. mapped with the (electrostatic) local potential; colour scale between ≥0 eV (blue) and ≤−2.5 eV (red).

5. COHP Plots

DOS and COHP plots are visualised with wxDragon 2.1.0.[35]

5.1 Surfaces

5.1.1 MgO

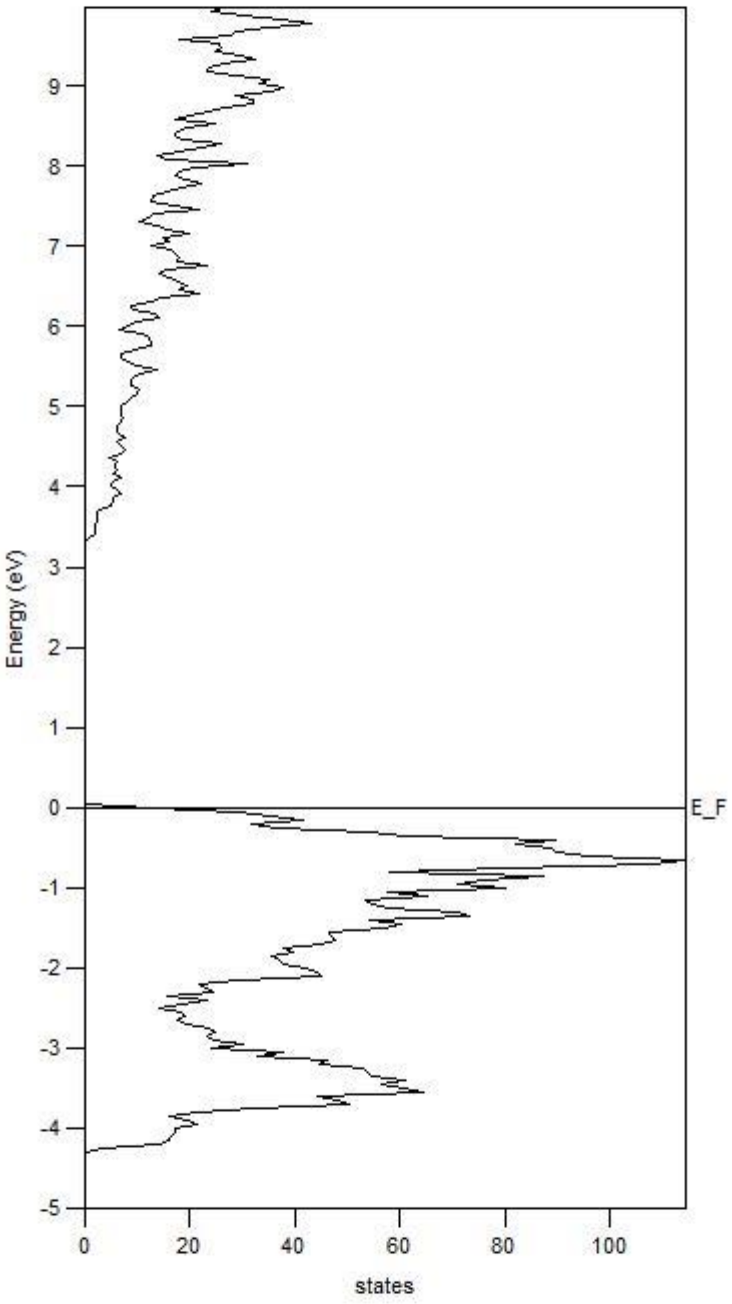

Figure S 3: DOS of MgO(001).

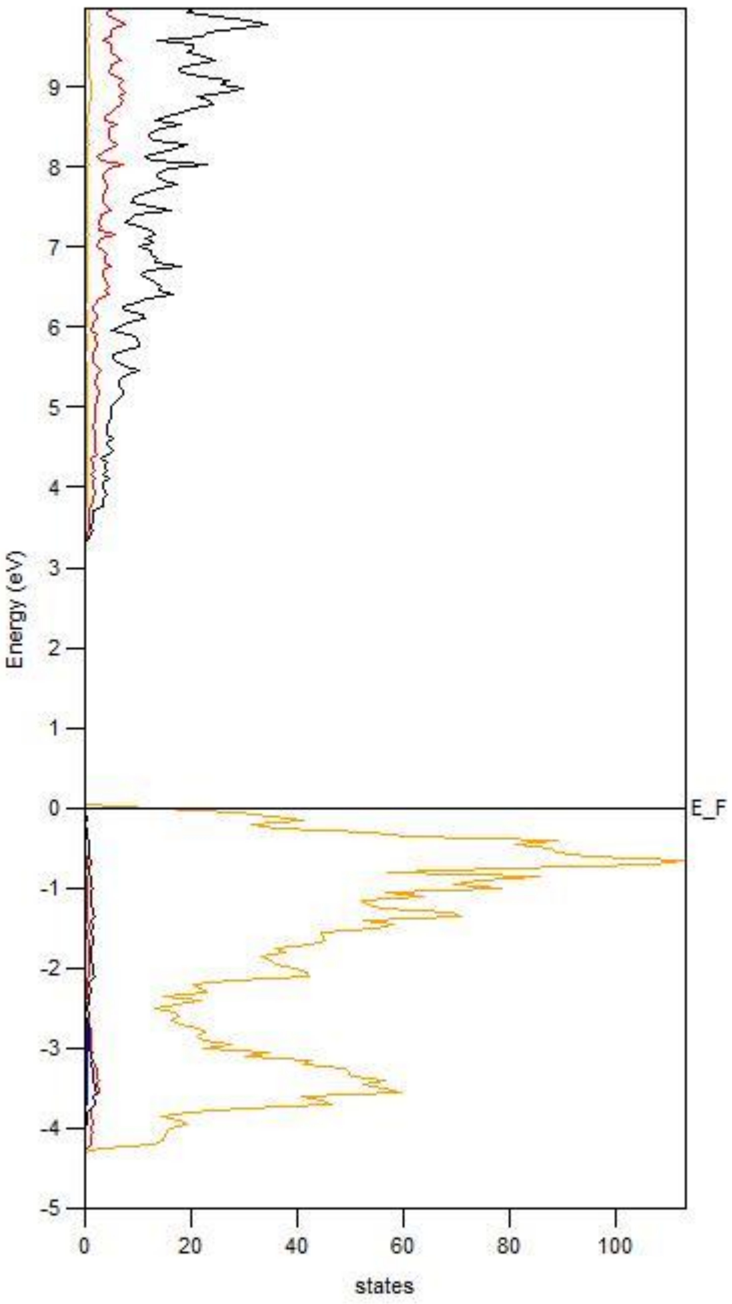

Figure S 4: pDOS of MgO(001); Mg(s) orbitals (red), Mg(p) orbitals (black), O(s) orbitals (blue), O(p) orbitals (yellow).

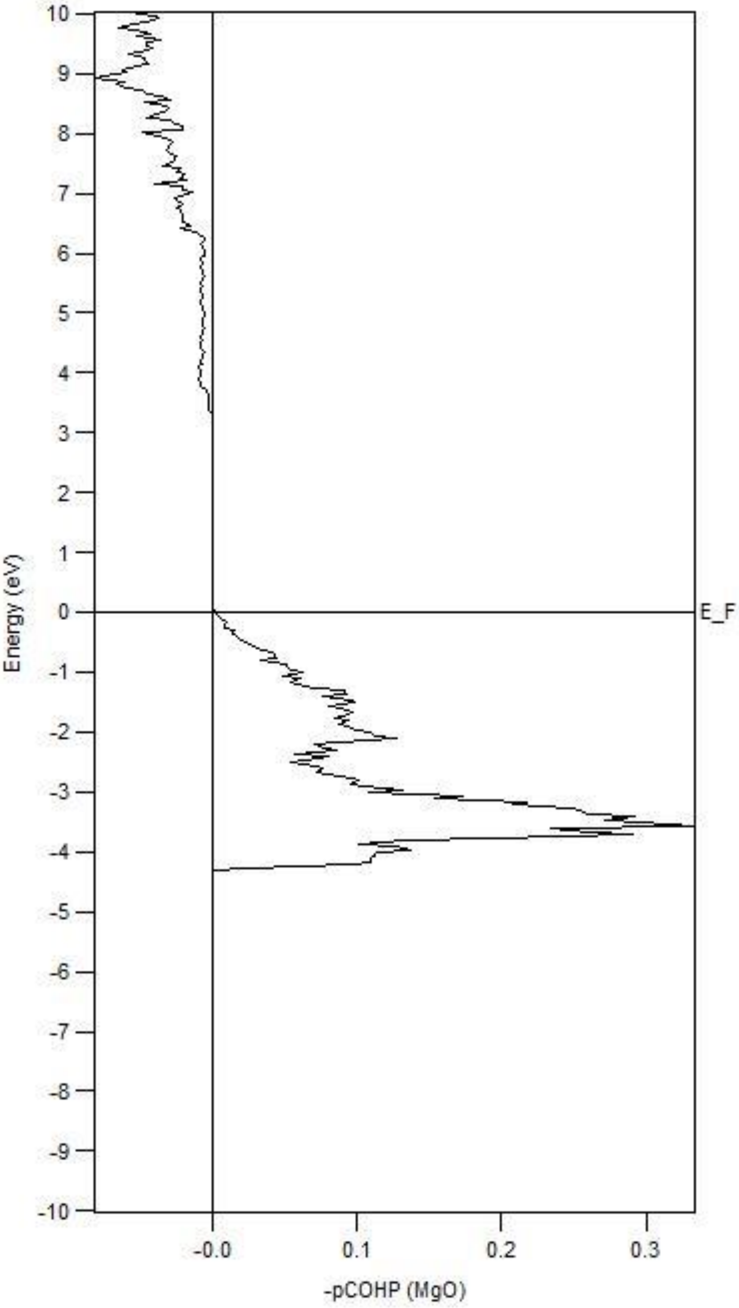

Figure S 5: Average pCOHP (Mg-O) of MgO; pairs within 3.0 Å.

5.1.2 C

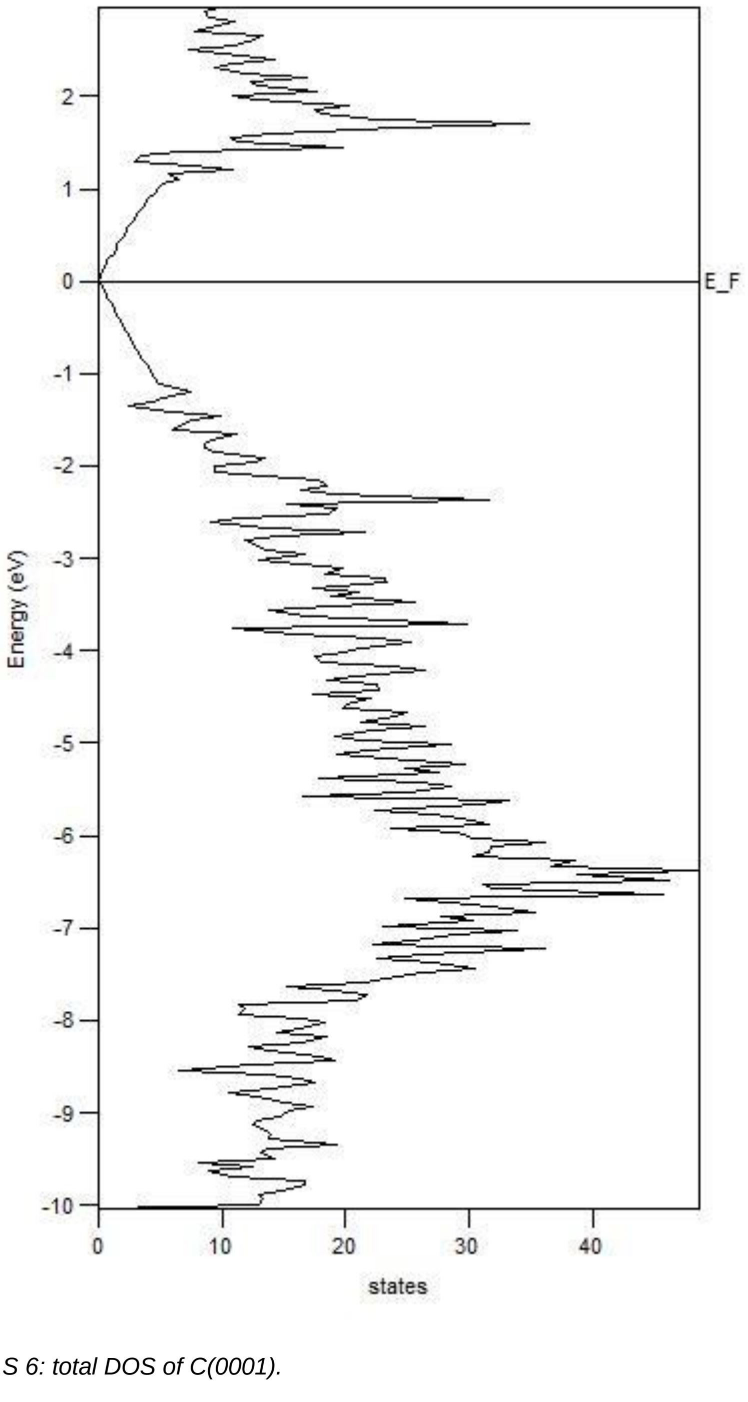

Figure S 6: total DOS of C(0001).

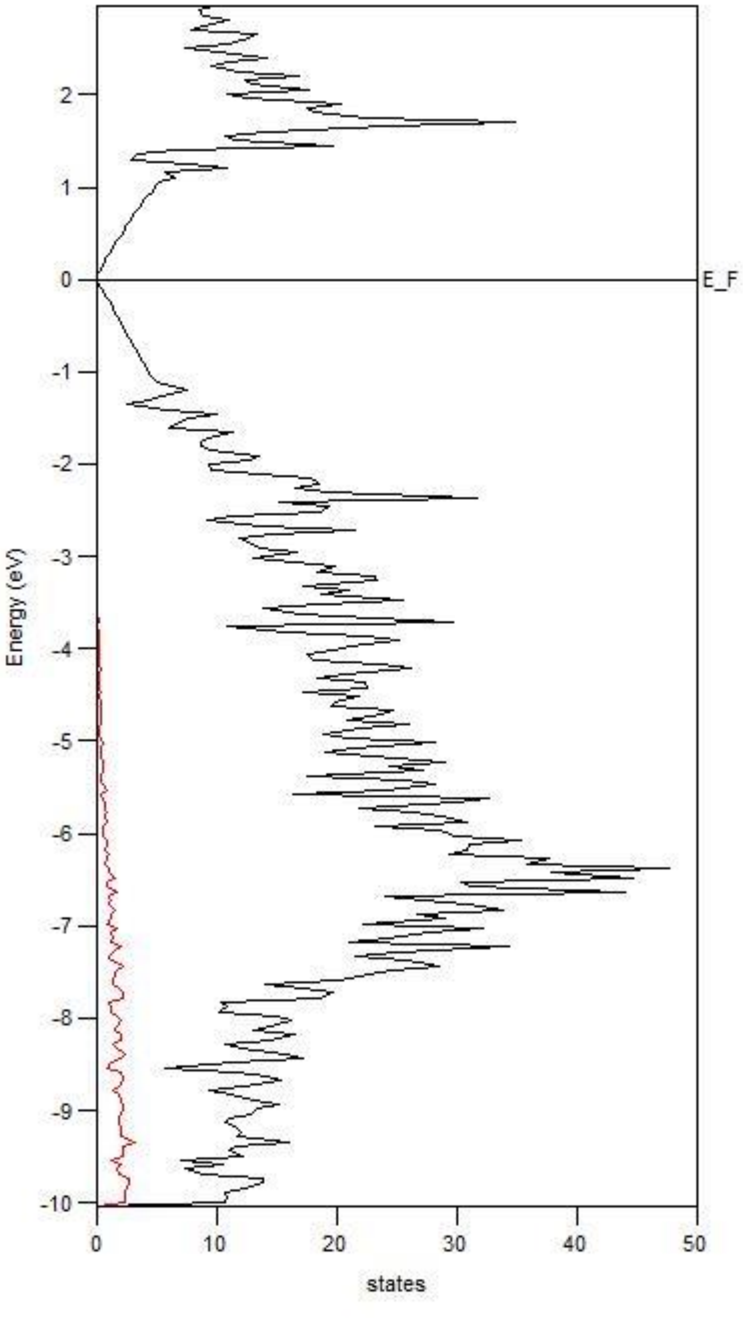

Figure S 7: pDOS of C(0001); C(s) orbitals (red), C(p) orbitals (black).

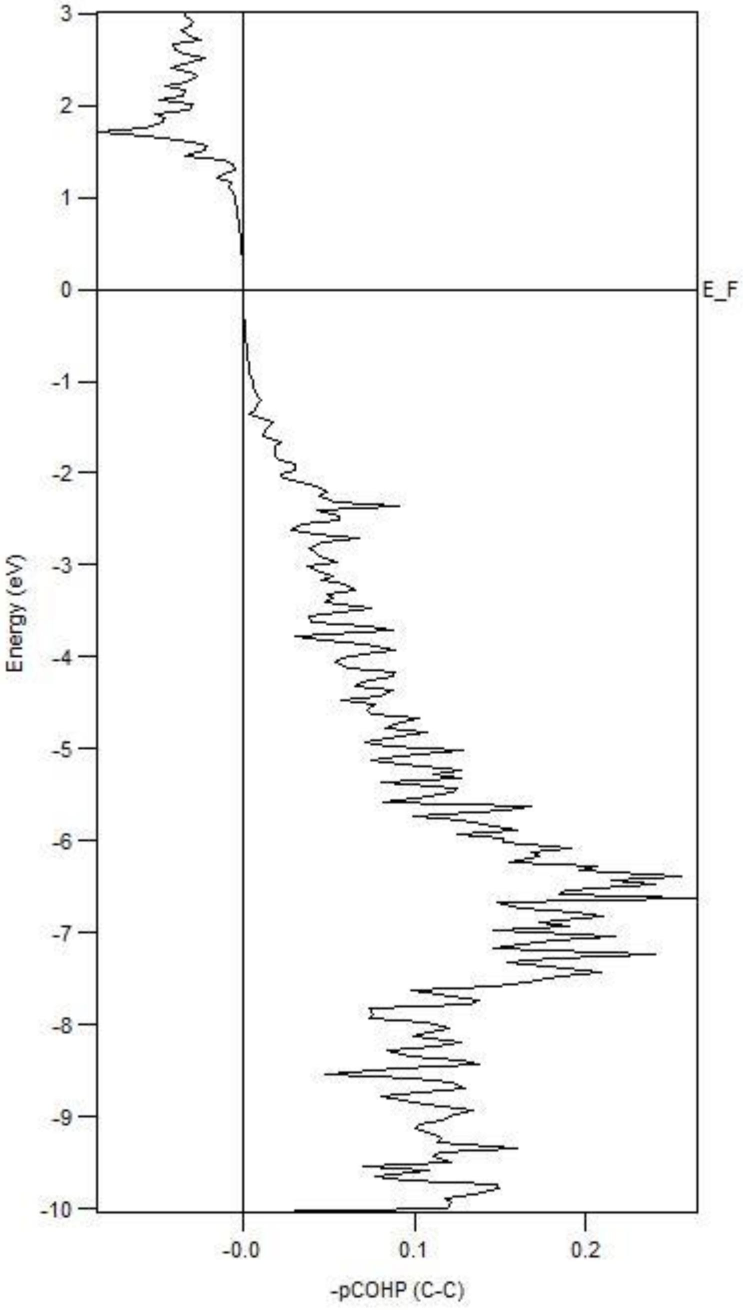

Figure S 8: Average pCOHP (C-C) of C; pairs within 3.0 Å.

5.1.3 CeO_2

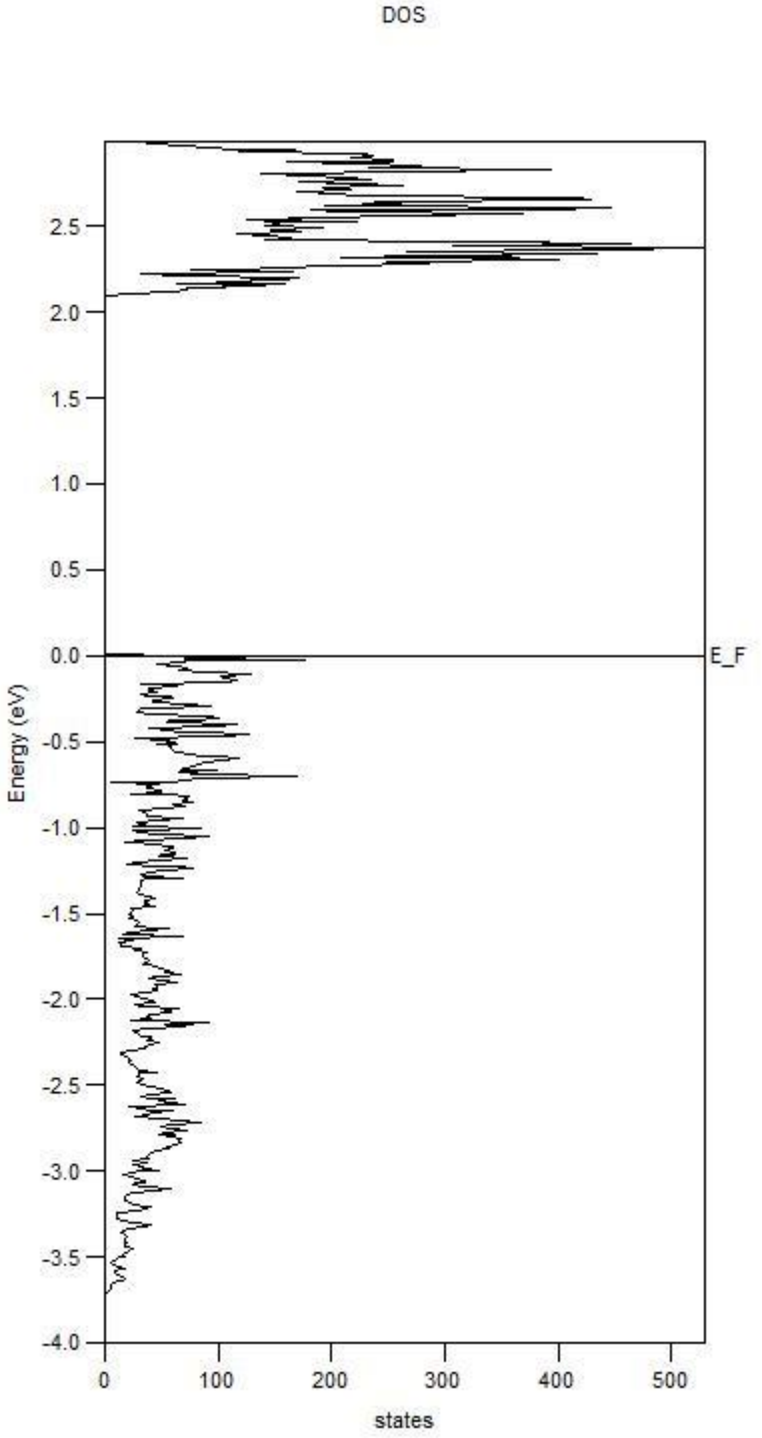

Figure S 9: total DOS of CeO_2 *(111).*

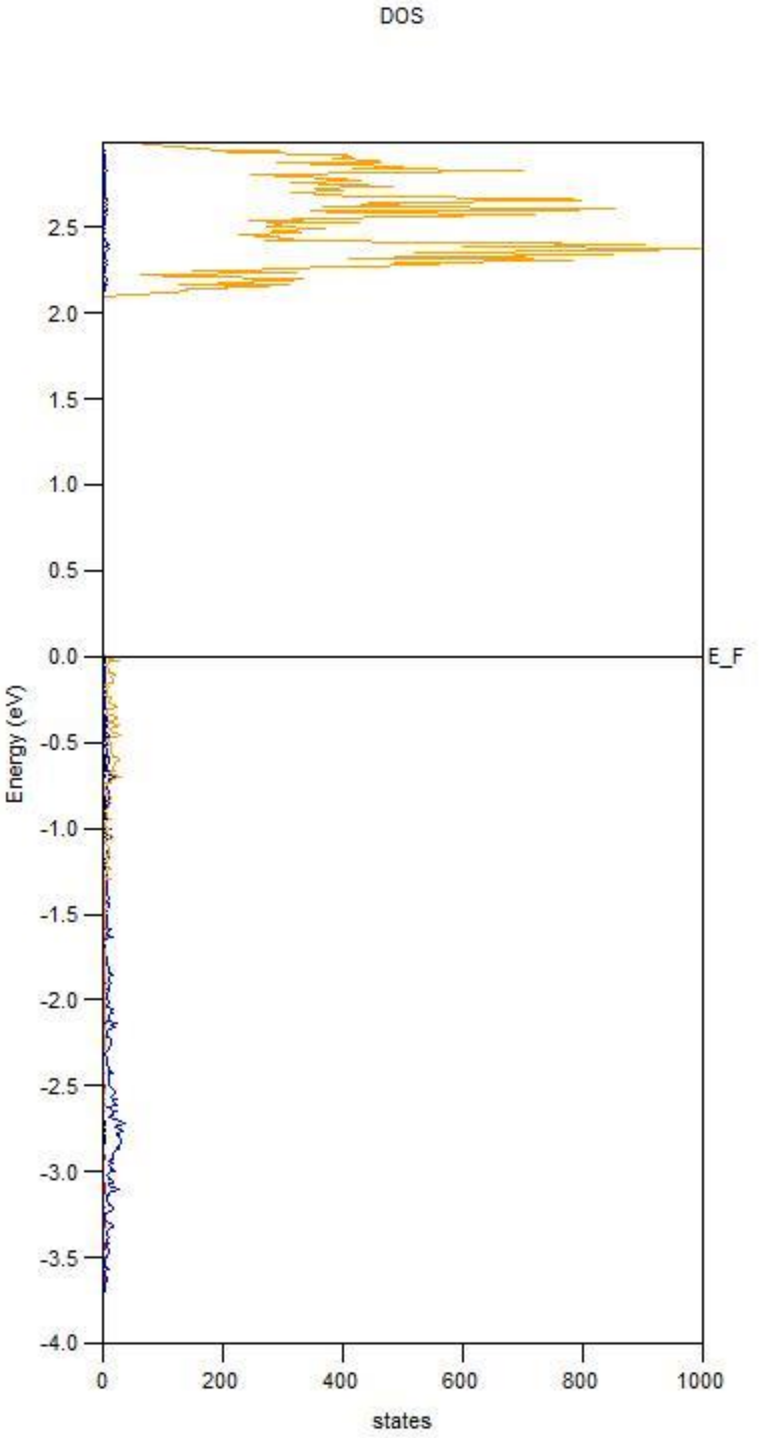

Figure S 10: pDOS of CeO_2(111); Ce(s) orbitals (red), Ce(p) orbitals black), Ce(d) orbitals (blue), Ce(f) orbitals (yellow).

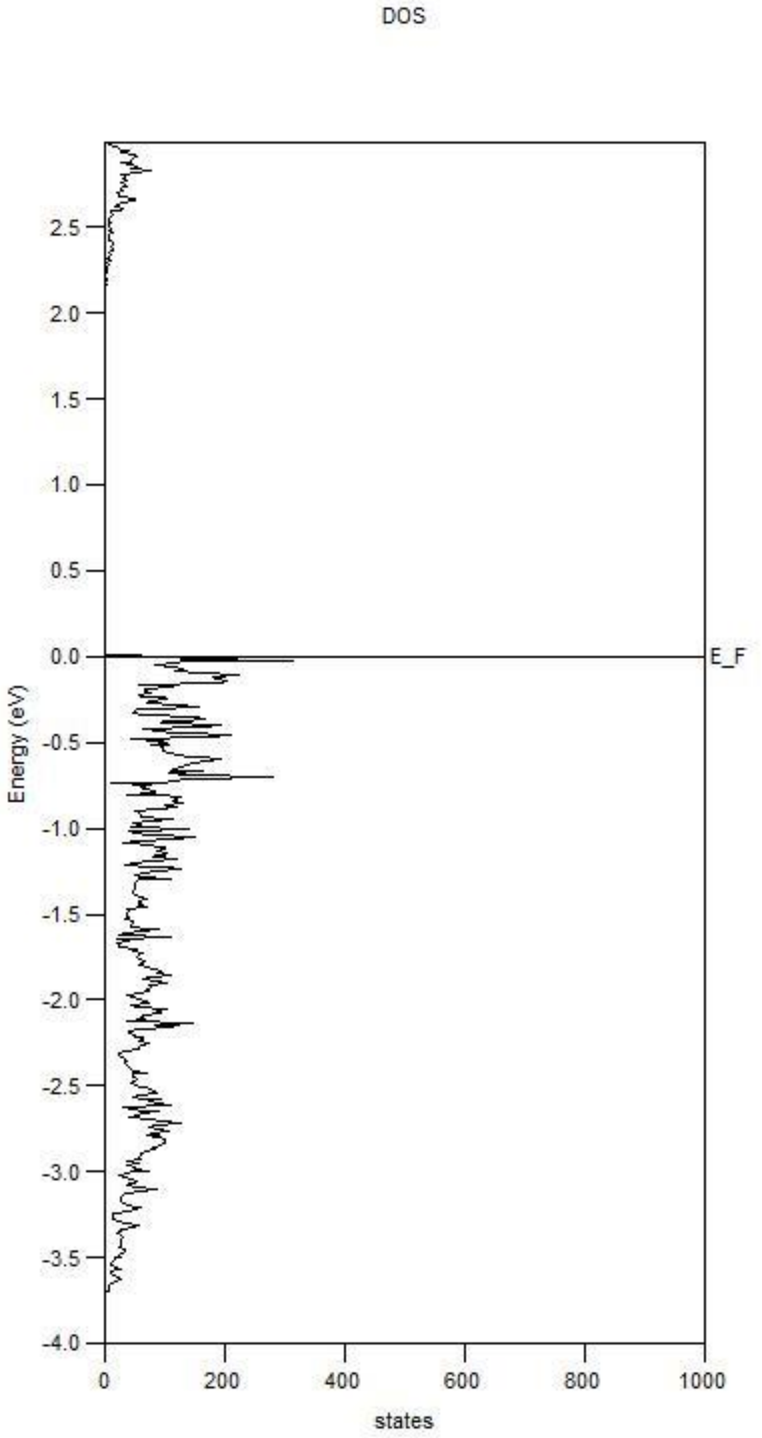

Figure S 11: pDOS of CeO_2*(111); O(s) (red), O(p) (black).*

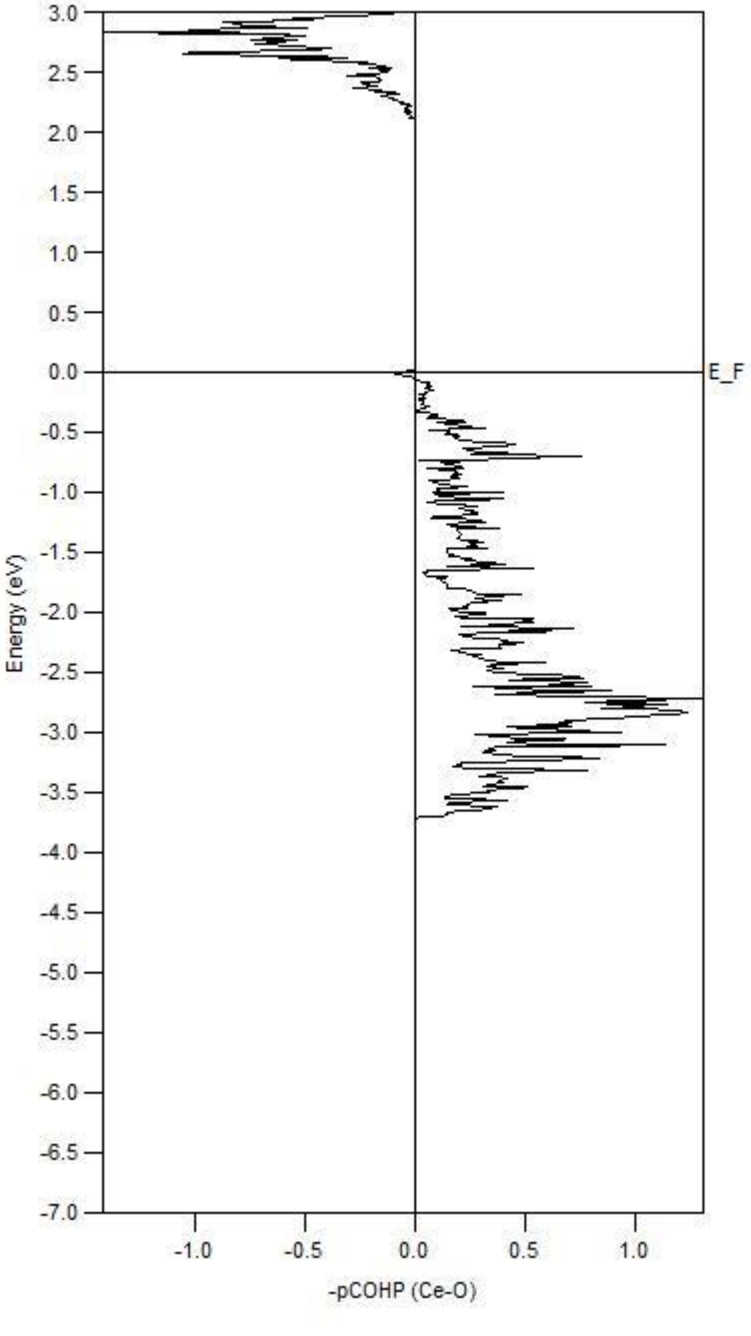

Figure S 12: Average pCOHP (Ce-O) of CeO_2; pairs within 3.0 Å.

5.2 Isolated Au clusters

5.2.1 Au_3

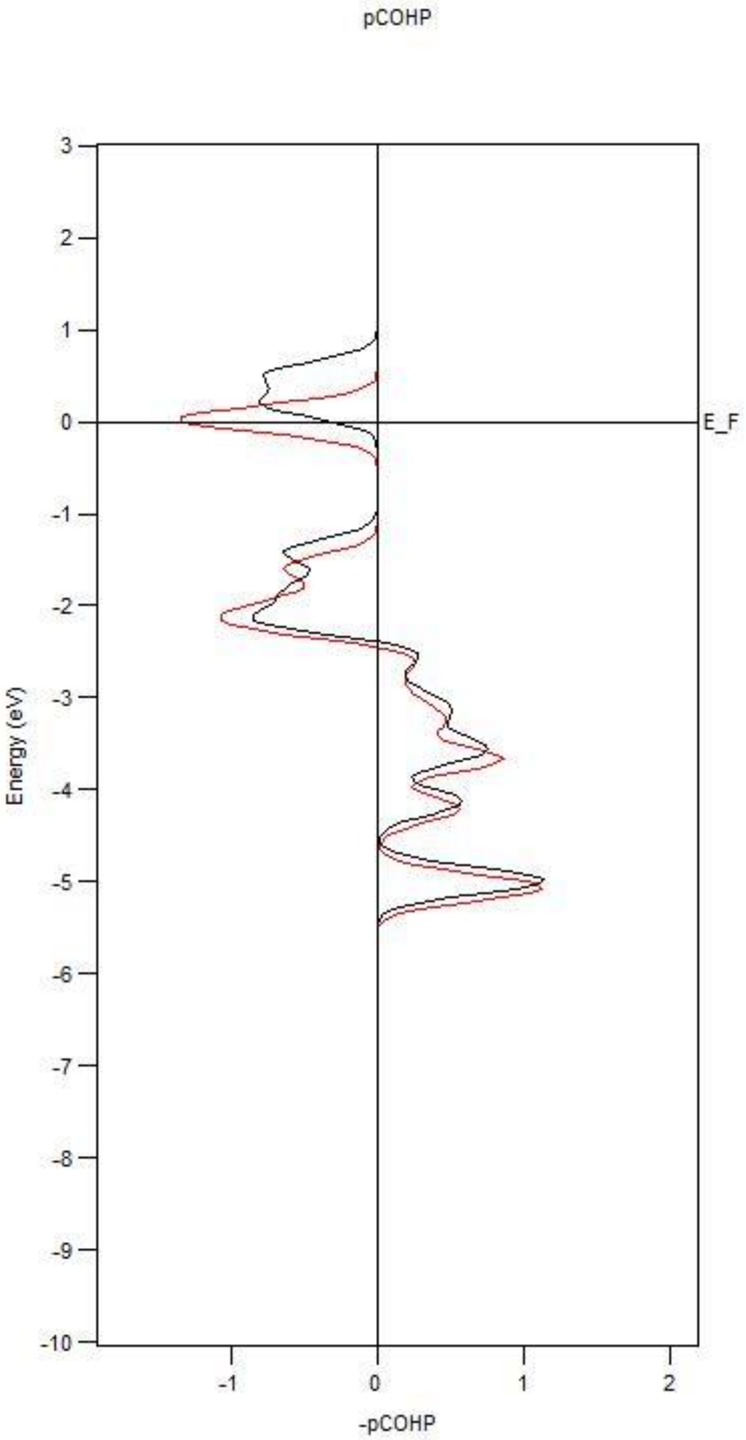

Figure S 13: Average pCOHP (Au-Au) of Au_3*; spin 1 (red) and spin 2 (black).*

5.2.2 Au_6

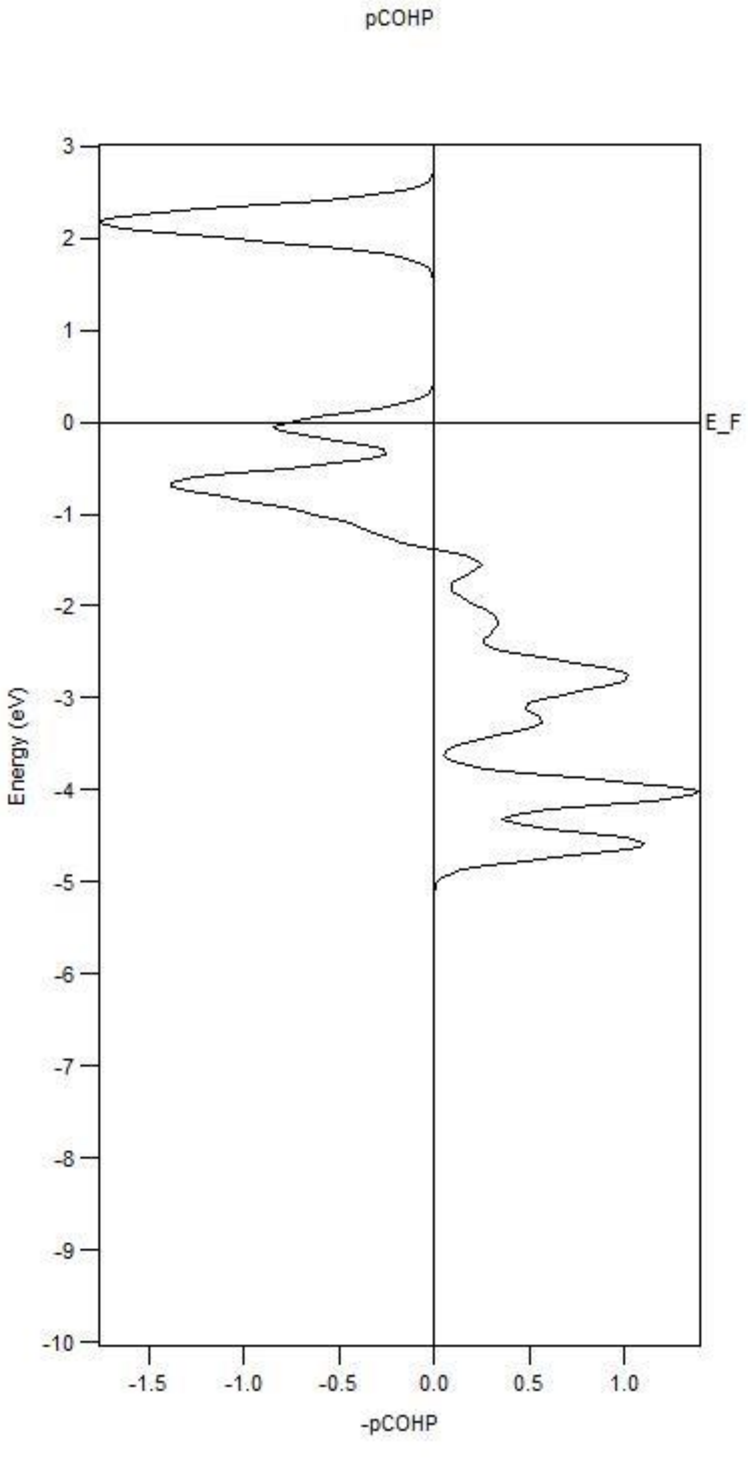

Figure S 14: Average pCOHP (Au-Au) of Au_6*.*

5.3 Supported Clusters

5.3.1 Au_3/MgO

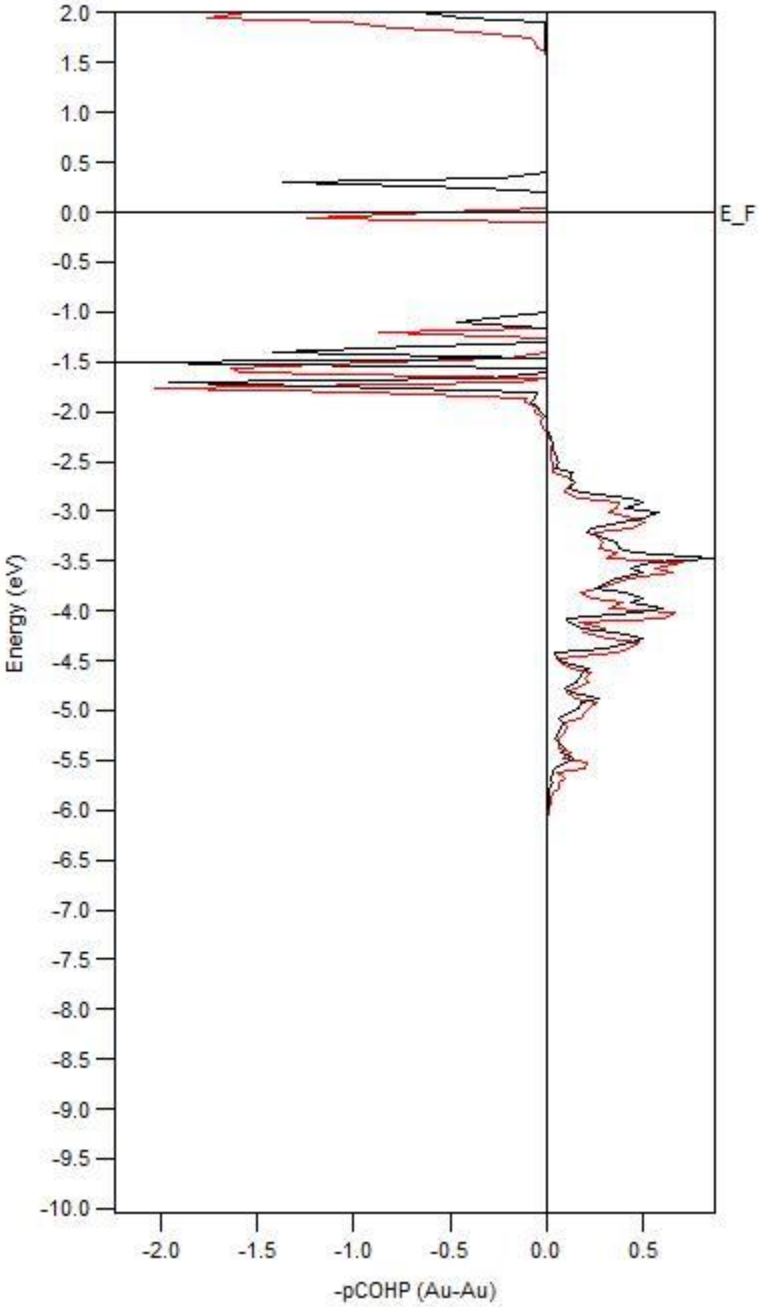

Figure S 15: Average pCOHP of Au-Au pairs within 4.0 Å of Au_3/MgO; spin 1 (red) and spin 2 (black).

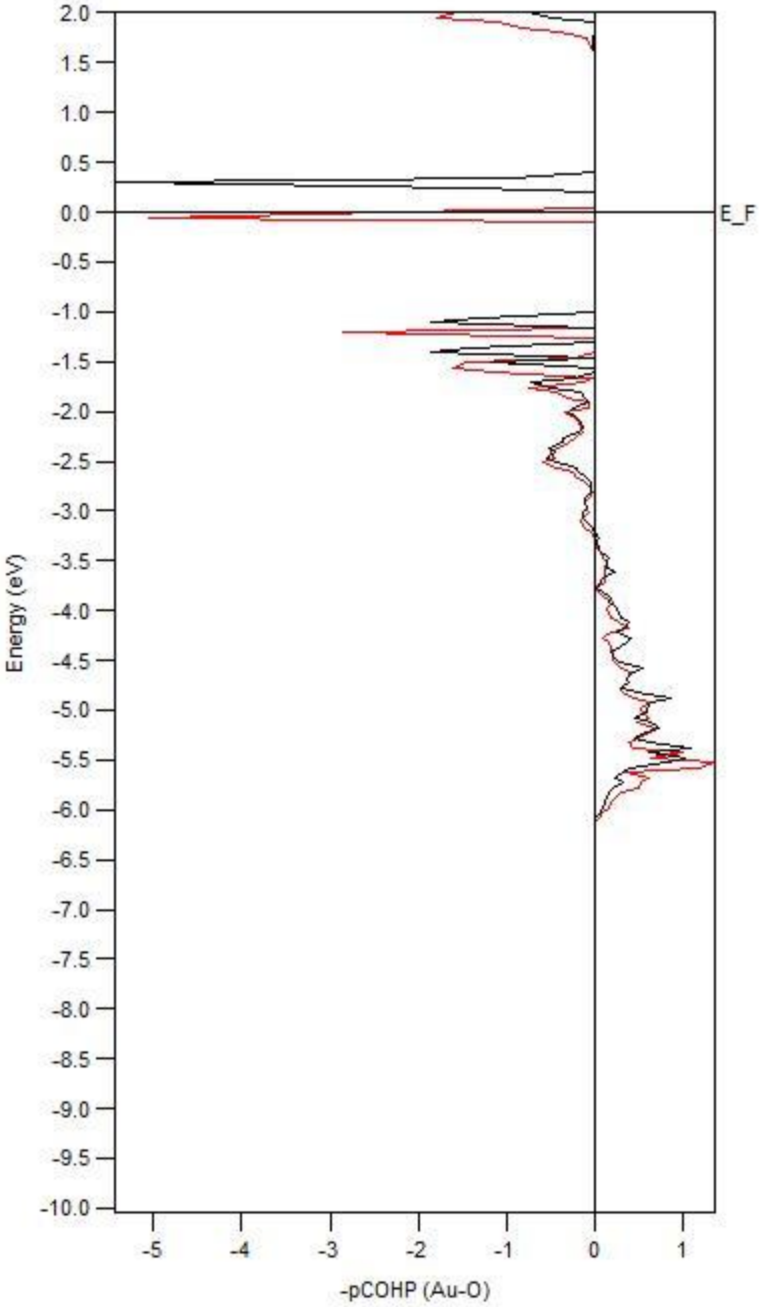

Figure S 16: Average pCOHP of Au-O pairs within 4.0 Å of Au_3/MgO; spin 1 (red) and spin 2 (black).

5.3.2 Au$_6$/MgO

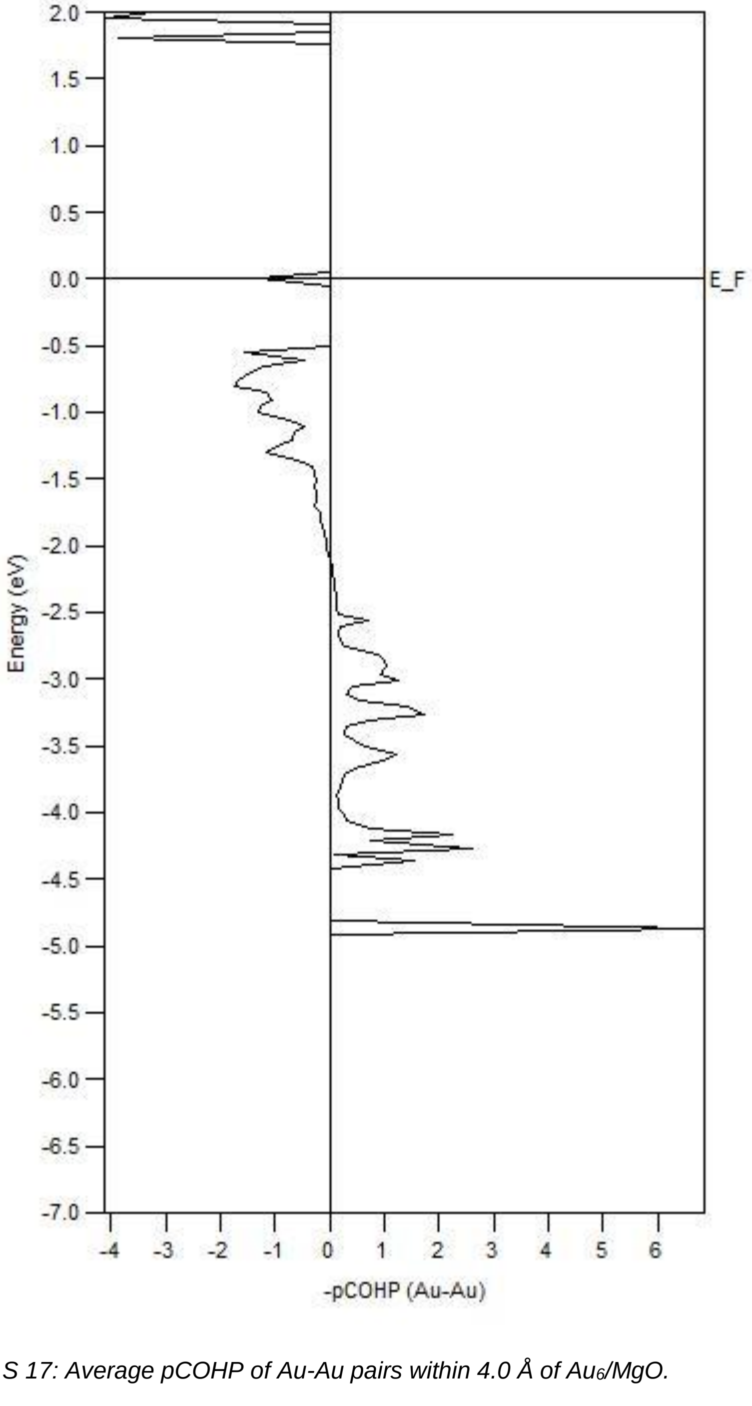

Figure S 17: Average pCOHP of Au-Au pairs within 4.0 Å of Au$_6$/MgO.

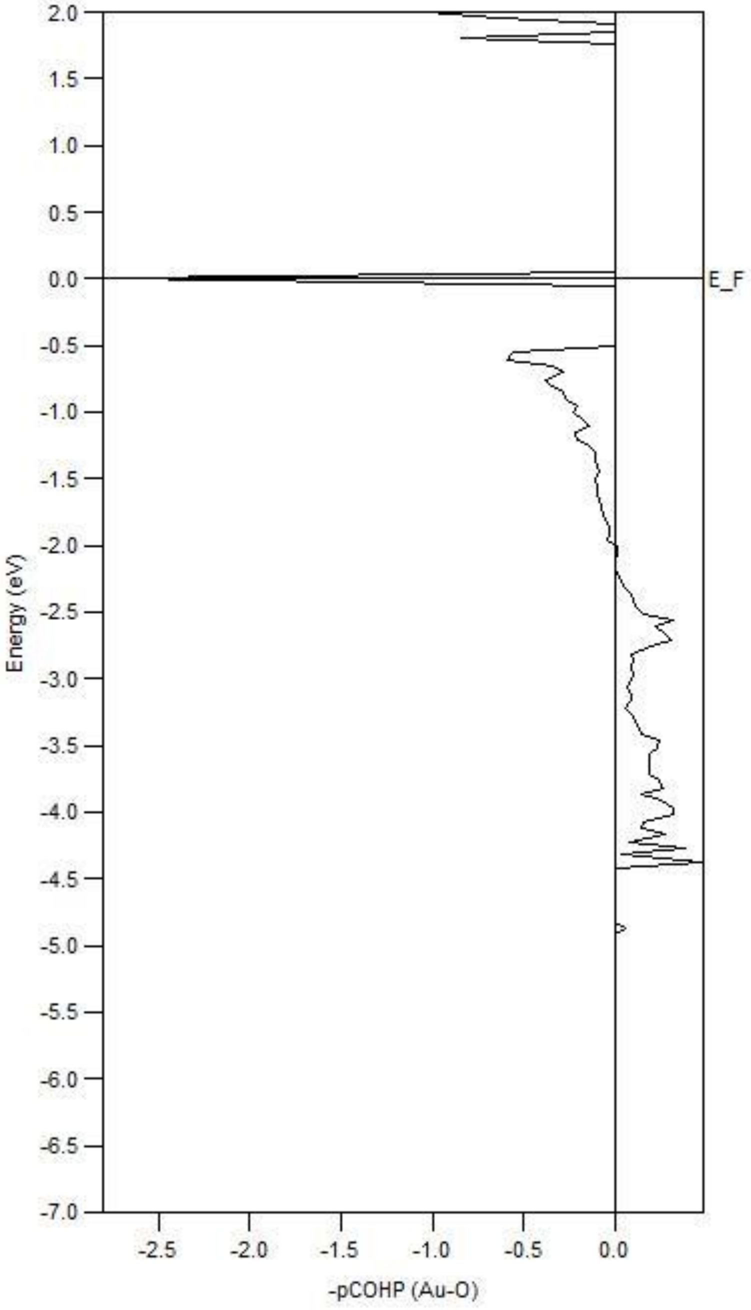

Figure S 18: Average pCOHP of Au-O pairs within 4.0 Å of Au_6/MgO.

5.3.3 Au_3/C

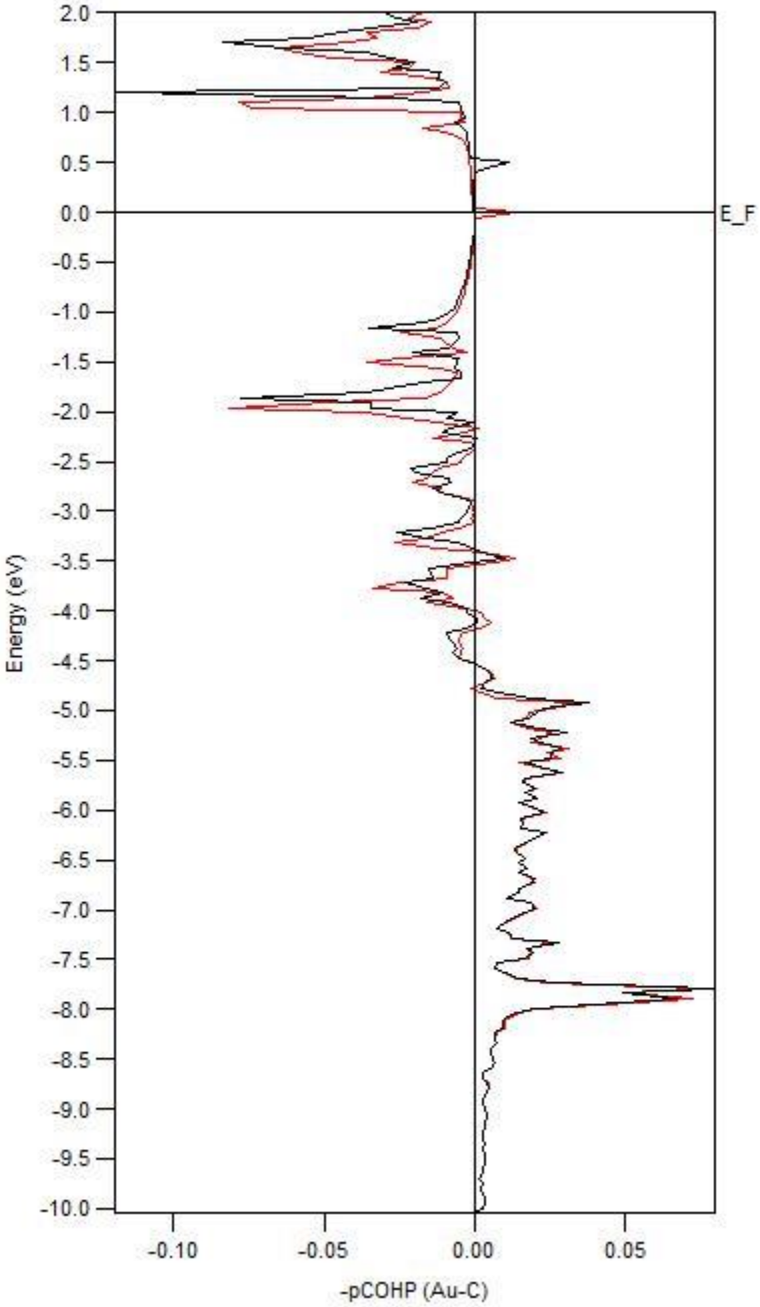

Figure S 19: Average pCOHP of Au-C pairs within 4.0 Å of Au_3/C; spin 1 (red) and spin 2 (black).

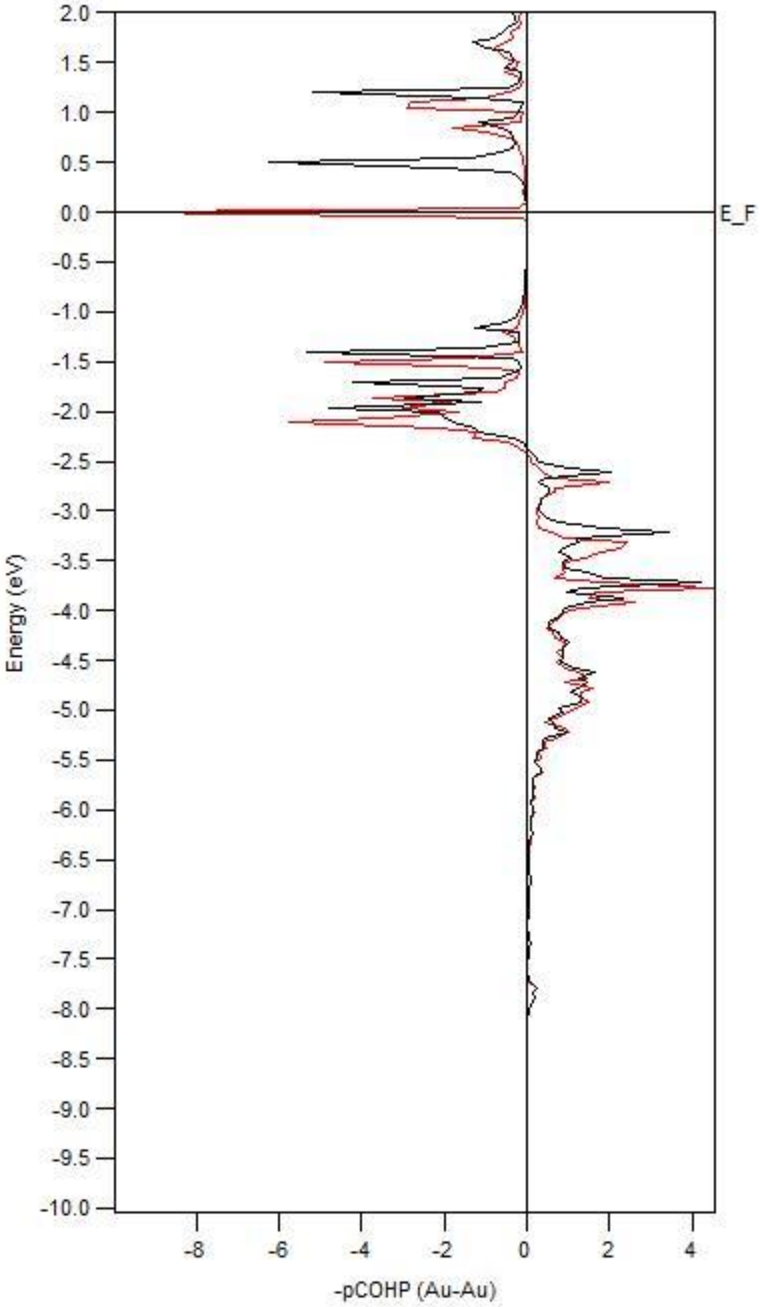

Figure S 20: pCOHP of Au-Au pairs within 4.0 Å of Au_3/C; spin 1 (red) and spin 2 (black).

5.3.4 Au_6/C

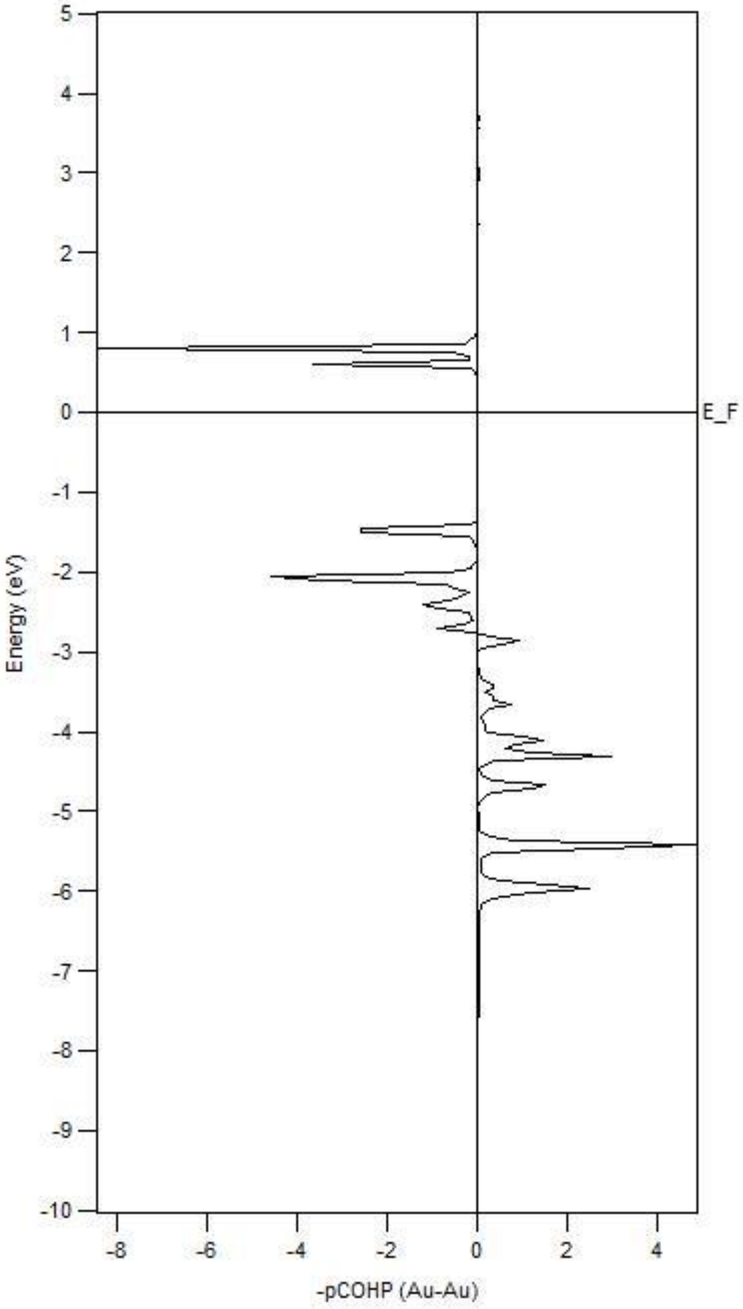

Figure S 21: Average pCOHP of Au-Au pairs within 4.0 Å of Au_6*/C.*

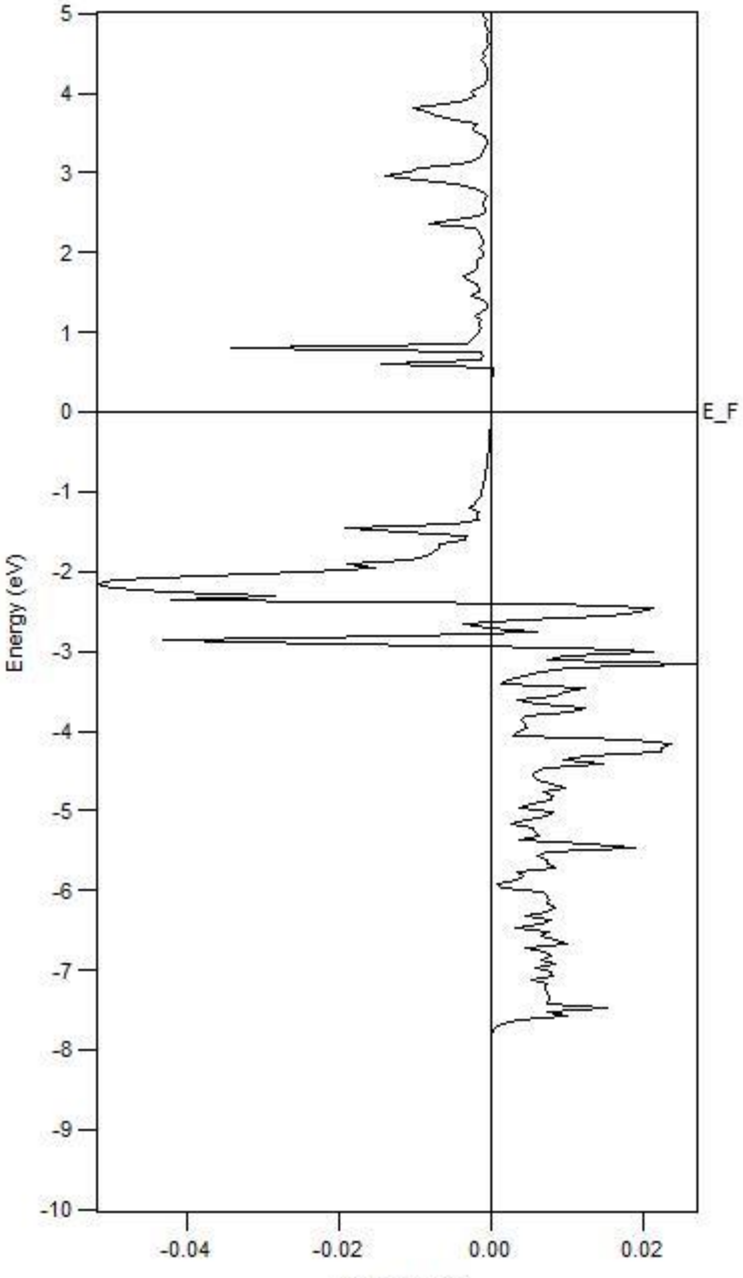

Figure S 22: Average pCOHP of Au-C pairs within 4.0 Å of Au_6/C.

5.3.5 Au_3/CeO_2

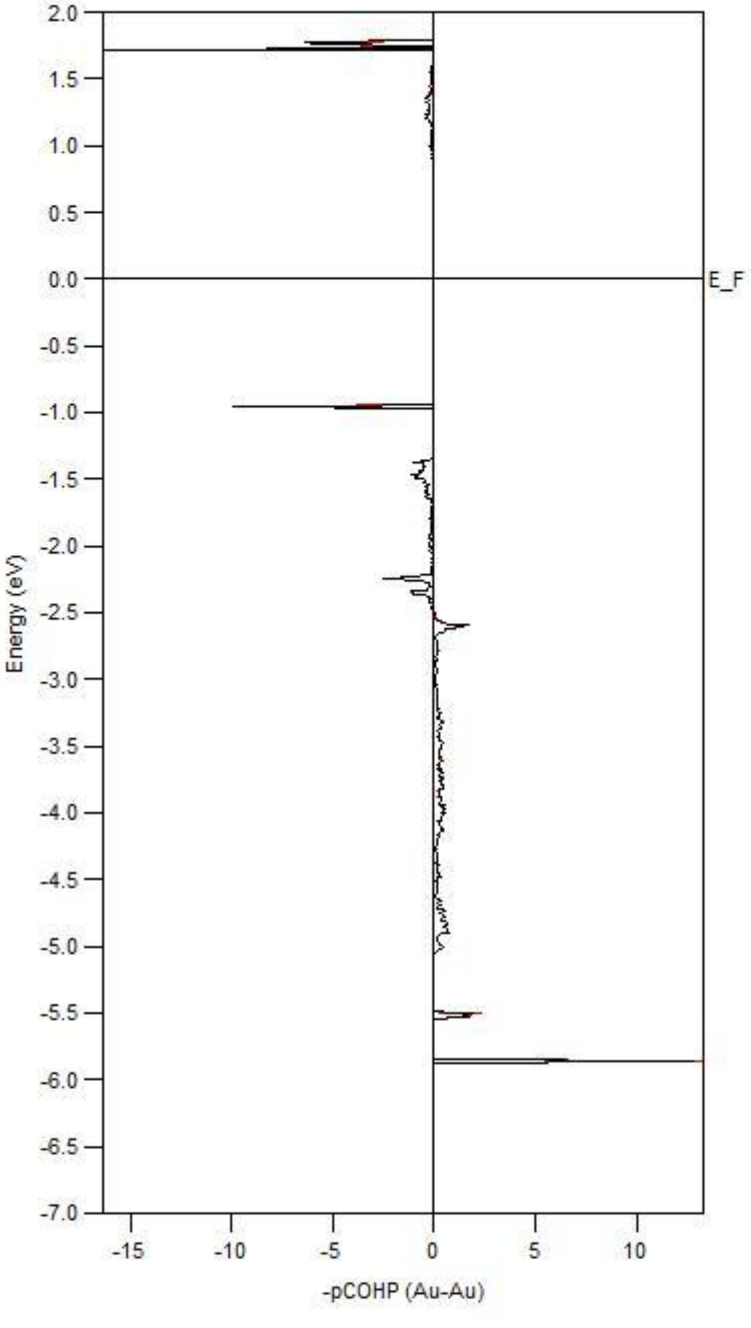

Figure S 23: Average pCOHP of Au-Au pairs of Au_3/CeO_2 within 3.5 Å; spin 1 (red) and spin 2 (black).

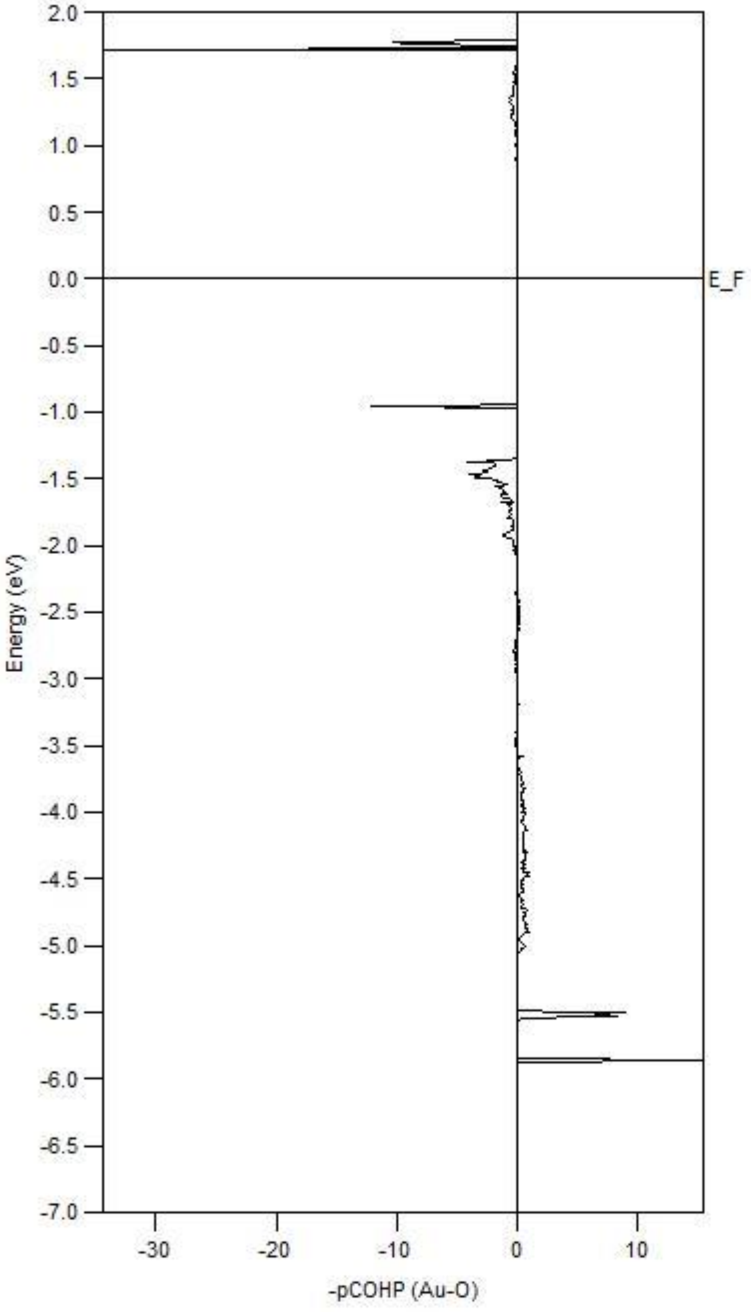

Figure S 24: Average pCOHP of Au-Au pairs within 3.5 Å; spin 1 (red) and spin 2 (black).

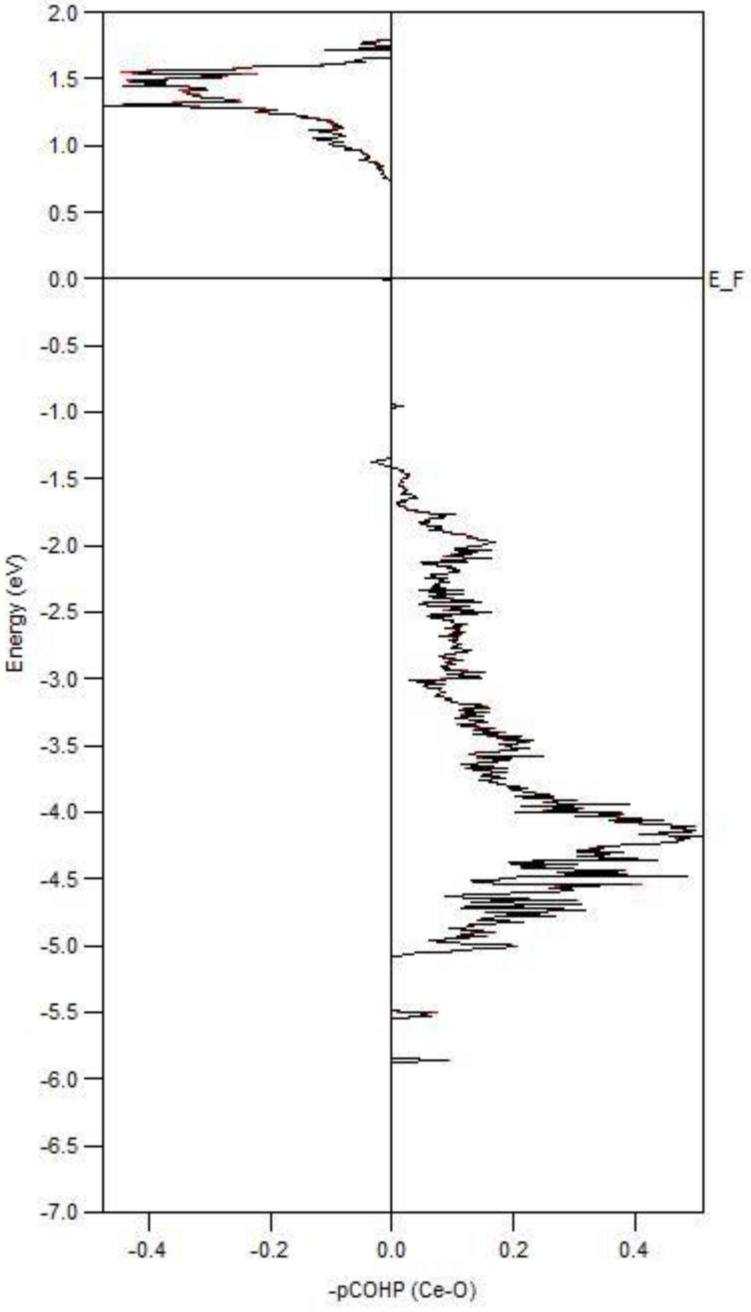

Figure S 25: Average pCOHP of Ce-O pairs within 3.5 Å; spin 1 (red) and spin 2 (black).

5.3.6 Au$_6$/CeO$_2$

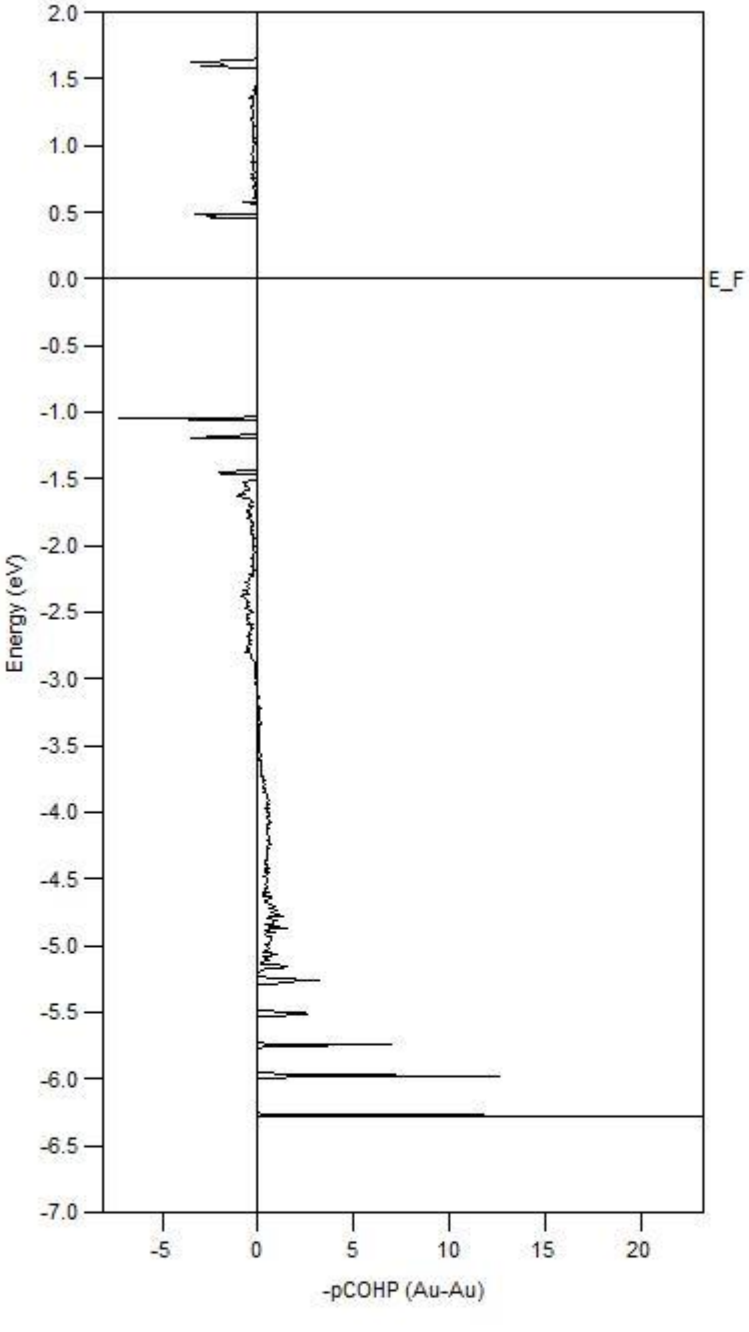

Figure S 26: Average pCOHP of Au-Au pairs within 3.5 Å.

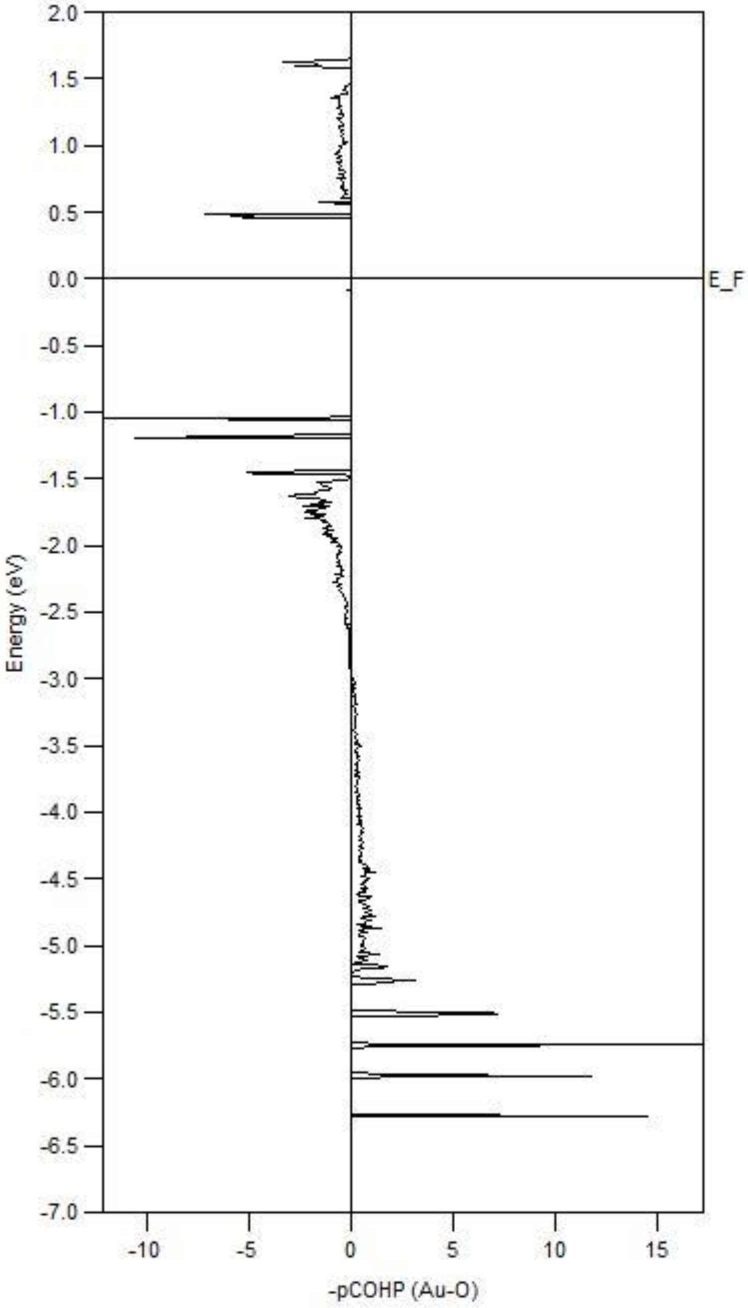

Figure S 27: Average pCOHP of Au-O pairs within 3.5 Å.

6. DFT+U benchmark

6.1 Computational Details

The general method is described in the Computational Details section of the main article. Benchmark calculations were performed with a Monkhorst-Pack 13x13x13 grid. The energy of O_2 was corrected to compensate overbinding based on an experimental binding energy of −5.17 eV.[36]

6.2 Benchmark of the Hubbard parameters

The influence of the Hubbard parameter on the lattice parameter, bulk modulus, and band gap of bulk CeO_2 as well as on the formation energies of CeO_2 and Ce_2O_3 and the energy of the reaction of CeO_2 to Ce_2O_3 was investigated. The results show that our choice of parameters (U = 5 eV; J = 1 eV) reproduces best the experimental values of the formation energy of CeO_2 (Figure S31) and the transformation of CeO_2 to Ce_2O_3 (Figure S33). The latter involves the reduction of Ce^{4+} to Ce^{3+} which is of particular importance in our work. Moreover, none of the investigated parameter values give good agreement with experimental values of the CeO_2 lattice parameter (Figure S28), bulk modulus, or 3d-4f band gap.

Lattice parameter

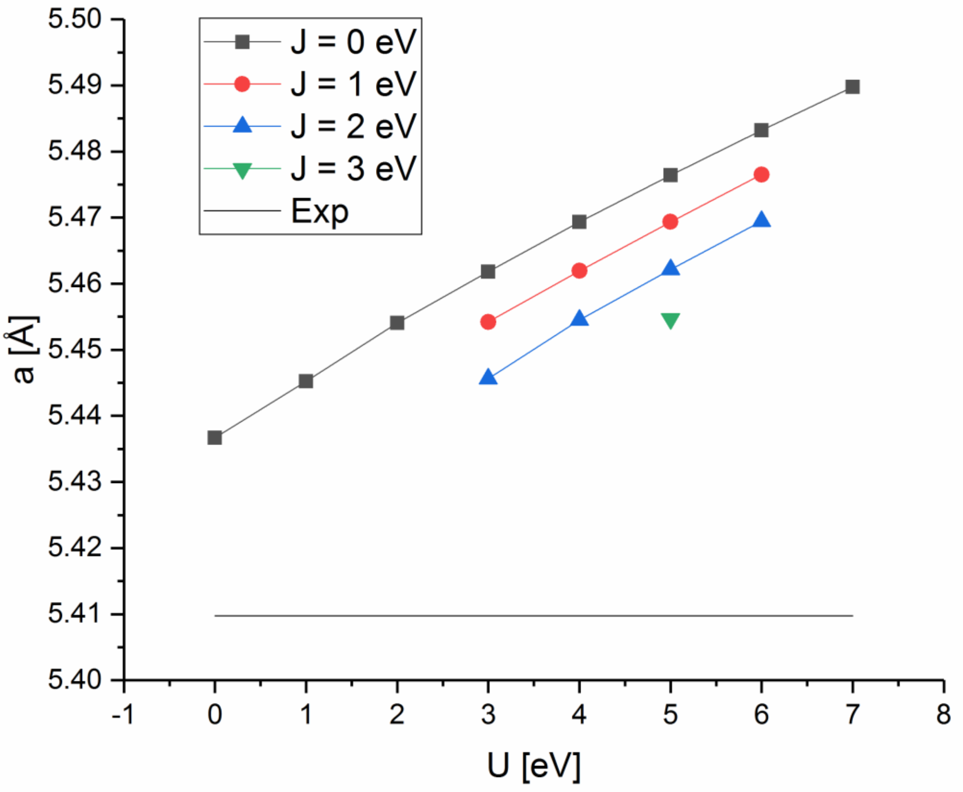

Figure S 28: Benchmark of the Hubbard parameters with respect to the CeO_2 lattice parameter a; experimental value from Artini et al.[37]

Bulk modulus

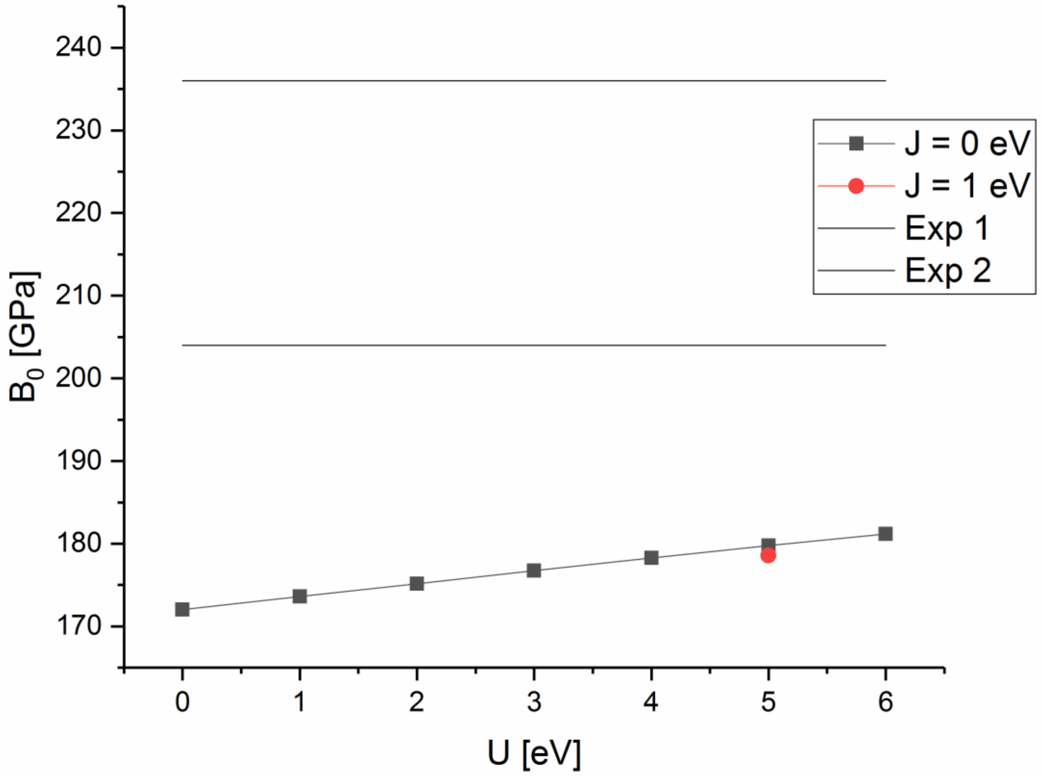

Figure S 29: Benchmark of Hubbard parameters with respect to the bulk modulus B_0 of CeO_2; experimental value from Loschen et al.[38]

Band gap

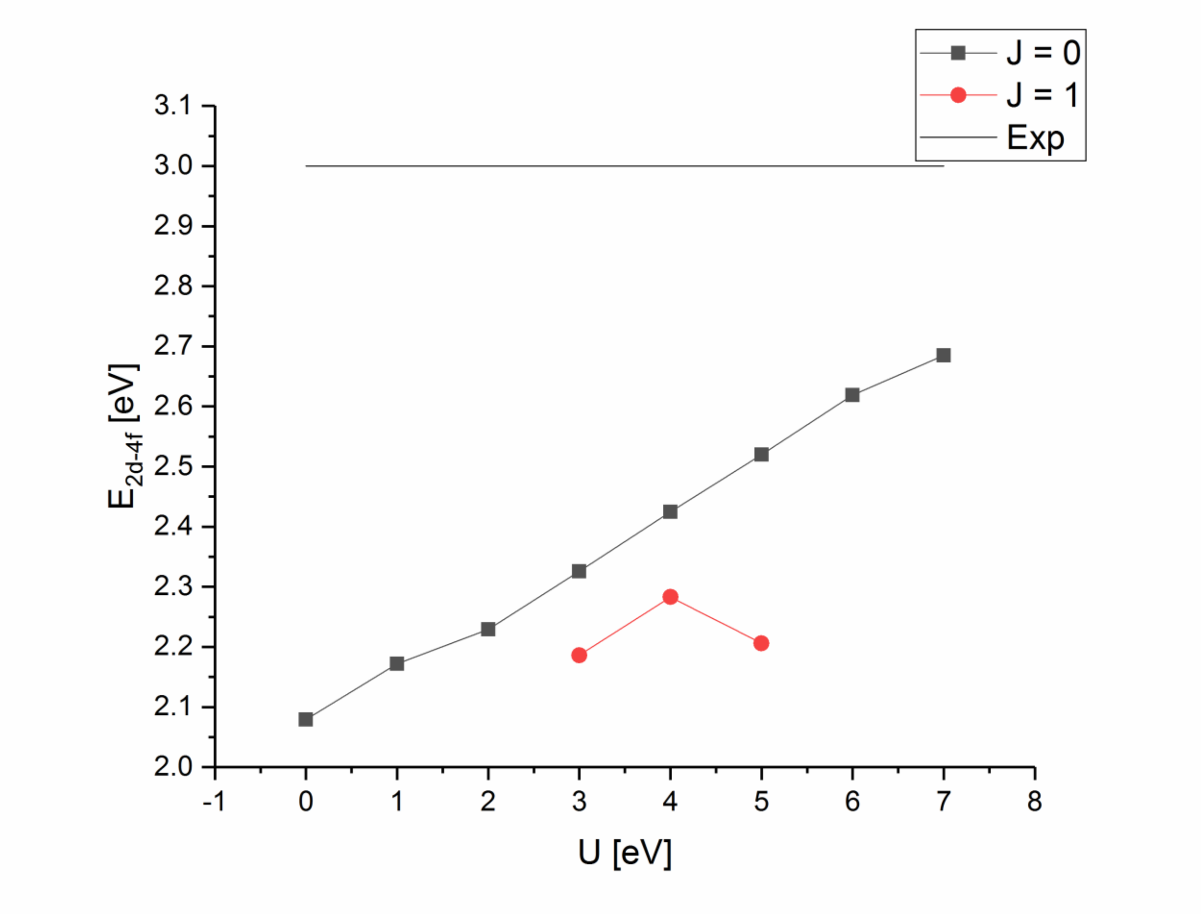

Figure S 30: Benchmark of Hubbard parameters with respect to the band gap (2d-4f) of CeO_2; experimental value from Loschen et al.[38]

CeO_2 formation energy

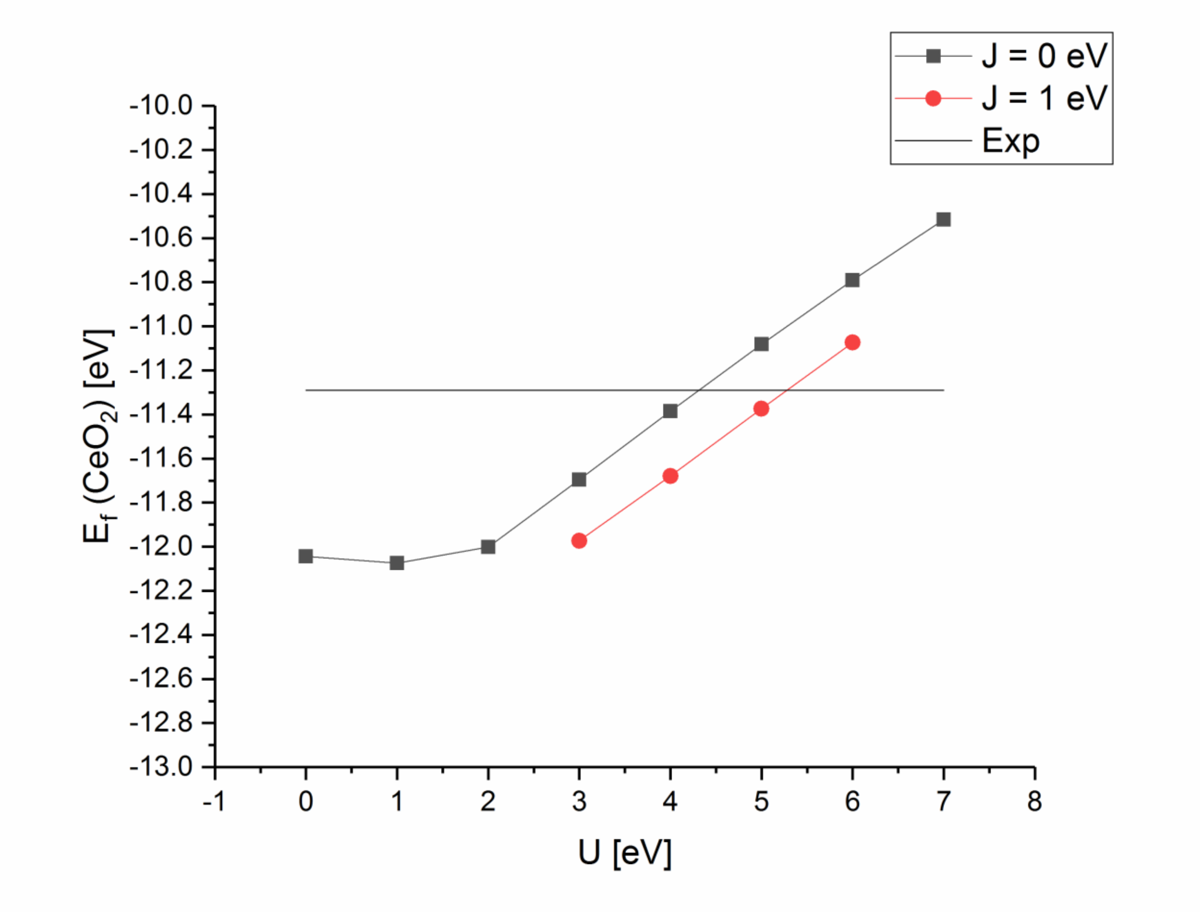

Figure S 31: Benchmark of Hubbard parameters with respect to formation energy of CeO_2; experimental value from Loschen et al.[38]

Ce_2O_3 formation energy

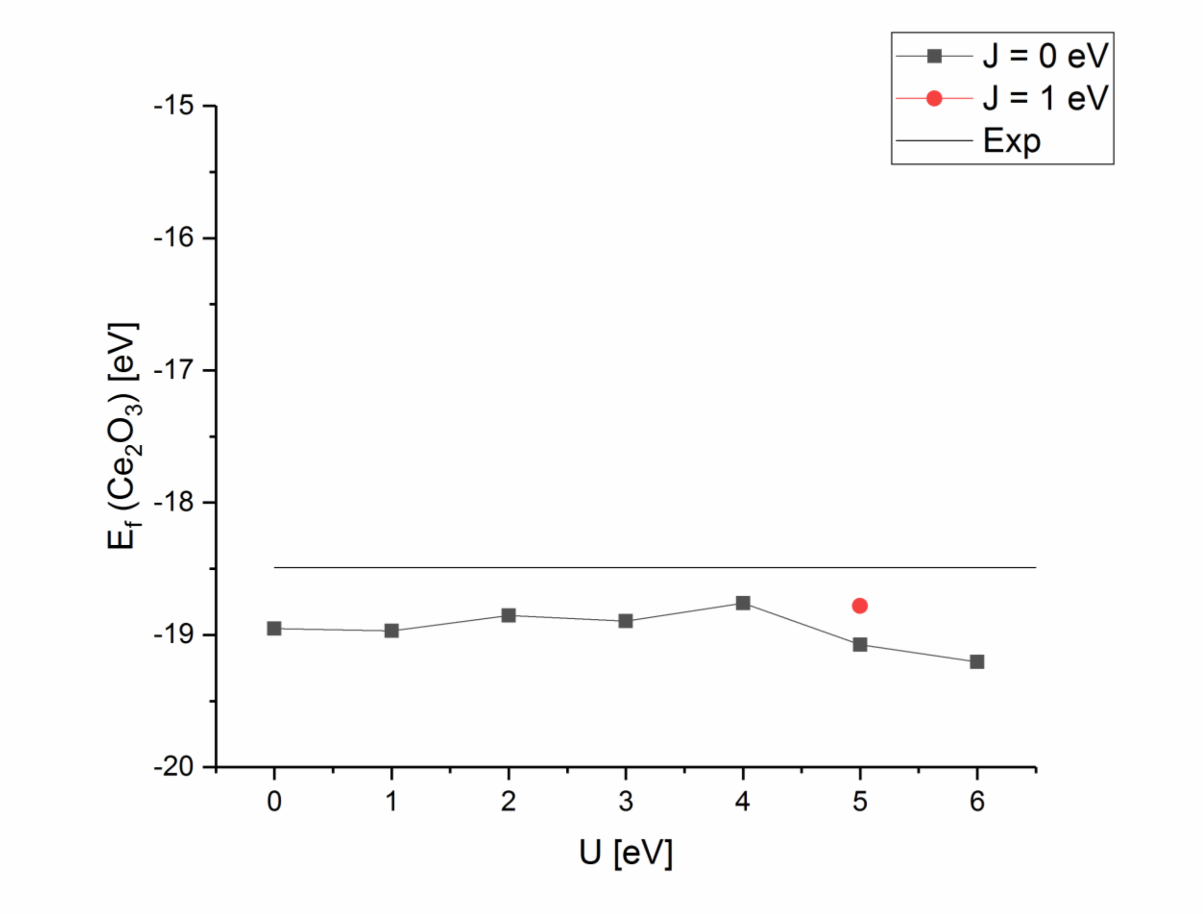

Figure S 32: Benchmark of Hubbard parameters with respect to formation energy of Ce_2O_3; experimental value from Loschen et al.[38]

CeO_2 to Ce_2O_3 reaction energy

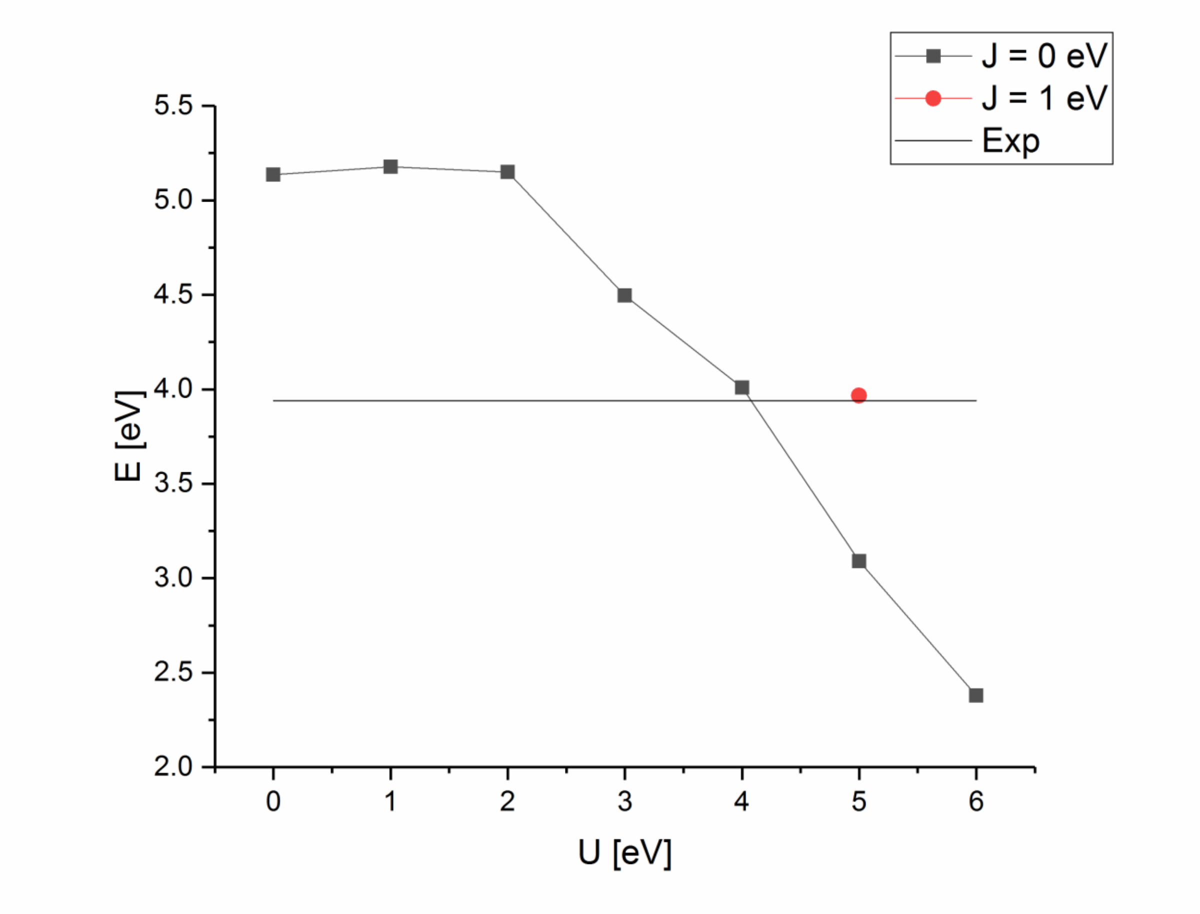

Figure S 33: Benchmark of the Hubbard parameters with respect to the transformation of CeO_2 to Ce_2O_3 and O_2; experimental value from Loschen et al.[38]

6.3 Influence of Hubbard parameters on Au_1/CeO_2

Adsorption energy

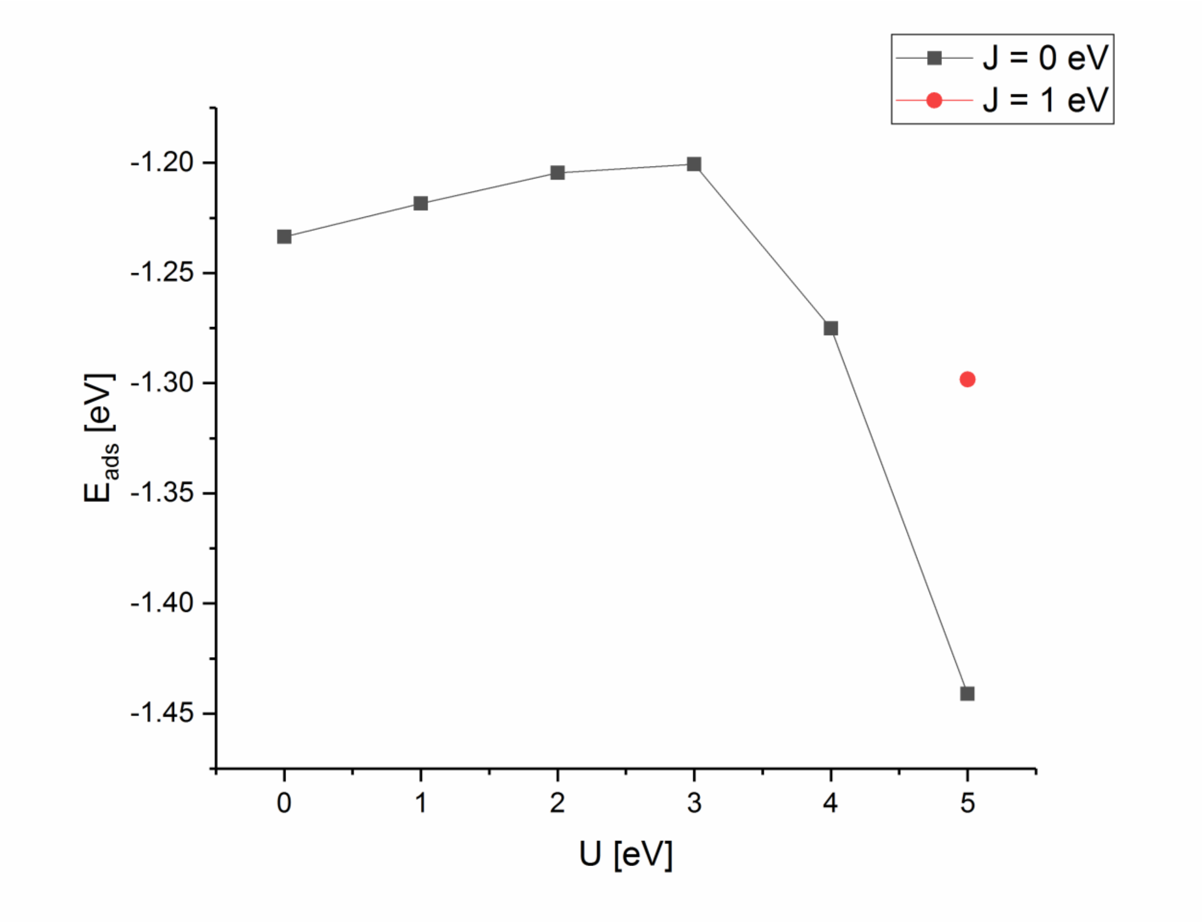

Figure S 34: Influence of the Hubbard parameters on the adsorption energy of Au_1 on $CeO_2(111)$.

Charge transfer

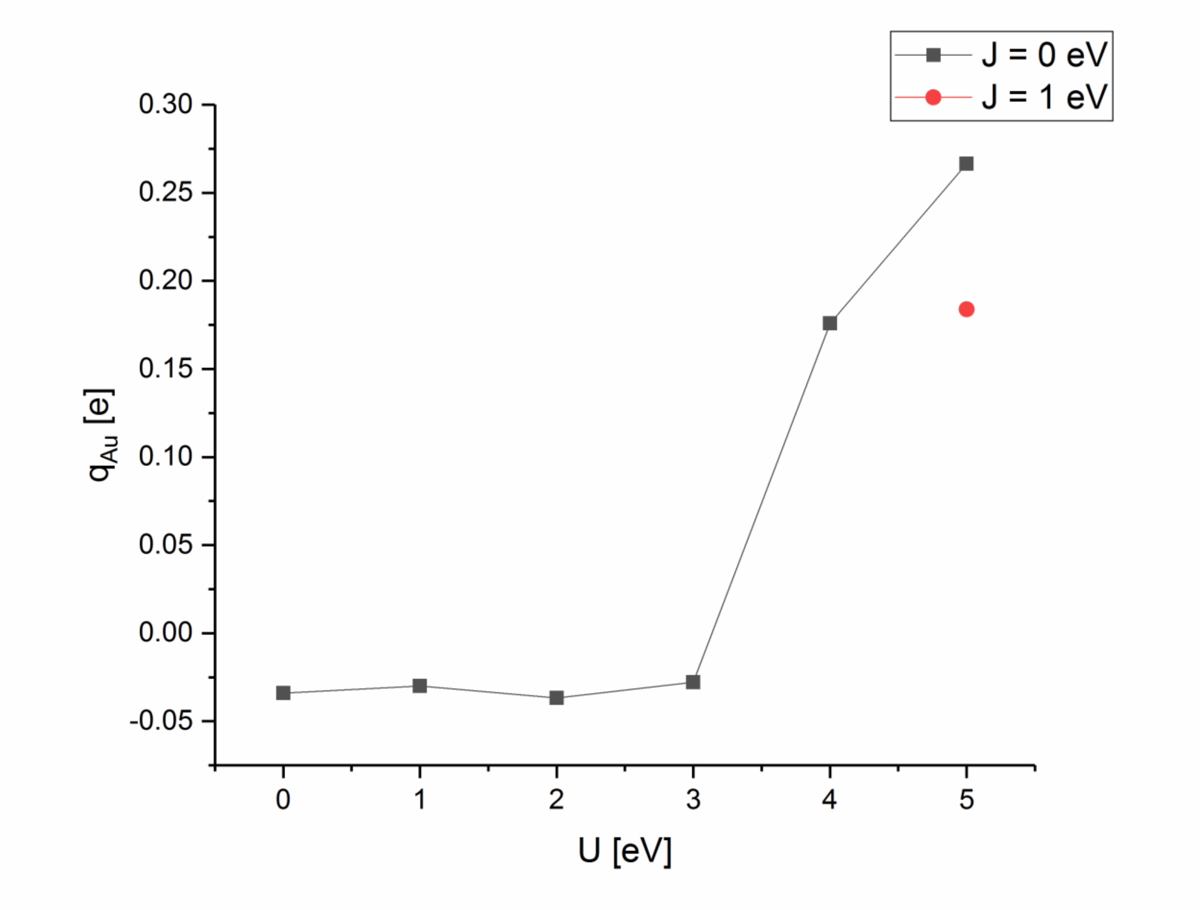

Figure S 35: Influence of the Hubbard parameters on the charge transfer between Au$_1$ *and the CeO*$_2$*(111) surface.*

Au-O distance

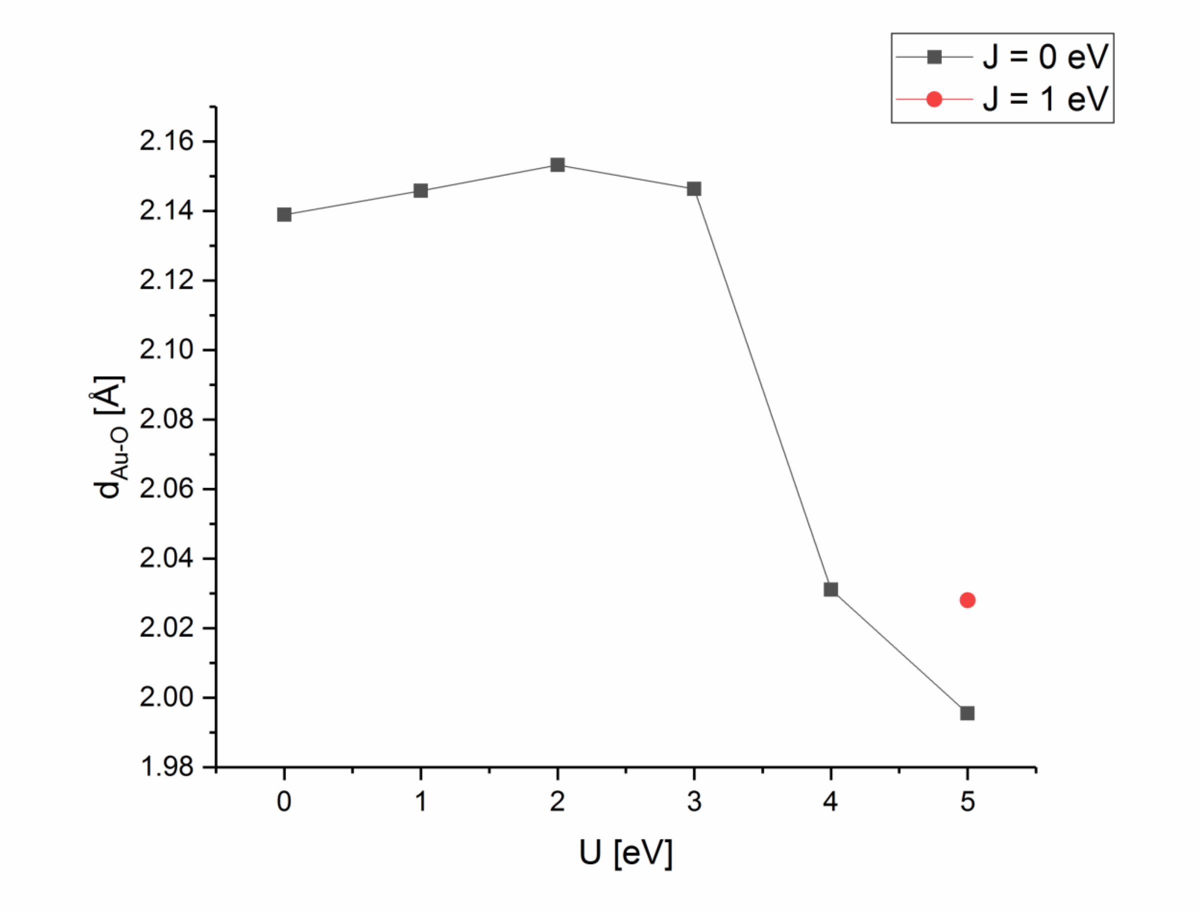

Figure S 36: Influence of the Hubbard parameters on distance between Au_1 and the CeO_2(111) surface.

7. Mismatch calculations

For a consistently good fit of the cluster interface on the surface, the ideal adsorption positions must occur in the same distance and with the same symmetry as the interface of the cluster. In this model, we assume that only one type of adsorption sites exists, and these sites are periodically distributed on the surface with the translation vectors k and l. There are many cases with more than one adsorption site is present on the surface. The inclusion of additional adsorption sites is not problematic in general. However, it is not possible to distinguish between different types of adsorption sites without including information about the energetics to penalise for the adsorption on less favoured sites. As this model is meant to be based on structural information only, we decided to exclude non-identical sites.

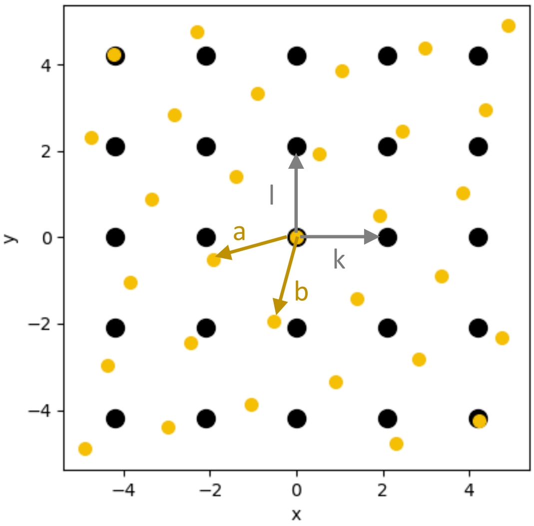

Figure S 37: Schematic representation of the surface (black) and cluster (yellow) grids.

Like the surface sites, the cluster atoms are represented by a grid, constructed with the lattice vectors of the cluster a and b. We define that the first atom of the cluster is locate located directly on top of an adsorption site. This position is set as the origin of the coordinate system. Any vector to another cluster atom p can then be constructed as a linear combination of the surface vectors:

$$R(\alpha)\,\vec{p} = c_1 \cdot \vec{k} + c_2 \cdot \vec{l}$$

The two-dimensional rotation matrix R(α) describes the rotation of the cluster with angle α with respect to the surface since their relative orientation is unknown. The rotated cluster atom p is named p’.

$$R(\alpha) = \begin{pmatrix} \cos\alpha & -\sin\alpha \\ \sin\alpha & \cos\alpha \end{pmatrix}$$

$$\vec{p}' = R(\alpha)\,\vec{p}$$

If every atom of the cluster is located on one of the sites described by k and l, then a rotation angle α exists for which the coefficients c_i are integer.

$$c_i \in \mathbb{Z}$$

For any non-zero mismatch case, the coefficients can take any rational value. Rounding of c_i to the closest integer value gives the coefficients c_i^R to the closest surface site q.

$$c_i^R = \lfloor c_i + 0.5 \rfloor$$

$$\vec{q} = c_1^R \cdot \vec{k} + c_2^R \cdot \vec{l}$$

The local mismatch m_p at the atom p can therefore be defined as the distance between the rotated cluster atom p' and the surface site q. The value is divided by the average length of the cell vectors to obtain a size consistent result. This means that the same value is obtained if the size of all vectors is scaled by the same factor.

$$m_p = \frac{4 \cdot |\vec{p}' - \vec{q}|}{|\vec{a}| + |\vec{b}| + |\vec{k}| + |\vec{l}|}$$

Since this expression describes the mismatch at each point, one could be tempted to define the mismatch as the average m_p over the cluster. However, this definition would be fundamentally flawed as for any non-zero mismatch case at infinite system size, the cluster atoms become equally distributed over all positions of the surface unit cell, which means, that the value obtained is only dependent on the surface vectors and independent from the structure of the cluster interface. Restriction to a fixed number of points or points within a certain radius around the origin can lead to artefacts and inconsistencies between different shapes and sizes. However, the initial change of the average mismatch d with increasing radius r describes the structural strain, which would build up during epitaxial growth of the cluster on the surface.

$$m_N(r) = \sum^{r} m_p(r_i) \cdot n(r)^{-1}$$

$$d = \frac{\partial m_N(r)}{\partial r}$$

High strain leads to mismatch induced three-dimensional cluster growth and eventually less wetting of the cluster surface. Moreover, if other facets of the cluster show less mismatch but higher surface energy, a change of the structure at the interface to the surface becomes likely at larger cluster size.

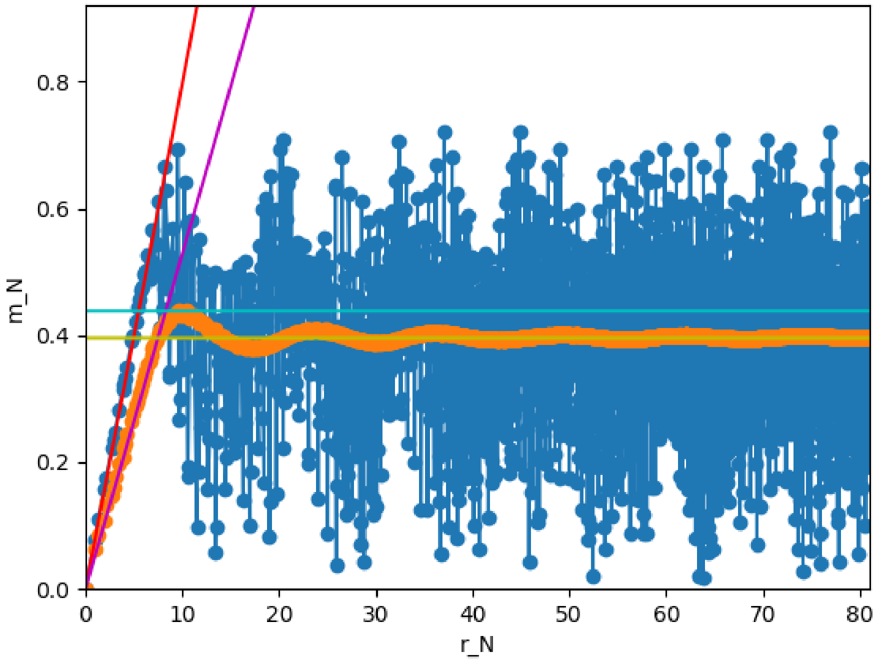

Figure S 38: Mismatch plot of Au(001)/MgO(001) based on DFT surface calculations; dark blue line: average mismatch at r; orange line: average mismatch at all positions within r; red line: initial slope of the average mismatch at r; purple line: initial slope of the average mismatch at all positions within r; light blue line: maximum average mismatch at all positions within r.

Second set of identical sites

The presented model assumes that all adsorption sites can be obtained by integer translation with $\vec{k}$ and $\vec{l}$ from the first site. However, in some materials (e.g. graphene) there may be sets of identical sites which are shifted to each other by another vector $\vec{s}$. All points of each set can be constructed by translations with $\vec{k}$ and $\vec{l}$ from any point of the given set but no point of the other set.

$$R(\alpha)\,\vec{p} = c_{1s} \cdot \vec{k} + c_{2s} \cdot \vec{l} + \vec{s}$$

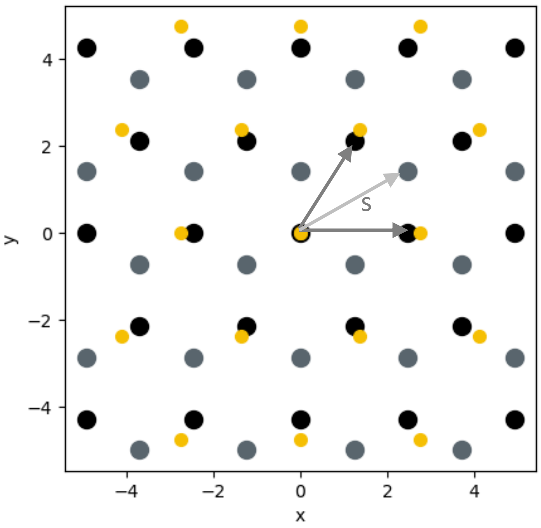

Figure S 39: Schematic representation of the surface (set 1: black; set 2: grey) and cluster (yellow) grids.

The local mismatch with respect to the second set can be calculated with

$$\vec{q}_s = c_{1s}^R \cdot \vec{k} + c_{2s}^R \cdot \vec{l}$$

$$m_{p,s} = |\vec{p}' - \vec{q}_s|$$

No redefinition of $\vec{k}$ and $\vec{l}$ is possible to include all sites in a single set. Since the sites of these sets are identical, the described equations only consider a fraction of the available adsorption positions. While these positions can be significant in high mismatch cases for the binding of small clusters to the surface, their importance diminishes quickly as the cluster grows because the shifting vector $\vec{s}$ is not represented in the structure of the clusters.

Cluster rotation

The rotation angle alpha between the surface and the cluster is determined by minimisation of the sum of all $m_{p,i}$ within $r < 2 \cdot |\vec{a}|$.

Determination of d_{ini} – Linear fit

Herein, we use a linear fit on the values of $m_N(r)$ through the origin including as many points as possible while maintaining a minimum R^2 value of the fit. In most cases, the slope of the linear fit is equal to $m_N(r)$ of the first neighbour shell. However, small deviations between the angles of the surface and cluster lattices result in small oscillations of $m_N(r)$ around the general linear behaviour. The linear fit cancels these oscillations out if they are below the set threshold. In this work, we used a minimum R^2 of 0.98. It can be adjusted in the input file (*mismatch.in*)

Mismatch at very large radius ($m_N(\infty)$)

The value of m_N at large radius before normalisation is independent from the cluster material and only dependent on the shape of the support material. The value can be determined analytically by integrating the distance function over the unit cell of the support. As an example, we show the solution for |a|, |b|, |k|, |l| = 1.0; θ = 90°, ρ = 60° (normalisation factor = 1) here:

For θ = 90°, the unit cell is square and the points within each quadrant of the square are closest to one of the corners. Hence, the average distance can be calculated from a single quadrant.

$$m_N(\infty) = 4 \cdot \int_0^{0.5} \int_0^{0.5} \sqrt{a^2 + b^2}\, da\, db = 0.3826$$

Using our script, we determined a final value of 0.382597 after 10000 neighbour sets.

Python script

Input file

The mismatch.in file contains all input information. All keywords are case-sensitive. All parameters, which are given here with one decimal need at least one decimal to be recognised by the script as valid input.

```
##CLUSTER DEFINITION##
LENGTH_A = 1.7 ##Defines the length of a (cluster)
LENGTH_B = 1.7 ##Defines the length of b (cluster)
ANGLE_PHI = 60.0 ##Defines the angle phi (cluster)
##SURFACE DEFINITION##
LENGTH_K = 2.05 ##Defines the length of k (surface)
LENGTH_L = 2.05 ##Defines the length of l (surface)
ANGLE_THETA = 60.0 ##Defines the angle theta (surface)
N_SET2_IF = 0 ##0: only one set of identical sites; 1: second set
N_SET2_L = 1.3 ##distance of SET2 to SET1
N_SET2_ANGLE = 30.0 ##angle of the shift from SET1 to SET2
##SETTINGS##
N_NEIGHBOURS = 200 ##Defines the number of calculated neighbour shells
R_CUT = 0.98 ##Minimum R^2 for linear fit
PLOT_FUNC = 1 ##1: Show plot of linear fit
PLOT_CLUSTER = 1 ##1: Show cluster plot
ALPHA_MIN = 1 ##0: no minimisation; 1: Nelder-Mead algorithm
ALPHA_RAND = 2 ##1: starting value of alpha randomly set; 2: theta-phi/2
ANGLE_ALPHA = 15.0 ##Defines starting value of alpha (if alpha rand is zero)
D_NORM = 3 ##0: r_N and m_N not normalised; 1: normalisation to (a+b)/2; 2: normalisation to (k+l)/2; 3: normalisation to (a+b+k+l)/4
```

Output files

Cluster.png: Schematic plot of the surface and cluster grid

Plot.png: Plot of the mismatch; compare Figure S38 for details

Mismatch.out: Contains all information and results of the run

Mismatch_plot: Average mp at r and linear fit data

Mismatch_plot_add: Average mN at r and linear fit data

Workflow

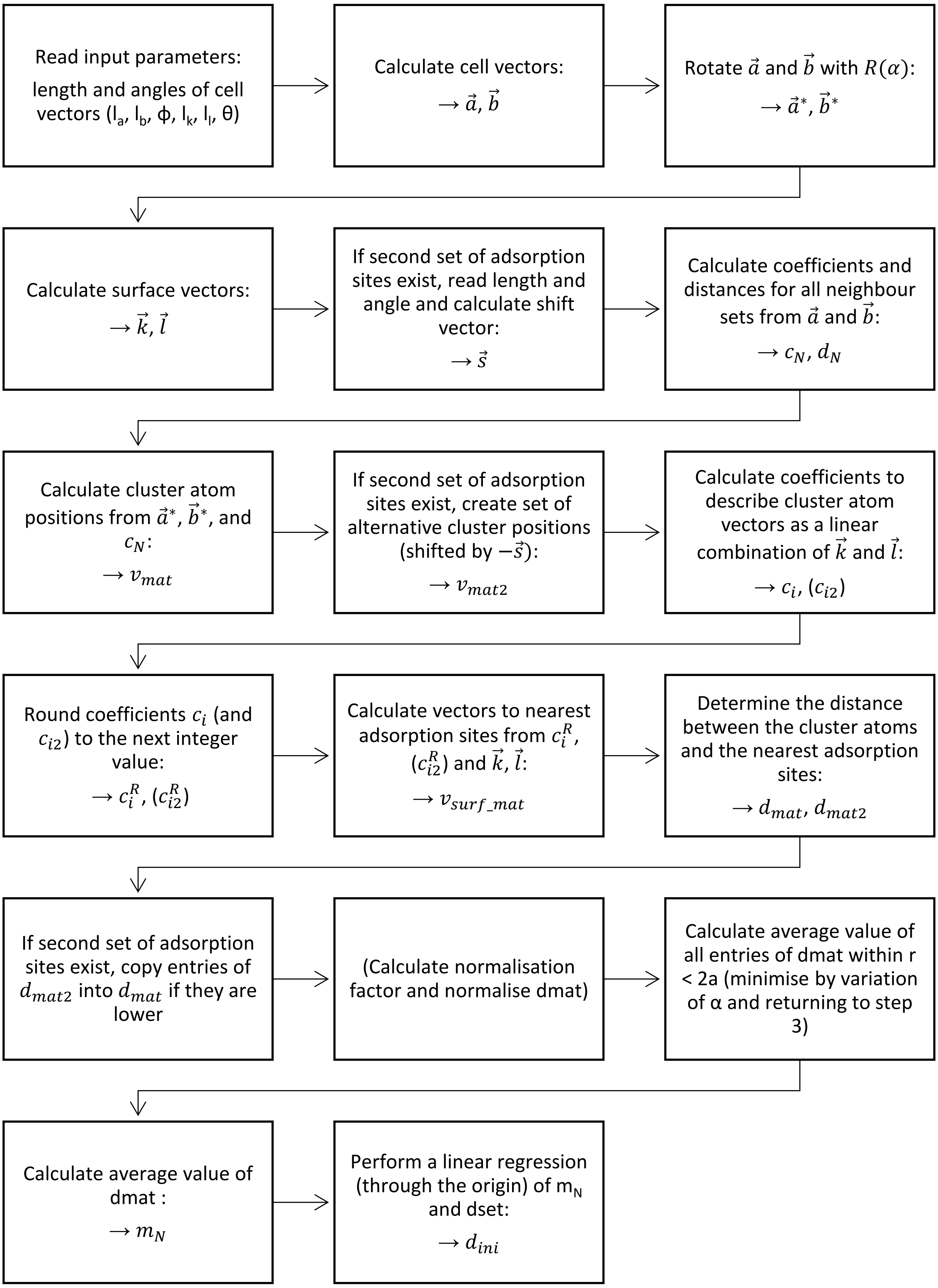
Read input parameters: length and angles of cell vectors (l_a, l_b, ϕ, l_k, l_l, θ)
Calculate cell vectors: $\rightarrow \vec{a}, \vec{b}$
Rotate $\vec{a}$ and $\vec{b}$ with $R(\alpha)$: $\rightarrow \vec{a}^*, \vec{b}^*$
Calculate surface vectors: $\rightarrow \vec{k}, \vec{l}$
If second set of adsorption sites exist, read length and angle and calculate shift vector: $\rightarrow \vec{s}$
Calculate coefficients and distances for all neighbour sets from $\vec{a}$ and $\vec{b}$: $\rightarrow c_N, d_N$
Calculate cluster atom positions from $\vec{a}^*$, $\vec{b}^*$, and c_N: $\rightarrow v_{mat}$
If second set of adsorption sites exist, create set of alternative cluster positions (shifted by $-\vec{s}$): $\rightarrow v_{mat2}$
Calculate coefficients to describe cluster atom vectors as a linear combination of $\vec{k}$ and $\vec{l}$: $\rightarrow c_i, (c_{i2})$
Round coefficients c_i (and c_{i2}) to the next integer value: $\rightarrow c_i^R, (c_{i2}^R)$
Calculate vectors to nearest adsorption sites from c_i^R, (c_{i2}^R) and $\vec{k}, \vec{l}$: $\rightarrow v_{surf\_mat}$
Determine the distance between the cluster atoms and the nearest adsorption sites: $\rightarrow d_{mat}, d_{mat2}$
If second set of adsorption sites exist, copy entries of d_{mat2} into d_{mat} if they are lower
(Calculate normalisation factor and normalise dmat)
Calculate average value of all entries of dmat within r < 2a (minimise by variation of α and returning to step 3)
Calculate average value of dmat : $\rightarrow m_N$
Perform a linear regression (through the origin) of m_N and dset: $\rightarrow d_{ini}$

8. References

1. Ferrando, R. & Fortunelli, A. Diffusion of adatoms and small clusters on magnesium oxide surfaces. *J. Phys. Condens. Matter* **21**, 264001 (2009).

2. Yulikov, M., Sterrer, M., Risse, T. & Freund, H. J. Gold atoms and clusters on MgO(100) films; an EPR and IRAS study. *Surf. Sci.* **603**, 1622–1628 (2009).

3. Vilhelmsen, Lasse B. and Hammer, B. Systematic Study of Au6 to Au12 Gold Clusters on MgO(100) F Centers Using Density-Functional Theory. *Phys. Rev. Lett.* **108**, (2012).

4. Appy, D. *et al.* Transition metals on the (0001) surface of graphite: Fundamental aspects of adsorption, diffusion, and morphology. *Prog. Surf. Sci.* **89**, 219–238 (2014).

5. Wang, G. M., BelBruno, J. J., Kenny, S. D. & Smith, R. Gold adatoms and dimers on relaxed graphite surfaces. *Phys. Rev. B - Condens. Matter Mater. Phys.* **69**, 195412 (2004).

6. Jensen, P., Blase, X. & Ordejón, P. First principles study of gold adsorption and diffusion on graphite. *Surf. Sci.* **564**, 173–178 (2004).

7. Akola, J. & Häkkinen, H. Density functional study of gold atoms and clusters on a graphite (0001) surface with defects. *Phys. Rev. B* **74**, 1–9 (2006).

8. Varns, R. & Strange, P. Stability of gold atoms and dimers adsorbed on graphene. *J. Phys. Condens. Matter* **20**, 225005 (2008).

9. Chan, K. T., Neaton, J. B. & Cohen, M. L. First-principles study of metal adatom adsorption on graphene. *Phys. Rev. B - Condens. Matter Mater. Phys.* **77**, 235430 (2008).

10. Amft, M., Sanyal, B., Eriksson, O. & Skorodumova, N. V. Small gold clusters on graphene, their mobility and clustering: A DFT study. *J. Phys. Condens. Matter* **23**, 205301 (2011).

11. Amft, M., Lebègue, S., Eriksson, O. & Skorodumova, N. V. Adsorption of Cu, Ag, and Au atoms on graphene including van der Waals interactions. *J. Phys. Condens. Matter* **23**, 395001 (2011).

12. Jalkanen, J.-P., Halonen, M., Fernández-Torre, D., Laasonen, K. & Halonen, L. A Computational Study of the Adsorption of Small Ag and Au Nanoclusters on Graphite †. *J. Phys. Chem. A* **111**, 12317–12326 (2007).

13. Wang, G. M., Belbruno, J. J., Kenny, S. D. & Smith, R. Density functional study of Au-n (n=3-5) clusters on relaxed graphite surfaces. *Surf. Sci.* **576**, 107–115 (2005).

14. Xiao, L., Tollberg, B., Hu, X. & Wang, L. Structural study of gold clusters. *J. Chem. Phys.* **124**, 114309 (2006).

15. Castellani, N. J., Branda, M. M., Neyman, K. M. & Illas, F. Density Functional Theory Study of the Adsorption of Au Atom on Cerium Oxide: Effect of Low-Coordinated Surface Sites. *J. Phys. Chem. C* **113**, 4948–4954 (2009).

16. Liu, Z.-P., Jenkins, S. J. & King, D. A. Origin and Activity of Oxidized Gold in Water-Gas-Shift Catalysis. *Phys. Rev. Lett.* **94**, 196102 (2005).

17. Camellone, M. F. & Fabris, S. Reaction Mechanisms for the CO Oxidation on Au/CeO $_2$ Catalysts: Activity of Substitutional Au $^{3+}$ /Au $^+$ Cations and Deactivation of Supported Au $^+$ Adatoms. *J. Am. Chem. Soc.* **131**, 10473–10483 (2009).

18. Zhang, C., Michaelides, A. & Jenkins, S. J. Theory of gold on ceria. *Phys. Chem. Chem. Phys.* **13**, 22–33 (2011).

19. Zhang, C., Michaelides, A., King, D. A. & Jenkins, S. J. Positive charge states and possible polymorphism of gold nanoclusters on reduced ceria. *J. Am. Chem. Soc.* **132**, 2175–2182 (2010).

20. Hernández, N. C., Grau-Crespo, R., de Leeuw, N. H. & Sanz, J. F. Electronic charge transfer between ceria surfaces and gold adatoms: a GGA+U investigation. *Phys. Chem. Chem. Phys.* **11**, 5246 (2009).

21. Marta Branda, M., Hernandez, N. C., Sanz, J. F. & Illas, F. Density Functional Theory Study of the Interaction of Cu, Ag, and Au Atoms with the Regular CeO2 (111) Surface. *J. Phys. Chem. C* **114**, 1934–1941 (2010).

22. Teng, B.-T. *et al.* A DFT Study of the Structures of Aux Clusters on a CeO2(111) Surface. *ChemPhysChem* **13**, 1261–1271 (2012).

23. Zhu, W. J., Zhang, J., Gong, X. Q. & Lu, G. A density functional theory study of small Au nanoparticles at CeO2 surfaces. *Catal. Today* **165**, 19–24 (2011).

24. Luo, Y. *et al.* Theoretical insights into ω-alkynylfuran cycloisomerisation catalyzed by Au/CeO 2 (111): the role of the CeO 2 (111) support. *RSC Adv.* **7**, 13473–13486 (2017).

25. Piotrowski, M. J., Tereshchuk, P. & Da Silva, J. L. F. Theoretical investigation of small transition-metal clusters supported on the CeO2(111) surface. *J. Phys. Chem. C* **118**, 21438–21446 (2014).

26. Xiao, L. & Wang, L. From planar to three-dimensional structural transition in gold clusters and the spin-orbit coupling effect. *Chem. Phys. Lett.* **392**, 452–455 (2004).

27. Wang, J., Wang, G. & Zhao, J. Density-functional study of Au n (n = 2 – 2 0) clusters: Lowest-energy structures and electronic properties. *Phys. Rev. B* **66**, 035418 (2002).

28. Zhao, J., Yang, J. & Hou, J. Theoretical study of small two-dimensional gold clusters. *Phys. Rev. B* **67**, 085404 (2003).

29. Häkkinen, H. & Landman, U. Gold clusters (Au N , 2 <~ N <~ 1 0) and their anions. *Phys. Rev. B* **62**, R2287–R2290 (2000).

30. Murray, J. S. & Politzer, P. The electrostatic potential: An overview. *Wiley Interdiscip. Rev. Comput. Mol. Sci.* **1**, 153–163 (2011).

31. Stenlid, J. H. & Brinck, T. Extending the σ-Hole Concept to Metals: An Electrostatic Interpretation of the Effects of Nanostructure in Gold and Platinum Catalysis. *J. Am. Chem. Soc.* **139**, 11012–11015 (2017).

32. Murray, J. S., Lane, P. & Politzer, P. Expansion of the σ-hole concept. *J. Mol. Model.* **15**, 723–729 (2009).

33. Clark, T., Hennemann, M., Murray, J. S. & Politzer, P. Halogen bonding: the σ-hole. *J. Mol. Model.* **13**, 291–296 (2007).

34. Bulat, F. A., Toro-Labbé, A., Brinck, T., Murray, J. S. & Politzer, P. Quantitative analysis of molecular surfaces: areas, volumes, electrostatic potentials and average local ionization energies. *J. Mol. Model.* **16**, 1679–1691 (2010).

35. wxDragon. Available at: http://www.wxdragon.de/.

36. Santos-Carballal, D., Roldan, A. & de Leeuw, N. H. Early Oxidation Processes on the Greigite Fe 3 S 4 (001) Surface by Water: A Density Functional Theory Study. *J. Phys. Chem. C* **120**, 8616–8629 (2016).

37. Artini, C. *et al.* Structural Features of Sm- and Gd-Doped Ceria Studied by Synchrotron X-ray Diffraction and µ-Raman Spectroscopy. *Inorg. Chem.* **54**, 4126–4137 (2015).

38. Loschen, C., Carrasco, J., Neyman, K. M. & Illas, F. First-principles LDA+U and GGA+U study of cerium oxides: Dependence on the effective U parameter. *Phys. Rev. B - Condens. Matter Mater. Phys.* **75**, 035115 (2007).